On Water-Ingression during top-flooding of corium melts

Alejandro Villarreal Larrauri, Renaud Meignen, Michel Gradeck, Nicolas Rimbert

On Water-Ingression during top-flooding of corium melts

Alejandro Villarreal Larrauri[a,b,1], Renaud Meignen[a,*], Michel Gradeck[b], Nicolas Rimbert[b]

[a] *Institut de Radioprotection et de Sûreté Nucléaire (IRSN),Cadarache, 13115 St. Paul lez Durance, France*
[b] *Laboratoire Énergies & Mécanique Théorique et Appliquée (LEMTA), UMR CNRS 7563, Université de Lorraine, 54505 Vandœuvre-Lès-Nancy, France*

Keywords: **Severe accidents, MCCI, SSWICS, Water Ingression**

1. Introduction

A severe accident in a nuclear power plant may continue up to the moment where the mixture of molten fuel, cladding, and core structures, commonly called corium, is released out of the reactor pressure vessel into the containment, as it has been observed in 3 of the damaged units after the Fukushima Daï-Chi disaster [1]. At that point, the melt can start to attack the concrete of the basemat and pit walls. This mechanism is at first a thermal process where the hot liquid corium transfers its energy to the concrete and induces its degradation and melting, inducing further mixing of the molten concrete material into the corium mixture.

Although the thermal attack and melting of the concrete is an extensively investigated phenomenon [2], the evaluation of the problem is still limited due to the complexity of the thermodynamical and chemical interactions among the numerous components involved. More so, the context enveloping severe nuclear accidents, in particular with the specific materials, high temperatures, and presence of internal heat source (decay heat), complicates the evaluation even further. On that note, it is essential to highlight that the conditions under which the phenomenon is studied are commonly simplified. In the experiments dedicated to the study of the phenomenology of Molten Corium-Concrete Interaction (MCCI), the corium composition is approximated and introduces some biases due to technical difficulties to simulate the actual accident conditions. One may cite for these biases the scaling effects and the impossibility of representing the effect of decay heat adequately. For the latter point, the existing technologies cannot reproduce an homogeneous power, in particular regarding the solidification state of the corium (most of the heat introduced goes to the liquid, whilst

*Corresponding author
Email address: renaud.meignen@irsn.fr (Renaud Meignen)
[1] Currently a consultant at Tractebel Engineering SA - Belgium

June 4, 2021

Nomenclature

Latin

C Fitting coefficient	$[-]$	G_m Empirical factor	$[-]$
E Young modulus	$\left[\frac{kg}{m \cdot s^2}\right]$	j_i Superficial velocity of phase "i"	$\left[\frac{m}{s}\right]$
e Crack thickness	$[cm]$	p, P Pressure	$\left[\frac{kg}{m^2 \cdot s^2}\right]$
F_p Functional group defined by eq. (30)	$\left[\frac{J}{m^2}\right]$	S_i Saturation of phase "i"	$[-]$
g Gravitational acceleration	$\left[\frac{m}{s^2}\right]$	T Temperature	$[K]$
G_c Fracture energy density	$\left[\frac{J}{m^2}\right]$	y Crack spacing	$[cm]$

Symbols

α Void fraction (steam saturation)	$[-]$	ν Kinematic viscosity	$\left[\frac{m^2}{s}\right]$
β_s Superficial thermal expansion coefficient	$\left[\frac{1}{s}\right]$	ϕ Superficial heat flux	$\left[\frac{kW}{m^2}\right]$
κ Absolute permeability	$\left[m^2\right]$	ρ Density	$\left[\frac{kg}{m^3}\right]$
$\kappa_{r,i}$ Relative permeability to phase "i"	$[-]$	σ_c Tensile strength of the crust material	$\left[\frac{kg}{m \cdot s^2}\right]$
λ Thermal conductivity	$\left[\frac{W}{m \cdot K}\right]$	σ_{lv} Liquid-steam surface tension	$\left[\frac{N}{m}\right]$
μ Dynamic viscosity	$\left[\frac{kg}{m \cdot s}\right]$	ε Porosity	$[-]$

Subscripts

c Capillary	v Vapour (steam) phase
l Liquid phase	

only a meager fraction goes to the solid corium). Thus, due the uncertainties related to the understanding and modeling of this process, a melt-trough of the basemat, and thus releasing radioactive (and toxic) materials into the environment, cannot be excluded.

A possibility to terminate the melt progression, i.e., to stabilize the corium, is to flood it via a dedicated water supply device or by the water already present in other systems of the nuclear power plant. The objective of adding water on top is to rapidly cool down and solidify the melt so that the effects of the uncertainties on the corium-concrete interaction may be reduced to an acceptable level. As shown by various experimental programs (MACE [3], CCI [4], SSWICS [5, 6], COTELS [7]) the presence of water induces additional complex phenomena and biases which are also far from being fully understood and well controlled. At first, superficial heat transfer is, of course, increased with the presence of water, which induces a faster solidification and crust development. Nevertheless, its impact is not totally clear. A particular problem is the frequent observation of anchoring of the formed crust on the lateral test section walls [4]. Clearly, this anchoring is favored in the experiments by two facts, again: the reduced scale and the absence of internal heat in the solid crust. An

additional phenomenon has been observed depending on the nature of the concrete used in the test section of the MCCI dedicated experiments.

In the case of calcareous limestone concrete, the abundant gaseous CO_2 and steam production from the melt-concrete interaction should lead to an entrainment of the melt with the gas into the overlying water layer through the crust (existing fractures or vulcanoes). The entrained corium may lead to the formation of a prominent debris bed overlying the crust (e.g., CCI-8 [4]), although this has not been systematically observed. If the cooling of the entrained melt is not sufficient to ensure solidification during its mixing with water, it will settle on the crust, possibly forming vulcano-like structures. In any case, the entrainment of the melt through the crust substantially contributes to the cooling of the corium pool, although, up to our knowledge, no dedicated precise modeling nor simulations have been proposed to evaluate the actual thermal efficiency of the phenomenon. In the case of siliceous concrete, the ablation provides a reduced gas (primarily steam) flux into the melt pool, and the experiments show only rare melt ejection events. In such a case, cooling is much less efficient. However, a phenomenon of water ingression (WI) into the solidified upper crust is expected to improve the efficiency as compared to the cooling that conduction only through the crust would provide. Nevertheless, the phenomenon is complex, involving both the cracking of the crust by thermal stresses and subsequent water penetration through these cracks.

Water ingress into hot lava rocks has been qualitatively explained and modeled by Lister [8]. Epstein extended this work to the MCCI situation [9]. According to this Lister-Epstein model, the crack pattern and associated permeability are continuously driven by the thermal stress, itself driven by the heat transfer. In turn, the heat transfer is related to the permeability. Meanwhile, a series of dedicated experiments called Small-Scale Water Ingression and Crust Strength (SSWICS 1-7) has been performed [5, 6] using representative materials. These experiments will be discussed with some details in the next section, but a major conclusion is that a definite period of quite constant heat flux could be observed only for corium mixtures with concrete content smaller than about 10% (fig. 1). This plateau of heat flux is expected to be the result of the progression of water ingression into the corium. Furthermore, for the cases with evidence that the WI phenomenon was present, the associated heat flux plateau had a limited duration, with a quite long subsequent slow heat flux decrease, which is not explained. For the other cases, with more significant concrete content, no heat flux plateau was observed. This could be due to the fact that the heat flux in first period of flooding could not measured. Lompersky and Farmer used the Lister-Epstein model in their analysis of SSWICS 1-7 tests [5, 6]. However, from our understanding, as will be discussed in next sections, the model includes some technical issues, in particular linked to the the fracture process, previously noted and discussed in [10] and [11]. Also, the model implies numerous highly uncertain physical properties that render it difficult to use. Finally, it may be noticed that the authors focused on the heat flux in the water ingression period and did not explain the following heat flux slow decrease.

Several experiments were performed using simulant materials. Nayak et al. [10] performed experiments using a calcium-barium oxide mixture $CaO + Ba_2O_3$ (solidus/liquidus temperatures at 1180/1250 K), with an external heating at a level of $1.3MW/m^3$ simulating decay heat. In the same facility, Kulkarni [11] later used sodium borosilicate glasses as simulant (melting point at about 900 K from [11]). The similitude with the melt in MCCI conditions was not demonstrated and the authors mainly claimed the fragile glass-like behavior of corium-concrete mixtures. The results in [10] indicated an apparent sudden temperature drop over a depth of 10 cm assimilated to a sudden crack generation with a fast water penetration. They came to the conclusion that the creeping mechanism proposed in the Lister-Epstein model could not hold. Excluding the possibility of malfunction of their installation, the Nayak and Kulkarni finding is in fact not incompatible with the Lister mechanism, due to the characteristics of the employed material (low melting temperature, low thermal expansion). The cracks are initiated with a non-zero initial length, but they can further develop probably more continuously as the condition for propagation is different from that for initiation. Also, as will be shown later, the speed of crack propagation is likely not an issue. However, in [10], the drastic sudden melt temperature drop did not coincide with an increase of the steam mass flow rate. Thus, the interpretation appears quite unclear. Unfortunately, the paper does not give indication of the internal structure and permeability of the solidified ingot. A 1D transient model was also developed in [10] with the particular hypothesis that the fractures occur in a single step along a given length. Water ingression was supposed to generate a dry-out heat flux from a correlation for debris bed. Logically, the model computes a delay between the temperature drops at the different thermocouple heights. Thus the model does not explain the observation. Up to our knowledge, the model has not been applied to compare with SSWICS tests. In [11], the experiment yielded only very limited water ingression if any. Consistently, the previous model predicted a thermal stress lower than the critical one.

Very recently, Yeo and No proposed a new and original detailed analytical 1D modeling and applied it to describe the SSWICS tests [12]. The model makes the same hypothesis as Nayak and colleagues of a sudden crack formation once for all along a given depth, without further progression. Thus a key feature is that the fracture pattern is fully driven by the initial intense heat transfer in the stage of film boiling at the upper surface. This may explain the long decreasing heat flux period following the water ingression period. The model is then based on a separate evaluation of the permeability evolution and the heat transfer inside the crust, both with original argumentation. The permeability is evaluated using standard models for fractures in brittle material [13], discussed further in the present paper. Overall, the model seems legitimate, but there are important fitting constants (some adjusted for each test) with few explanations. Also, the demonstration of the model is presented without intermediate results, so that, in our opinion, it is difficult to judge on its applicability. All in all, the authors are finally able to retrieve the extracted heat flux for the SSWICS tests, including those where a WI phenomenon could not be actually observed (which may be a misinterpretation of the SSWICS presentation of results in [5, 6]). In contrast, the calculated permeabilities were only approximately consistent. The fractured crust depth

was only between 1 and 2 cm, which would then imply a poorly efficient mechanism. In addition, the period of decreasing heat flux after the plateau is not discussed, despite their hypothesis of finite crack length provides a clear potential explanation.

The objective of the present work is to address these recondite points to clarify the efficiency and the effectiveness of the WI on melt progression mitigation. Section 2 provides a preliminary analysis of the SSWICS experiment results. Section 3 is devoted to one-dimensional modeling of the thermal-hydraulics in fractured crusts, highlighting the limits of the WI phenomenon. This analysis is extended to study two-dimensional effects in section 4, concluding with the "real" expected accidental situations. Finally the question of the fracturing process is addressed in section 5.

2. Preliminary analysis of the SSWICS tests

As mentioned before, Lomperski, Farmer, and co-workers obtained the main available dedicated experimental results using prototypical corium in the frame of the OECD MCCI program [5, 6]. They investigated the cooling of mixtures of about 75 kg of corium and concrete slag by water injected from the top in a cylindrical test section with diameter equal to 30 cm (melt depth about 15 cm). The test section is essentially composed by an MgO liner and and MgO basemat, avoiding thus any ablation and any evolution of the melt composition during the test (except potentially through oxidation). The melt was produced inside the test section by a thermite reaction. Water was added on top of the melt shortly after the thermite reaction completion. On top of the test section, a 10 cm pipe carried out the generated steam flow to a condensation system. The heat flux was obtained through the measure of the condensation and is thus an indirect measurement of the steam flux above the water pool. In all except one test (#6) the water was initially largely subcooled ($\Delta\left(T_{sat} - T_{H_2O}\right) \sim 50 - 80°\mathrm{C}$). The measurements clearly indicated a first period with low steam flux, likely due to the heat up of the water. Consequently, the actual melt to water heat flux is absorbed by the water and not measured during this period which lasted from about 1000 s in the tests with the highest heat flux to about 1500 s for those with the lowest mean heat flux. Note also that the very first melt water contact produces a large amount of steam but measurements were not exploited due to the transient aspect and large uncertainties of the initial measurements. The corium was a mixture of UO_2/ZrO_2 formulated to have a core-to-cladding oxide mass ratio of 2.44 with added concrete of two types: LCS, i.e., limestone with a high content of calcite ($CaCO_3$), and SIL, i.e., siliceous, with a high content of silicon oxide. Four different concrete mass fractions in the corium mixtures were considered: 4, 8, 15, and 23 %, whilst two ambient pressures were used: 1 and 4 bars. To reduce the phenomenological complexity, the cavity receiving the corium was protected by a MgO layer, so that no ablation occurred. However, since MgO conductivity is rather high, the system was subject to important heat losses through the bottom and the sides. Also, no sustained power was injected in the corium to simulate decay heat so the

experimental results should not be directly extrapolated for safety evaluations. Therefore, the applicability of the models for an evaluation of accidental scenarios should be justified with care.

Figure 1 is reproduced from [5] and reports the measured heat flux for the first 7 SSWICS tests. The legend directly indicates the nature of the concrete, mass fraction, and ambient pressure. The interpretation of these curves is not so obvious and needs a preliminary discussion.

For all the tests, but # 6, there is an unclear first period, not shown on the figure, with a strong initial peak and then a sharp decrease towards a second period with nearly null flux , followed by a second increase. The 0-flux period is then attributed to the water heat up. As water is also heated during the first unclear period, no clear and valuable estimate of average heat flux can be made[2]. These effects of both these initial and 0-flux periods are out of the scope of the present work.

In three of the seven tests (# 1,3, and 7), a more or less clear heat flux plateau can be observed, which is interpreted as the result of a quasi-steady water ingression into the crust. These plateau emerge immediately after the 0-flux period so that it is clear that water ingression starts earlier than indicated in the figure. In contrast, the tests # 4, 5, and 6 show a heat transfer without any steady period and a general tendency very similar to simple conduction.

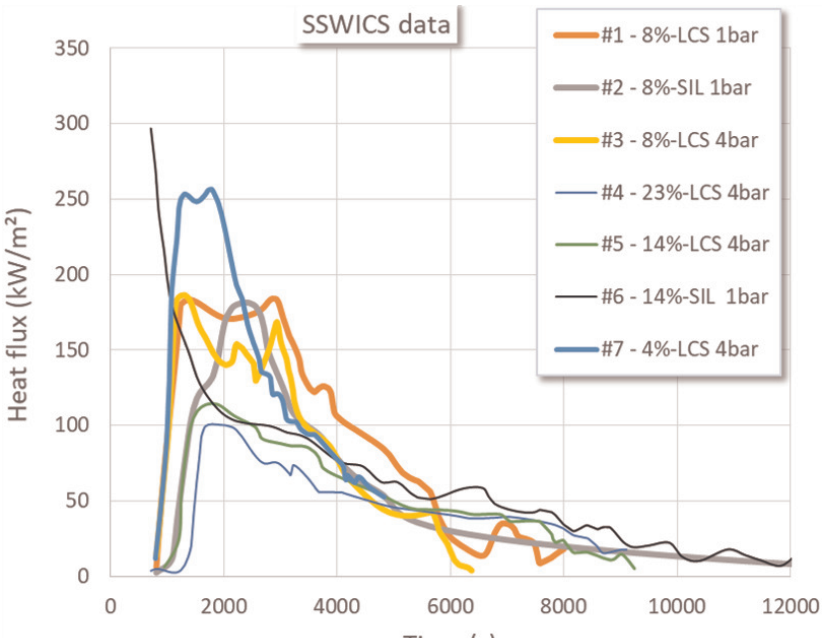

Figure 1: Measured heat fluxes in the 7 SSWICS tests. Reproduced from [5]. The first periods below 800 s. are not shown for clarity.

[2]Detailed estimates of the heat losses can be found in the (unpublished) test reports.

The original figure in [5] also shows the result of a simulation by the authors assuming purely conductive heat extraction, taking into account the heat losses in the experiments, leading to substantially lower heat fluxes. This result was supposed to show the effectiveness of WI in any situation. However, the authors used a conduction coefficient of 1.25 $\frac{W}{m \cdot K}$, which seems rather small as the corium conductivity is more often considered to be in the range from 2 to 3 $\frac{W}{m \cdot K}$ ([14, 15]). Clearly, with this range of conductivity coefficient, the conclusion that for these three tests WI was a governing phenomenon is more uncertain. In any case, the presence and level of a WI heat flux plateau cannot be stated. In fact, the conclusions from Lomperski and Farmer are not so manifest as they stated in [6] that "these three heat flux curves all resemble the conduction-limited solution, which would be expected if water ingression played a minor role in cooling. Still, the corium crack structure for these tests was found to be similar to that of the other, higher heat flux tests, suggesting that even for these low heat flux tests, water accounts for a significant portion of the difference between the measured heat flux and the conduction solution". However, the mechanism through which a limited water ingression would increase the extracted heat flux form conduction-limited was not clarified. From their interpretation, the tests with the highest amounts of concrete showed similar WI heat flux, around 100 $\frac{kW}{m^2}$. From our understanding, the results are not sufficiently clear to draw such conclusions. The presence of fractures may not serve as definitive evidence of the presence of WI since there are no evidence of effective water penetration in them.

In the case of test n°2, no real plateau was observed, but the high level of extracted heat flux (compared to tests n°4, 5, and 6) leads to consider that water ingression occurred to some extent, and the measured peak heat flux should provide a reasonable approximation.

Preliminary, and conservative, conclusions would then be that WI was observed for the mixtures with 4 and 8 % of concrete, whereas a conduction-limited heat transfer occurred for tests with 15 and 23 %. Regarding the heat flux level, it may be remarked that tests 1, 2, and 3, with 8 % of concrete led to comparable levels between 150 and 180 $\frac{kW}{m^2}$, whereas test 7, with 4 %, led to a noticeably higher flux of about 250 $\frac{kW}{m^2}$, so, again, an important impact of the concrete mass fraction. It may be argued that the WI heat flux plateau for the other tests was hidden in the first 0-heat flux period. However, it was no observed in test 6 done with water initially at saturation temperature. Second, it can be consistently remarked that higher levels of heat flux are contingent with smaller duration. Then a WI period in the first 1000 s. would imply a very high, and thus very short plateau, not consistent with the measures permeabilities, see discussion below. Last, it is important to highlight that the slow decrease following the quite short WI plateaus in tests 1, 2, 3, and 7 were not explained by Lompersky and Farmer. Following the Lister-Epstein model, the WI process should continue up to the complete cooling since the heat flux produces the permeability, which conducts, in turn, a given level of heat extraction. A clarification is then needed on this point for the consideration of the validity of the interpretations and models.

For six of the seven considered SSWICS tests, the permeability was determined by the measure, after the test, of water flow through the ingot, with the assumption of viscous Darcy flow. The two graphs of fig. 2 show these measurements as a function of the concrete nature (limestone and siliceous) and the ambient pressure (1 or 4 bars). The most explicit tendency is the diminution of the permeability with increasing concrete content. The primary reason is not so apparent and will be discussed afterward. Regarding the characterization of the impact of the two other parameters (concrete nature and pressure), the limited number of points does not permit unambiguous conclusions. It may be stressed, with substantial uncertainty, that the concrete's nature has a low impact, whereas the ambient pressure has a noticeable influence. The origin of the role of pressure is not clear and may be related to the two-phase flow characteristics and hence be explained by its impact on heat transfer, on which the crack spacing depends. This is indeed the hypothesis of the Lister-Epstein model. It may, however, be noticed that tests 3 and 6 have the same final permeability while both have different heat transfers, without water ingression period observed in test 6. In contrast, the Yeo-No model hypothesizes that the cracks are formed during the stage of film boiling of the uncracked crust. However, assuming a classical heat transfer model (e.g. [16]), the impact of pressure on the heat transfer is quite limited and does seem to be able to explain the observed significant difference in permeability.

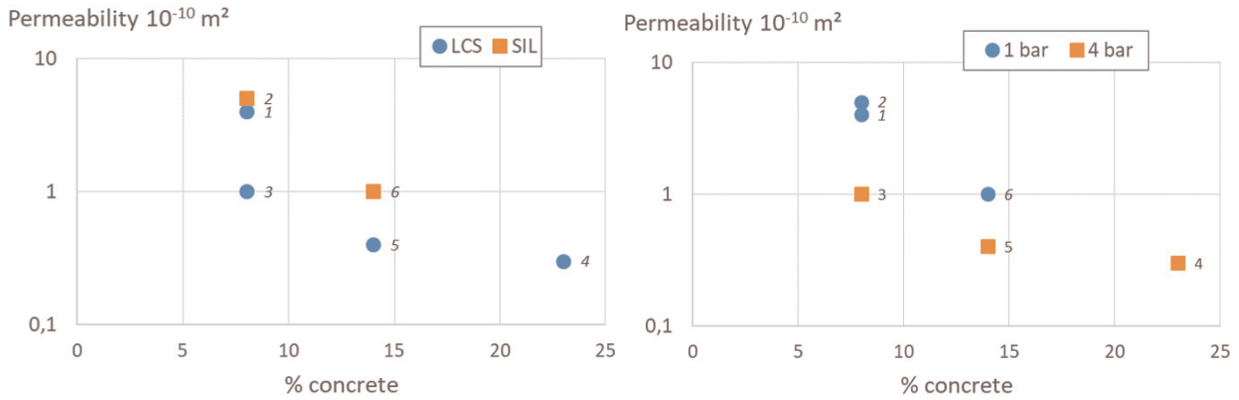

Figure 2: Measured permeability of the SSWICS ingots after tests. Left: impact of concrete nature; right: impact of ambient pressure. Test number is indicated close to each symbol. Data from [5].

The Lister-Epstein model used by Lompersky and Farmer shows a decreasing heat flux with an increasing amount of concrete, up to a plateau, or a gently decreasing region for concrete fractions larger than about 15 %. Looking at the model in detail, the decreasing heat flux and change in regime are principally due to the change of solidification temperature in the corium-concrete mixtures, the solidus reaching a plateau at about 2000 K for the same concrete fraction. Although one may doubt the almost constant predicted heat flux at large amounts of concrete, the drastic change of solidification temperature might explain the impact of the concrete on the heat flux.

To conclude, the situation is quite contrasted with experimental evidence of the existence of the phenomenon, but also with apparent difficulties to characterize it precisely.

- the phenomenon is well-identified only for limited amounts of concrete in the corium;
- the absence of direct observation for large contents is not explained;
- the slow heat flux decrease following the WI plateau has not received either any explanation;
- permeability measurements indicate an impact of the ambient pressure which is difficult to explain;
- the applicability to the real accidental situation was only partially analyzed in previous works; Epstein [17] discussed the role of decay heat and came to a quite negative conclusion on the impact of water ingression.

A clarification for the interpretation of the SSWICS experiments, the modeling, and the extrapolation to the real accidental scenarios is then needed. At first, it is proposed to provide an analysis of the WI phenomenon itself, with consideration of the measured permeability. A one-dimensional analysis will be proposed; after which two-dimensional effects will be discussed. This will lead us to a comprehensive interpretation of the measured heat flux and a fine characterization of the phenomenon. Finally, the generation of cracks and permeability will be discussed, with the goal of proposing a general methodology to construct a complete model based only on material properties.

3. One-dimensional thermal-hydraulic modeling of water ingression

3.1. Introduction

In this section, the focus will be to analyze the thermal-hydraulics related to water penetrating an already fractured crust, with prescribed characteristics. Such a medium may be considered as a porous one. Top reflooding of such dry-superheated porous medium has been investigated in some few experiments but, to our knowledge, has not received a complete comprehensive analysis in particular regarding the applicability of conventional porous medium models. The question has been investigated, and the complete analysis can be found in [18]. Let us summarize the main findings that will help to understand the orientation for the analysis presented here.

When the water penetrates the hot porous medium or crust, it will be partly transformed to steam in the hot part of the porous medium, and depending on the characteristics of both the remaining water layer and the initial conditions of the medium will proceed further into it. The major available experiments studying this configuration for a debris bed composed of round particles are those provided by Ginsberg and co-workers [19, 20], complemented

by those of Cho et al. [21]. In these experiments, with debris beds of steel balls from about 1 to 3 mm in diameter, some instabilities with penetrating water fingers and counter-current dry steam channels were observed. The origin of these instabilities has not been clarified. One may hypothesize at first some kind of Safmann-Taylor instabilities related to the laminar frictions [22], often encountered in porous media. However, as they were observed in situations where the inertial frictions play an important role, one may, instead, relate them to Rayleigh-Taylor instabilities [23], that are induced by phase acceleration or by gravity. One may observe that Yeo & No [12], followed the qualitative observations of Ginsberg, considered in a parametric way that the generated steam was escaping from some dried channels, whereas water would penetrate through the fingers as a one-phase flow.

An analytical modeling of these instabilities appears quite out of reach due to the complex thermal interactions. Instead, they have been investigated through two-dimensional numerical simulations with the MC3D code [24]. Simulations of debris beds in the inertial range (d=3 mm) showed a clear appearance of instabilities in the form of penetrating water fingers. It is essential to point out that a significant finding of these simulations is that the water fingers are, in nature, subjected to a two-phase counter-current flow. As they are progressing, these fingers tend to group by pairs, leaving completely dried regions, although some of them could have been previously flooded and cooled before drying up again. The simulations also indicated a tendency of the instabilities to be inhibited with a progressively diminishing permeability.

Although a firm demonstration is needed, the analysis done in [18] tends to show that for the singular case of water ingression in solidifying crusts with a homogeneous permeability, spatial instabilities of the cooling front are not likely, and a one-dimensional analysis can highlight the general behavior, provided the absence of border effects. Our study indicates that the wavelength of the instabilities scales with the permeability. So only small-scale instabilities may be expected here. As the fractured medium is treated here as a porous one, only instabilities larger than the fractures distance (see further, some few centimeters) are of interest for this study. Our simulations did not show such types of instabilities. This will be reinforced by dedicated numerical simulations performed and discussed further in a subsequent section of this work.

Nevertheless, it may be noted that CFD simulations performed in [18] indicate that the reflooding pattern may be very sensitive to the characteristics of the porous medium, in particular the homogeneity of the temperature field and of course that of the permeability field. These two-dimensional effects will be subject to a more detailed discussion later on.

3.2. Analytical model

The analytical model presented here is limited to the situation related to SSWICS experiments, namely that there is no additional gas flux coming from concrete decomposition,

and that oxidation can be neglected. The model may be extended to such without major difficulty.

In a dense porous medium where laminar effects are dominant (inertial and interfacial frictional effects are neglected), the flow is quasi-steady and the pressure drop is the same in both phases:

$$\frac{dp}{dz} = \rho_l g + \frac{\mu_l}{\kappa \kappa_{rl}} j_l = \frac{\mu_v}{\kappa \kappa_{rv}} j_v + \frac{dp_c}{dz} \tag{1}$$

The permeability is considered here as an intrinsic characteristic of the medium and is affected for two-phase flow by adjunction of specific functions, called relative permeabilities, κ_{rl} and κ_{rv} for the liquid and steam phases. In packed round particle beds, several formulations for these functions have been developed, but the most accurate seems to be those proposed by Reed [25], $\kappa_{ri} = S_i^3$ where S_i is the saturation of phase "i" (relative volume fraction). For the case of fractured porous media, several formulations have been proposed, amongst which is the one proposed by Fourar & Lenormand [26], with α being the void fraction (steam saturation, i.e. the steam volume relative to the pore volume):

$$\begin{cases} \kappa_{r,l} = \frac{(1-\alpha)^2}{2}(2-\alpha) \\ \kappa_{r,v} = \alpha^3 + \frac{3\mu_v}{2\mu_l}\alpha\,(1-\alpha)\,(1+\alpha) \end{cases} \tag{2}$$

The last term in eq. (1), p_c, is the capillary pressure, i.e., the pressure difference between gas and liquid phases due to surface tension effects. Capillarity in porous media is a complex phenomenon still incompletely understood and characterized. In order to clarify the mechanism of penetration, a preliminary analysis is proposed hereafter. Several correlations have been proposed, amongst which, a rather common one was formulated by Leverett [27]:

$$p_c = p_v - p_l = \sigma_{lv} \cos\theta \sqrt{\frac{\varepsilon}{\kappa}} J\,(S) \tag{3}$$

where $\theta\,[^\circ]$ is the wetting angle (in general taken as 0 to maximize the function). $J\,(S^*)\,[-]$ is an non-dimensional expression called the Leverett J-function dependent of $S^*[-]$, an effective liquid saturation, both of which may be evaluated using the several formulations that can be found in the literature, see e.g. [28], [29],[30]. There are rather large discrepancies among the various formulation but $J\,(S^*)$ is generally a smoothed increasing function from 0 to maximum values of the order of unity.

A plausible estimation of the capillary effects can be done by linearizing the term p_c over

the entire length of the debris bed Z [m] as $\frac{\delta J\left(S^*\right)}{\delta z} = \frac{\Delta J\left(S^*\right)}{\Delta Z}$. In the present context, water is penetrating a hot medium so the liquid is absent below the front, hence the void fraction is gradually decreasing from the front to the level z where the critical heat flux, corresponding to where the maximum possible steam flux is reached. Thus there are 3 distinct regions, shown schematically in fig. 3. In the cold region where, in the absence of decay heat, the flow is established and corresponds to the "critical" conditions, the void fraction is almost constant, so there is no variation of the void fraction, and thus no capillary effects. It may be noticed that water ingression may have started before the water above reaches the saturation temperature. Nevertheless, the amount of water in the fractures is very small and subcooling seems very unlikely (i.e. this cooled region is at saturation temperature from the moment water has penetrated and established the flow conditions through it). Similarly, in the region below the front, liquid is absent and so are any capillarity effects.

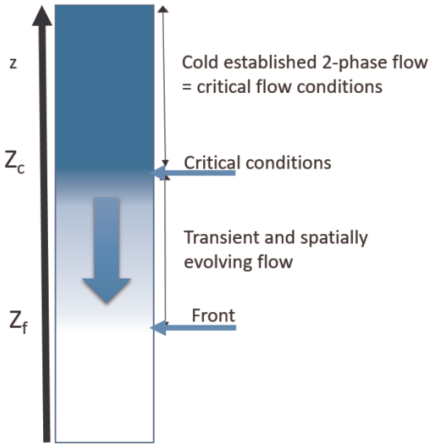

Figure 3: Sketch of the flow configuration for the analysis of the capillary effects

Let us note $J(S_z^*)$ the Leverett function at height z. Then, at any height z above Z_F, $\frac{\Delta J\left(S^*\right)}{\Delta Z} = \frac{J\left(S_{Z_c}^*\right) - J(S_{Z_F}^*)}{Z_C - Z_F}$ is negative since J is a decreasing function when there is a decreasing void fraction. This would suggest that the capillary pressure, in this case, would impede the front to advance since the liquid water would instead be "pulled inside" the finger and not in the direction of the advancing front. Indeed, saturation overshoots close to the "finger tips" have been observed in porous media experiments (see [31]). However, it is highly dubious that the existing formulations for the capillary pressure remain valid with the high temperatures conditions between Z_C and Z_F. Indeed, the current formulations all consider the wetting of the solid material phase, which seems rather unlikely here. Even if the capillarity may affect the penetration speed (although no current formulation seems adapted to the conditions expected here), it would not affect the flow above the front in the cooled region, where the critical heat flux is expected to occur (see next paragraphs). For these reasons, the effects of the capillary pressure are not included in the present modeling.

As the front progresses, there is a disequilibrium in the mass balance since a fraction of the water flux, here called X_l will be used to partially fill the empty pores at the front. For simplicity, the steam flux coming from below the front, e.g., from the concrete ablation, can be neglected. It will also be considered that the liquid water flow occurs in saturated conditions, i.e., no subcooling, which sounds reasonable for the problem at hand due to the high temperatures expected. Under these hypotheses, the mass balance at any height above the cooling front is:

$$\rho_v j_v + \rho_l \left(j_l + \varepsilon X_l u_l \right) = 0 \tag{4}$$

where u_l is the reflooding front velocity. However, in the present unsteady situation with water slowly progressing downward, it can be easily verified that the amount of water necessary for the progression ($\varepsilon X_l u_l$) is negligibly small. Substituting eq. (4) into eq. (1) (i.e., balancing mass fluxes, viscous shear and gravity) yields the following relationship between the steam flux and local void saturation, α, at any elevation z above the cooling front:

$$j_v = \frac{\frac{\rho_l}{\rho_v} \kappa g}{\frac{\nu_l}{\kappa_{r,l}} + \frac{\nu_v}{\kappa_{r,v}}} \tag{5}$$

Formally, the heat flux can be easily deduced by making the hypothesis that the heat is transported by the up-flowing steam with the enthalpy corresponding to the latent heat of vaporization:

$$\phi = \rho_v j_v h_{lv} = \frac{\rho_l \kappa g h_{lv}}{\frac{\nu_l}{\kappa_{r,l}} + \frac{\nu_v}{\kappa_{r,v}}} \tag{6}$$

Using the formulations of the relative permeabilities in eq. (2) or those presented by Reed [25], the gas flux can be linked to local void saturation. The result is shown in fig. 4, which plots the superficial steam and liquid velocities, given by eq. (5) and eq. (4) respectively, for a representative fractured corium crust with $\kappa = 10^{-10} m^2$, and evaluating the fluids properties at 1 atm and saturation temperature. As can be seen, for any given j_i, there are two possible solutions for α, i.e., two possible physical configurations. A maximum is then found, the location of which is depending on the relative permeability formulation. This maximum is located at a void saturation around 0.83 and 0.75 using eq. (2) and Reed formulation, respectively. The maximum represents then a critical flux beyond which the two-phase flow is not possible, or is unstable. In other words, the maximal amount $j_{v,c}$ of steam that can flow and transport energy out of the porous layer is located at this critical saturation α_c. It should be noticed that this maximum is located at high steam saturation,

and this may explain why, up to our knowledge, the right part of the curves has not been identified experimentally.

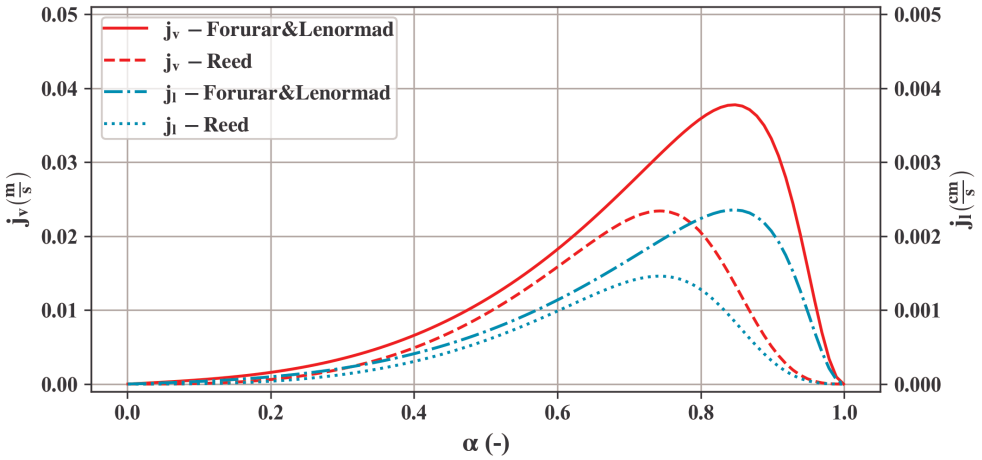

Figure 4: Laminar liquid and steam superficial velocities as a function of α at 1 atm for $\kappa = 1 \times 10^{-10} m^2$, j_v in left axis $\left(\frac{m}{s}\right)$, and j_l in right axis $\left(\frac{cm}{s}\right)$

Now, in a progressing water front in a hot media, the flow will "start" from the right side of fig. 4 with $\alpha = 1$ and should progress upward with increasing liquid volume fraction. As water injection is driven by gravity, the latter should tend to increase the liquid flux until an equilibrium is found, corresponding to the maximum possible counter-current steam flux. This point corresponds to the so-called critical heat flux, meaning the maximum heat flux transported by the steam. This maximum can be computed but no analytical expression can be given without some approximations.

First, the maximum is located close to α=1, which leads to the following approximation for the Fourar & Lenormand relative permeabilities formulation:

$$\begin{cases} \kappa_{r,l} = (1-\alpha)^2 \\ \kappa_{r,v} = \alpha^3 \end{cases} \tag{7}$$

By introducing eq. (7) into eq. (6) the critical heat flux can be written in the following form:

$$\phi_{WI} = \rho_v j_{v,c} h_{lv} = \frac{\rho_l \kappa g h_{lv}}{\frac{\nu_l}{(1-\alpha_c)^2} + \frac{\nu_v}{\alpha_c^3}} \tag{8}$$

In such conditions, $\kappa_{r,v}$ is of the order of unity whereas $\kappa_{r,l}$ is of the order $0.15^2/2$, i.e. 10^{-2}. Now, recalling that, under saturated conditions at 1 bar, the steam to liquid viscosity

ratio is roughly of the order of 60, it comes that the liquid contribution ($\nu_l/\kappa_{r,l}$) balances the steam and cannot be neglected. This finding seems to diverge from the heat flux formulation used in the Lister-Epstein model, where Epstein in [9, 17] expressed both Jones et al. [32] and Hardee & Nilson [33] model, for a pressure of 1 atm, as:

$$\phi_{modJones} = \kappa g h_{lv} \frac{(\rho_l - \rho_v)}{2\nu_v} \tag{9}$$

Nevertheless, looking at the actual Jones et al. correlation in [32]:

$$\phi_{do} = \kappa g h_{lv} \frac{0.015\,(\rho_l - \rho_v)}{\nu_v \left(1 + 0.003 \left(\frac{\nu_v}{\nu_l}\right)^2\right)^{\frac{1}{4}}} \tag{10}$$

it is clear that the viscous liquid contributions were not taken into account for the Lister-Epstein model. This might prove a somewhat sensible approximation at low pressures but quickly proves problematic at high pressures since the approximation diverges.

The critical flux can be analytically found by maximizing eq. (8), i.e solving:

$$\frac{{\alpha^{crit}}^4}{\left(1 - \alpha^{crit}\right)^3} = \frac{3}{2}\frac{\nu_v}{\nu_l} \tag{11}$$

which, for a pressure of 1 atm, is approximately at $\alpha^{crit} = 0.833$. An analytical expression cannot be obtained, but it is found that, for the conditions of interest, α_c is approximated by 0.8. Thus, the water ingression heat flux may be approximated by :

$$\phi_{WI} = \frac{\rho_l \kappa g h_{lv}}{25\nu_l + 2\nu_v} \tag{12}$$

Figure 5 shows a comparison of the critical heat flux relative to permeability ϕ_c/κ between the complete formulation (obtained by numerically solving eq. (11) to obtain the void fraction and evaluate eq. (6)), the previously expressed approximation, eq. (12), and the Epstein approximation of the Jones model, eq. (9) (labeled "modif Jones"), used in [5], over the range of pressures expected to be encountered in the containment in the context of an MCCI. Our approximate solution is fully satisfactory (compared to the full model). The modified Jones model gives similar results at 1 bar but is quickly diverging from the solution proposed here, overestimating the critical heat flux, as the pressure increases.

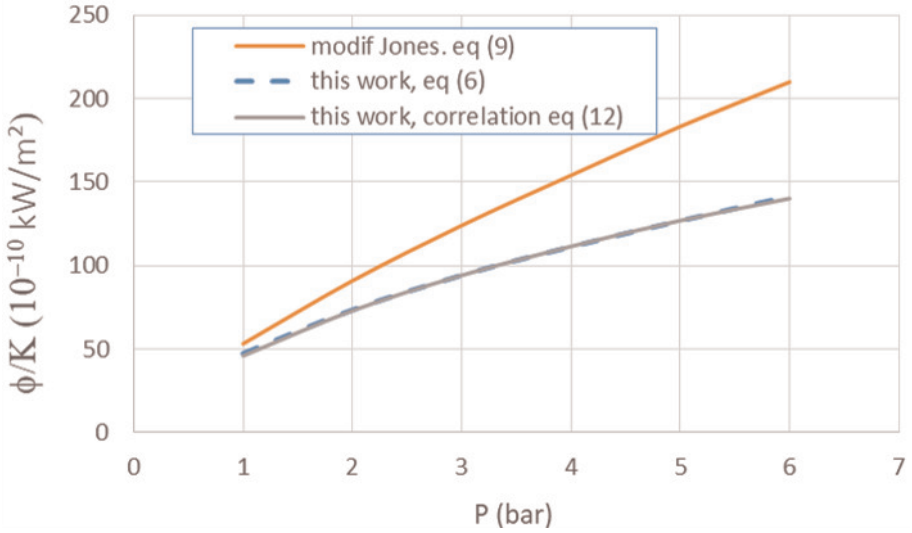

Figure 5: Comparison of the critical heat flux relative to the permeability with formulation eq. (6) (dashed blue), the approximate solution eq. (12)(gray) and the modified Jones one eq. (9) (orange)

An important point to note here for concluding this section is that the present model, as well as the other ones discussed, are limited in use to the situation without the presence of non-condensables either from concrete degradation either from strong oxidation. Such limitation is clearly to be considered for simulations of the full MCCI process.

3.3. Evaluations of the SSWICS experiments with MC3D

More elaborate evaluations can be performed using the MC3D-PREMIX model, slightly modified for the purpose. This 3D multiphase flow model, dedicated to evaluate the premixing stage of fuel coolant interaction (FCI) [34], is also used to evaluate the thermal-hydraulic behavior of debris beds [24, 35]. Basically, for such evaluation, the debris bed is simulated with one or several numerical fields of drops (spheres) with different diameters and material properties. A large collection of constitutive laws for frictions is available. Regarding the application to water ingression, as, in principle, the water traverses the crust through more or less parallel, and probably not communicating, cracks, the following modification of MC3D were done to compute the SSWICS tests:

- introduction of a dedicated correlation for the relative permeabilities: the Fourar & Lenormand model, eq. (2), was chosen;
- no account of the inertial friction term,
- strong increase of the lateral friction (for the two-dimensional calculations), and
- variable melt density in the solid state, as function of temperature, to simulate dilatation effects.

The permeability is computed using the Ergun [36] function for solid round spheres. Thus it is imposed by adjusting the drop diameter of the MC3D model. The starting porosity for the corium melt is set to 2%. Calculations with variable density shows final porosities of the order of 10 %. However, as variable porosity did not show a strong impact, several calculations were made with a constant porosity of 10 % and constant permeability, independent of the actual temperature.

As for the heat transfer, MC3D uses non-equilibrium modeling with heat transfers among the different fields through the various interfaces (drop-liquid, drop-gas, liquid-gas). In the situation of porous media, there is clearly a lack of knowledge, due to the fact that in general there is a fast quasi-equilibrium locally. Thus the local heat transfer are difficult to measure. Then, the heat transfers are mostly controlled by the transport of matter and energy by the two-phase flow inside the matrix (and so the importance of friction laws). In MC3D modeling of debris bed, the same laws as for dilute flows of corium drops are used ([24, 34]). In the present situation, where the crack distance is of the order of some centimeters (see section 5), local equilibrium is likely not reached. Clearly, there is room for improvement, but, at first, it was considered sufficient to keep this approximate approach.

Further simplifications for these preliminary studies are as follows. As there is no concrete ablation in the SSWICS experiments, there is no bubbling throughout the melt, so the liquid convection should be limited. Due to the physical properties of the mixture, the Rayleigh number becomes rapidly very large, when the melt is liquid. It is not possible to give here a precise number due to the important uncertainties but it can be stated that it may rapidly reach numbers in the order of 10^6. However, it is important to precise that the possible thermal convection effects were not investigated in this study due to the following reason. As it can be noticed, the initial temperature of the melt in the tests is always estimated to be close to liquidus of even below (e.g. test 7).

Computations with the NUCLEA database [37] of the mass fractions of most important phases of the SSWICS mixtures, show that the liquid fraction drops very rapidly below the liquidus temperature. This is because of the fast solidification of $UO_2 - ZrO_2$. Supposing that a transition towards solid mechanical behavior occurs at around, for instance, 50 % of solid fraction, this yields a "solidification" temperature about 100 K below the liquidus. So the mixture should reach very rapidly a "solid" or very viscous mechanical behavior. Our simulations show that the maximum melt temperature reaches rapidly, within maximum about 2000 s, this solidification temperature. Test 7, with the highest WI heat flux, and thus the fastest to start WI may then be the most affected. However, the initial temperature (2100 K) is already largely below the liquidus. It should in fact, following the results of the NUCLEA database, be almost solid. Hence, it can be concluded that thermal convection effects here should then be very limited, hence were not accounted for in the calculations. Furthermore, the effects of concrete decomposition gasses on the fracturing and permeability formation are not taken into account here. The bubbling may affect drastically the permeability.

It is also hypothesized that the fractures do not perturb the conduction significantly. This hypothesis is probably quite strong for lateral heat transfers close to the wall. It is finally highlighted that the horizontal upper surface heat flux is not directly computed precisely with the current modeling since it is not the focus of this work and its impact is limited. This is clearly contrasting with Yeo & No work where the hypothesis is made that fractures occur solely during the period of upper surface film boiling. The upper surface is very roughly modeled with more substantial permeability and porosity conditions, directly connected to a pressure boundary condition, letting water come inside the bed as necessary. As it will be shown, for the various SSWICS tests here considered, the heat transfer is rapidly limited by conduction, before reaching a water ingression period, if any.

Obviously, due to the various uncertainties, in particular the experimentally measured permeabilities, which are post-test mean values measured at room temperature, a precise validation is not sought for, but rather, the calculations are used as a qualitative interpretation of the experimental results, in conjunction with the analytical modeling presented previously. The typical meshing used for the one and two-dimensional calculations discussed later on, is shown in fig. 6. A slowly progressive mesh with increasing mesh sizes with the depth is imposed. Better precision is needed at the top to capture the beginning of penetration, hence the smaller mesh sizes. As for the 2D case, two different meshes have used: the radially regular one presented in fig. 6 and a radially progressive one, with finer meshes closer to the MgO wall, not shown here. The results are very similar. As can be seen, the water region above the melt pool is not represented. Instead, a pressure boundary condition is imposed, with an imposed volume fraction of water of 1 only water can enter the domain when the pressure is smaller than the imposed one in order to simulate water injection into the domain[3]. It is also noted that the three uppermost meshes (blue zone) have an imposed DROPS volume fraction of 0.8, to simulate large film boiling heat transfer at the surface. Clearly, the heat contained in the wall above the melt level is neglected [4].

As already discussed, except at the top, the melt is modeled with a fixed porosity of 10% i.e., a volume fraction of 0.9 (green zone). As the crucible material, mostly MgO, has a rather high conductivity, noticeable heat transfer to this material is expected. The effective loss of energy from the crucible to rest of the installation and atmosphere is also neglected. Furthermore, the temperature of the MgO layer is initialized at saturation temperature. Also, the intermediate zirconia thin layer between the bottom of melt and the MgO basemat layer is not taken into account as its conductivity is similar to corium's conductivity.

[3]only liquid water can enter the domain when the pressure is smaller than the imposed one

[4]due to the violence of the chemical reaction, a small part of the thermite has splashed up over the lateral wall

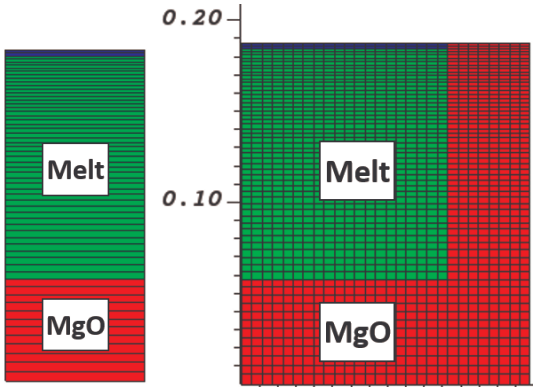

Figure 6: One and two-dimensional meshes for MC3D calculations of the SSWICS tests. The red part is not accessible to the coolant and represents the isolating material (MgO mostly)

Table 1 provides information related to the MC3D calculations initial conditions and both the experimental and simulation results of the water ingression heat flux plateau. The initial temperature (T_{cor}) and imposed permeability are taken from the experimental measures for SSWICS tests 1 through 6 (for test 7 no permeability measurement was made due to technical complications). The melt properties are roughly those reported by Farmer and Lompersky, see [6], slightly rounded as the precision given by the authors probably surpasses the actual uncertainties[5]. However, regarding the physical properties needed for theses thermo-dynamical calculations (density, latent heat, specific heat), these uncertainties are considered reasonable. Nevertheless, as already discussed, regarding the melt conductivity, the values taken as either 1.5 or 1.25 $\frac{W}{m \cdot K}$ in Farmer and Lompersky works are considered to be too low, hence a value of 2.5 $\frac{W}{m \cdot K}$ is used in these calculations. The impact of the uncertainty on this parameter will be discussed. It may also be noticed that the permeability used in the calculation of test SSWICS 1 and 2 differs intentionally from the experimental mean estimates, both around $5 \times 10^{10} m^2$, to evaluate the sensitivity to this parameter.

Table 1: SSWICS initial conditions for MC3D calculations and results

Test	**Concrete**	$\boldsymbol{\kappa}$	**m**	$\mathbf{T_{sol}}$	$\mathbf{T_{liq}}$	$\mathbf{c_p}$	$\mathbf{h_{ls}}$	$\boldsymbol{\rho}$	**Energy**	$\mathbf{T_{cor}}$	**P**	$\mathbf{\Phi_{calc}}$	$\mathbf{\Phi_{exp}}$
N°	**%**	$\boldsymbol{m^2}$ $\boldsymbol{(\times 10^{-10})}$	**kg**	**K**	**K**	$\frac{\mathbf{J}}{\mathbf{kgK}}$	$\frac{\mathbf{MJ}}{\mathbf{kg}}$	$\frac{\mathbf{kg}}{\mathbf{m^3}}$	**MJ**	**K**	**bar**	$\frac{\mathbf{kW}}{\mathbf{m^2}}$	$\frac{\mathbf{kW}}{\mathbf{m^2}}$
1	8	4	75	2000	2600	500	0,4	7300	82.5	2600	1	194	175
2	8	5	75	2000	2400	500	0,4	7300	75	2400	1	242	180
3	8	1	75	2000	2400	500	0,4	7300	75	2400	4	120	150
4	23	0.25	60	1400	2400	600	0,65	5600	72	2400	4	30	-
5	14	0.38	68	1400	2400	550	0,6	6500	74.8	2400	4	45	-
6	14	1	80	1400	2400	550	0,6	6200	83.6	2250	1	60	-

κ: permeability, m: mass, c_p: heat capacity, h_{ls}: fusion heat, T_{sol}: solidus temperature, T_{liq}: liquidus, ρ: density, T_{cor}: initial temperature, P: pressure, Φ_{calc}: calculated WI heat flux, Φ_{exp}: experimental WI estimated heat flux, Energy: Initial corium energy $(m \cdot c_p \cdot \Delta T)$

[5]the properties are not constant but vary notably with temperatures

Figure 7 shows the heat flux extracted at the top boundary for each of the one-dimensional calculations. For all cases, it can be observed that a plateau of heat flux was reached, denoting a water ingression extraction heat process. However, for the tests 4, 5, and 6, with low permeabilities, the plateau is low (barely perceivable in the current scale) and reached quite late in the simulation. In the calculations, the plateau is often preceded by a small heat flux peak; this is to be considered as a numerical effect accompanying the beginning of the water penetration. It can also be observed that the plateau duration is much longer than in the experiments (see fig. 1). In the calculations, the end of the plateau corresponds to the moment when the water reaches the bottom of the corium. An important finding from these calculations is the presence of quite slow decreasing heat flux after the plateau (not observed in the calculations 3 to 6 because they were stopped before the complete cooling). This decreasing heat flux is, in fact, due to the heat transferred to the MgO basemat, which is transferred back through the solidified cooled corium once it is cooled down. This decrease occurs however much later and sharper than in the experiments. This is, in fact, due for a large part to the limitations of a one-dimensional representation, avoiding radial heat transfers.

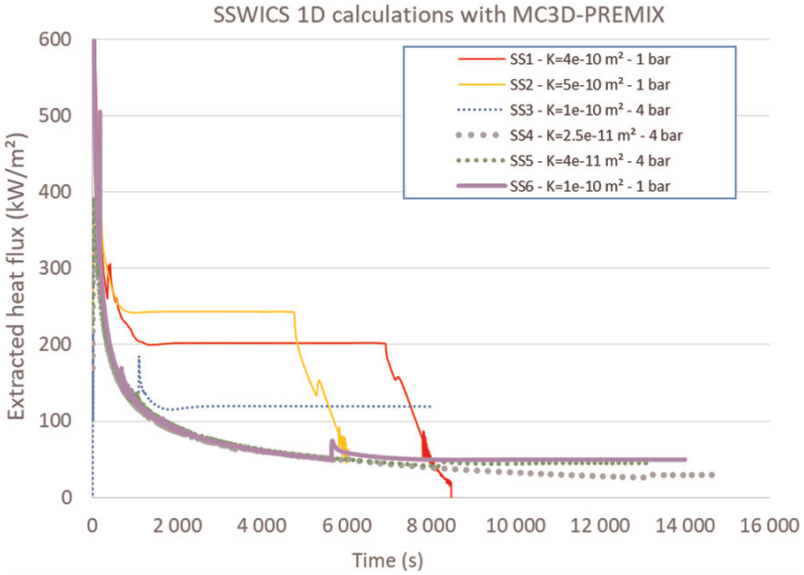

Figure 7: Extracted heat flux in the SSWICS one-dimensional calculations with MC3D

Figure 8 illustrates the SSWICS-1 calculation behavior for three different times. Due to the conduction, the temperature gradient is rather smooth. This is not obvious from the pictures, but the time 1500 s. marks approximately the moment when the heat is extracted solely through the transport of steam in the crust. The green lines marks the solidification front. The crust thickness is about 4 cm. Before that moment, water penetrated the hot crust slightly, and the heat is probably extracted by conduction and by water ingression. As can be seen in the images in the middle for each time, a substantial amount of heat is transferred to the MgO layer before the water reaches it. The lower images show the time

when the water reaches the bottom of the test section. From that moment on, the heat is transferred back from the MgO to the solidified corium, which leads to the slow heat flux decrease seen in fig. 7. It is important to point out that there should be in the experiment "real" losses of energy by heat transfer from the crucible to the rest of the installation.

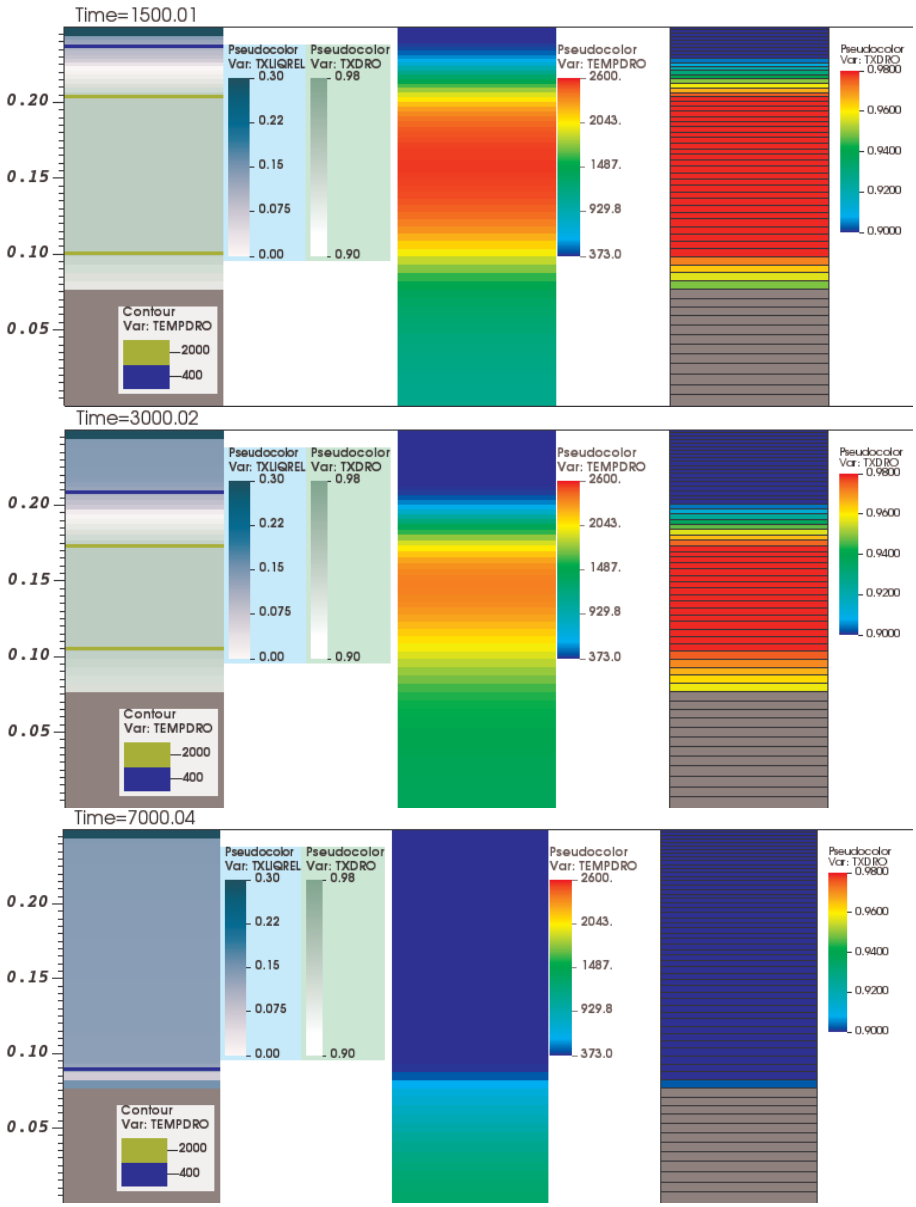

Figure 8: SSWICS-1 MC3D calculation at t=1500s., 3000 s. and 7000 s.

Left: liquid water volume fraction (blue shades) + corium volume fraction (green shades)+ levels for T=T_{sol}=2000 K (green lines) and T=T_{sat} (blue lines); middle: corium and MgO temperature; right: melt volume fraction

Figure 9 illustrates the SSWICS-6 calculation behavior. In this case, the water stars penetrating by about 6000 s. The dry crust is noticeably larger and continue to increase with the water penetration. It is about 8 cm thick at t=7000 s. It is noticed that, the solidification at the boundary with MgO disappears rapidly so that the corium remains liquid in the low part for a long time. At the end of the calculation, t=14000 s., the water has penetrated less than half of the melt (thus, the expected end of water ingress period should be by t=20000s, far beyond the test duration).

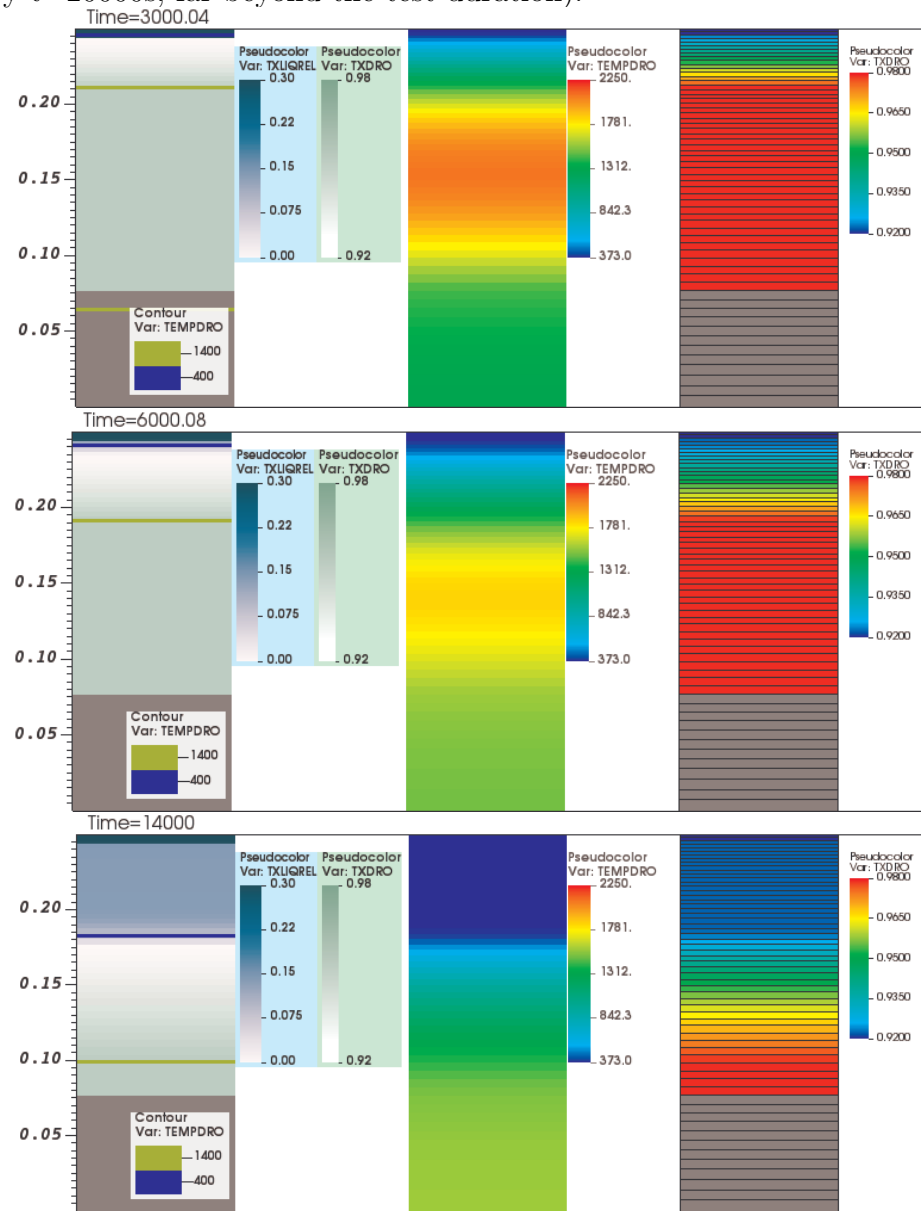

Figure 9: SSWICS-6 MC3D calculation at t=3000 s., 6000 s. and 14000 s.

Left: liquid water volume fraction (blue shades)+ corium volume fraction (green shades)+ levels for T=T_{sol}=1400 K (green lines) and T=T_{sat} (blue lines); middle: corium and MgO temperature; right: melt volume fraction

It can be noticed in Figure 7 that the calculated heat flux for test 6 has the correct tendency, but the experimental one is notably delayed in time compared to the calculation. Sensitivity tests regarding the conductivity have been performed and this uncertainty does not explain the delay. Also, modifications of the modeling of the top of the melt have been tested in order to try to obtain a peak heat flux comparable to the data. Again the effect is limited. However, the experimental heat flux history does not show any plateau that could be interpreted as a WI period, which would explain this delay (but would contradict all previous analysis as well as the present one). For these reasons, it is here concluded that this delay is due to some neglected aspect of our modeling, in particular the amount[6] of melt splashed on the upper part of the MgO liner during the chemical reaction, the heat contained in the MgO liner itself, or the fast penetration of the water along the wall (as indicated by the temperature sensors). A more precise modeling would be necessary to reproduce the experimental curves but this is not the aim of the present work.

The cases of SSWICS-4 and 5, not shown here, are even more problematic since water ingress occurs very late and has a very minor effect since most of the heat has already been extracted at that moment.

Figure 10 provides a comparison of the experimental heat fluxes (tests 1, 2, and 3 only), those computed with the analytical model (eq. (12)) and those obtained with MC3D, the latter two assuming then conditions as presented in table 1. With the small number of data points, it is not possible to conclude definitely, but one may nevertheless argue that the model results fits rather well the data and thus, that the measured permeabilities may be consistent with the measured heat flux. The calculations predict a relatively small impact of the pressure at 14% of concrete, but a noticeable effect occurs for 8%. The estimated WI heat flux falls to about $60\frac{kW}{m^2}$ at 14% of concrete and down to $40\frac{kW}{m^2}$ at 23%.

[6] not reported

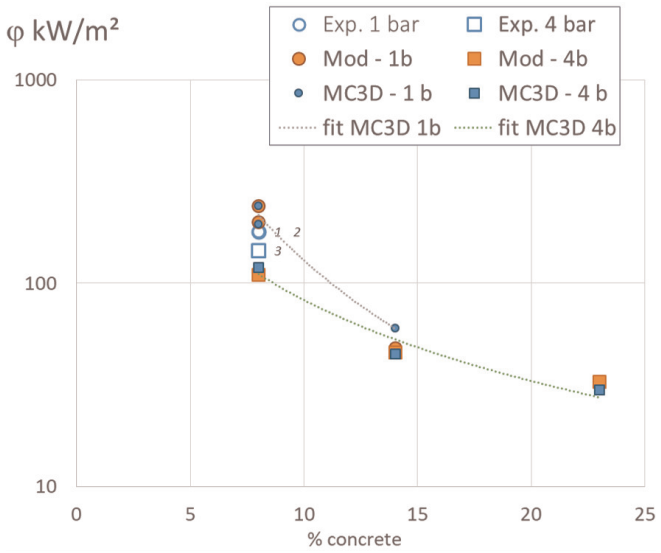

Figure 10: WI heat flux comparison of the SSWICS tests with the one-dimensional calculations. Large empty symbols : data (tests 1,2, and 3); large red full symbols : model with eq. (12); small blue full markers : calculations with MC3D; round markers : tests at 1 bar, squares : 4 bars

4. Two-dimensional effects

The previous one-dimensional simulations have shown a much too long heat flux plateau compared to the data. Border effects might explain this important discrepancy. It may be noticed that [7] pointed a critical border effect in the test they performed with water added on top of the melt. Apparently, from the analysis of the authors, the wall was rapidly degraded due to the important heat transfer. This potential effect, as well as wall melting, is out of the scope of the SSWICS experiments (designed to avoid such effect) and of the present analysis. The objective here is rather to analyse what could be interpreted as an artifact of the experiment, namely the role of the wall which acts as a temporary sink of heat. When the water has penetrated and cooled the corium, this sink will act as a source (with however some losses).

This was investigated using two-dimensional cylindrical calculations with the mesh shown in fig. 6. It is noticed that lateral MgO liner is somewhat thick, and due to the considerable conductivity of MgO, it may have significant effects. Figure 11 shows the result of the calculation of the SSWICS-1 tests, with the same conditions as for the one-dimensional calculation, for five different times. In it, for each time, the image on the left plots the liquid saturation field (and three temperature contours), whilst the image on the right plots the temperature field. As can be seen by comparing the temperature field for each time, a "fast" heat transfer occurs towards the MgO liner. The lateral gradient of temperature modifies the penetration pattern with a faster penetration close to the wall. However, in the meshes just adjacent to the wall, it is seen that the penetration does not really occur, leaving a thin dry zone (one or two meshes). This is due to the fact that the heat is released from the hot insulation liner (MgO sidewall) to the flooded part of the corium, following the water

advancement front. The water reaches the bottom a bit after 4000 s., to be compared with the 8000 s. in the one-dimensional case, illustrating the critical impact of two-dimensional effects. The corium is mostly flooded a bit before 5000 s. Nevertheless, the MgO is still rather hot, and heat is still transferring to the top water layer.

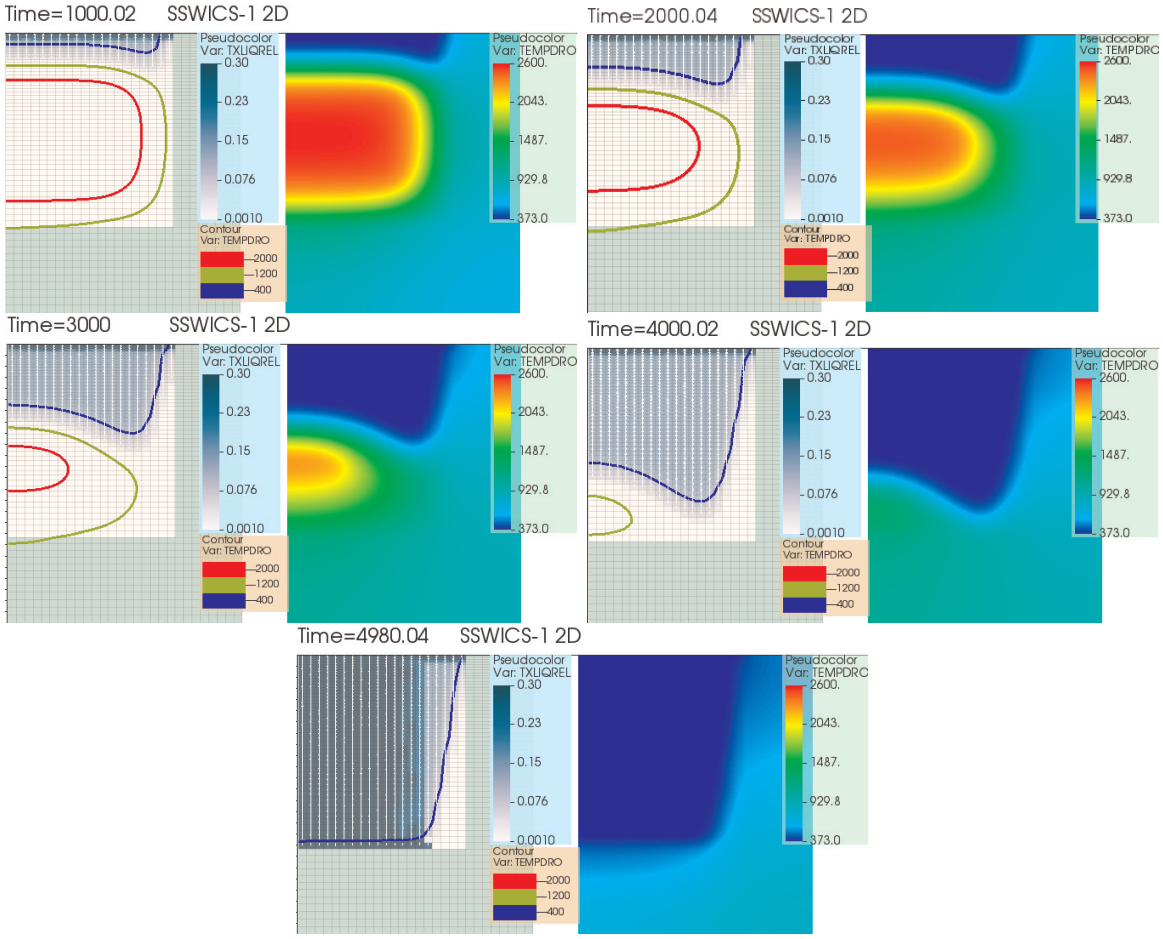

Figure 11: SSWICS-1 MC3D homogeneous two-dimensional calculation at 5 different times, left: liquid saturation and 3 contours of temperatures (TEMPDRO); right: melt and MgO temperature

If border effects are essential for heat transfer, they should also impact the permeability noticeably. In fact, the images of the corium ingot cross-sections in the publications of Lomperski and Farmer [6] visually indicate a higher permeability in the outer region closest to the wall, although no quantification of this has been done. To test the hypothesis of heterogeneous permeability numerically, the corium region was (arbitrarily) separated into two zones, with the second zone adjacent to the MgO sidewall initialized with different permeability. It is reminded that only a mean permeability is measured in the experiments and that Darcy's law leads to a flow rate proportional to the permeability. Thus, it is possible here to divide the test section in two vertical zones of surface area S_i and S_e (such that $S = S_i + S_e$) and two permeabilities κ_i and κ_e whilst maintaining the same global permeability:

$$\kappa = S_i \kappa_i + S_e \kappa_e \tag{13}$$

The simulation shown in figs. 12 and 13 was performed with $S_i = S_e = 0.5$. The permeabilities were set to $\kappa_e = 1 \times 10^{-9} m^2$ and $\kappa_i = 6 \times 10^{-11} m^2$, that is with an external region with a permeability approximately double compared to the mean experimental value, and a very small internal permeability, for which water ingression should be very difficult. The initial conditions of the calculation can be visualized in fig. 12 with the temperature field presented in the image on the right.

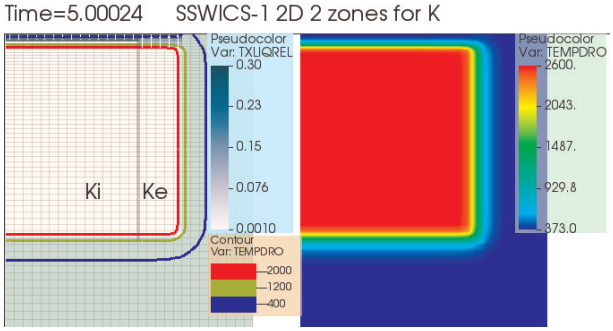

Figure 12: Two dimensional SSWICS-1 simulation: Initial conditions simulation with permeability heterogeneity.
Legend: see fig. 11; the vertical grey line in the left graph separates the two zones with permeabilities κ_i and κ_e

Figure 13 shows the progression of the simulation at four different times. In it, it can be clearly seen that the water penetrates mainly through the zone adjacent to the MgO sidewall, with the largest permeability. Nevertheless, as in the previous simulation, a non-negligible part of the energy is transported out of the corium via conduction. Similarly, the energy goes back once the corium is flooded in the vicinity of the wall. Compared to the previously presented homogeneous 2D simulation, it is noticed that the heat transfer back to the corium is faster since the top part of the MgO liner is cooled down more rapidly. This is accompanied by a faster wetting of the inner wall surface. In contrast, the core of the melt is almost impermeable (no water penetration in the central zone is observed), at least on the duration of the calculation. For the duration of the calculation, the heat in the central part is transferred almost entirely by conduction to the top and to the flooded channel.

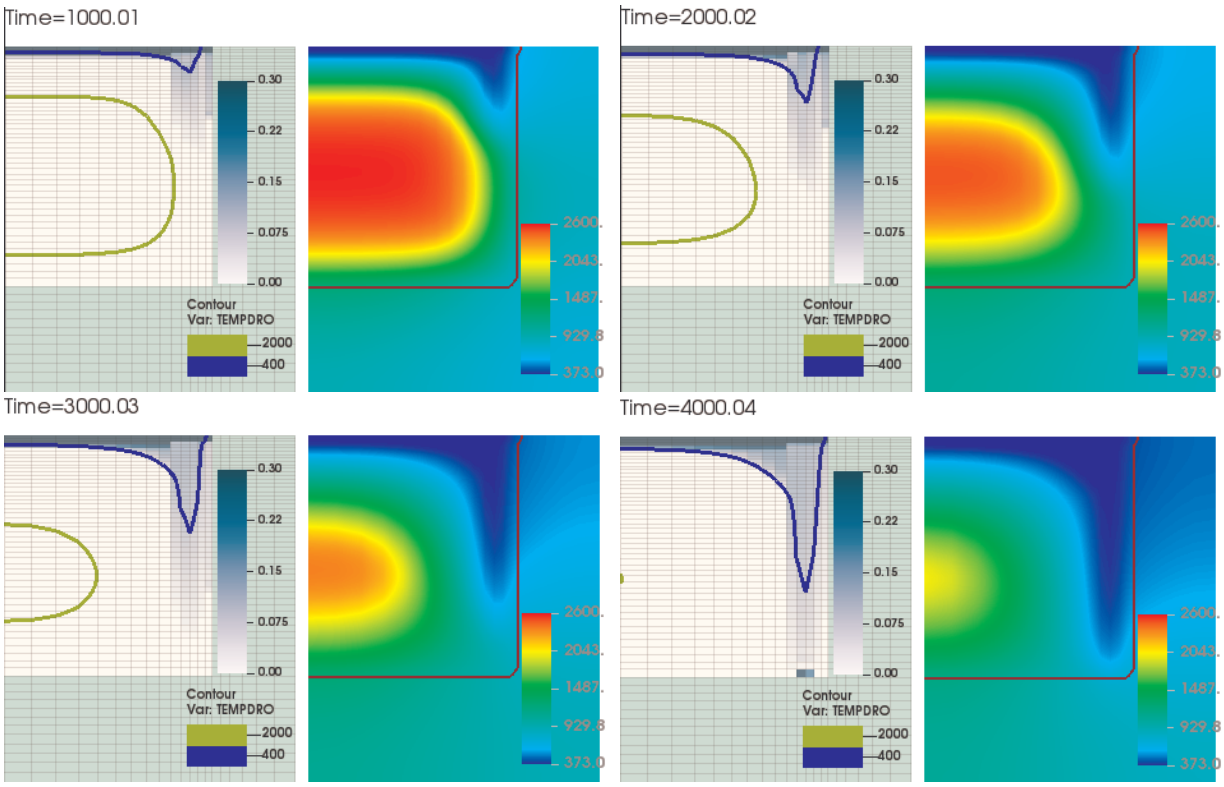

Figure 13: SSWICS-1 MC3D two-dimensional two-zone calculation at 4 different times
Legend: see fig. 11

Figure 14 plots the extracted heat flux for the one and two-dimensional simulations. The completely flat plateau in the previous one-dimensional and homogeneous two-dimensional simulations was not obtained in the two-dimensional two-zone simulation, but the tendency, before the heat flux drops, shows stabilization of the heat flux level. Both two-dimensional calculations show a reduced plateau with a duration similar to the experimental one and finally, both cases would be difficult to identify from an experimental result. One may also notice the the small spike observed at the end of the heat flux plateau in the experiments is not obtained in the calculations, so that no explanation can be given about that phenomenon.

Clearly, although these calculations are made with quite rough approximations and hypothesis, both two-dimensional calculated heat fluxes are reasonably close to the experimental one, and it is difficult then to draw firm conclusions about the impact regarding the permeability. Nevertheless, the importance of the border effect is highlighted.

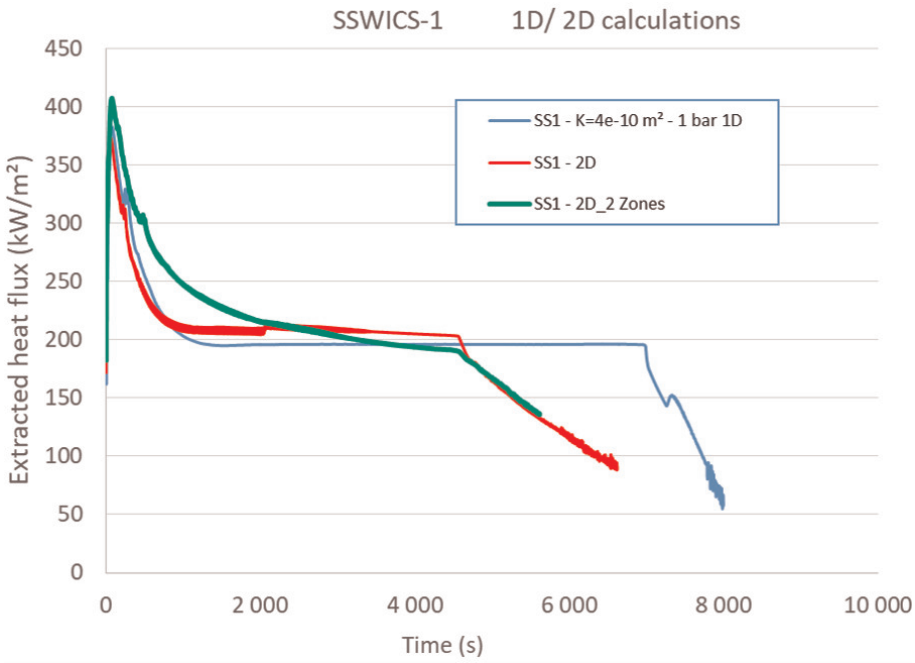

Figure 14: SSWICS-1 one and two-dimensional simulations: comparison of the extracted heat fluxes

5. Generation of cracks and permeability

In this section, the proposed model will be presented with particular attention in detailing the lines of reasoning for its formulation. To begin with, the classical theoretical models of crack generation are recalled. Then, their limitations are discussed.

The applicability of any such model with respect to the present situation adds several additional difficulties, in particular:

- the fact that the crust is building co-currently with the fractures, so at conditions of very high temperatures close the solidification;
- the large uncertainty attached to the mechanical parameters, particularly at the considered temperatures.

For these reasons, the choice was made to take advantage of the fact the the SSWICS experiments are done with a proto-typical corium, so that these uncertainties can be embedded in one empirical parameter. The different choice made with respect to other previous models (Lister-Epstein-Lompersky and Yeo) implies to use exactly the same values for all the parameters, as if they were universally admitted (the parameters used by Lompersky and Farmer are likely representative only at room temperatures). Changing any of these uncertain parameters will result in the need to re-fit the correlation.

5.1. General analysis of existing models

As seen before, the crucial point of water ingression modeling is the permeability, directly linked to the fracture generation in the crust. Generally speaking, in a brittle material, fractures will appear when the mechanical stresses will surpass a given value dependent on the material properties. It is at first essential to recall that both oxidic corium and concrete are materials with a brittle behavior at low temperatures. However, it is possible to anticipate that the fractures should start, or propagate, at high temperature, close to the solidification conditions, where visco-plastic behavior is expected. Furthermore, significant uncertainties exist regarding the properties of mixtures of corium oxides of type $UO_2 - ZrO_2$ and concrete oxides. In view of these difficulties, a rather parametric approach is likely necessary, based on comparison with existing data, namely the SSWICS tests. Considering this, the extrapolation to the real reactor situation appears difficult. In this case, several conditions that must not be neglected, namely the gas generation and associated dynamics of the mixture, along with the internal heat generation, should substantially modify the porosity and permeability generation from the mechanism involved in SSWICS. This point will not be discussed further in this work.

It is reminded that the permeability κ for a single thin planar crack of thickness e can be deduced from the laminar flow equations as: $\kappa = e^2/12$. In the porous-like medium, one considers the superficial flow rate. The medium's permeability must then account for the "superficial" porosity ε, and so $\kappa = \varepsilon e^2/12$. For a parallel crack pattern, $\varepsilon = e/y$, where y is the crack spacing. Instead, for a squared crack patter, $\varepsilon = 2e/y$ whilst for a polygonal pattern, the closest to observations, $\varepsilon = \sqrt{2}e/y$. Of course, the precise description of the crack pattern is out of reach and hence ε will be assumed of the general form:

$$\varepsilon = C\frac{e}{y} \tag{14}$$

where C is a constant depending on the fracture pattern (square, hexagonal, etc.), between 1 and 2. The porosity is also related to the shrinkage of the material after solidification and cooling, as a function of its thermal expansion coefficient, β_s $\left[\frac{1}{K}\right]$, and temperature drop, δT [K], from the solidification to the water saturation temperatures (temperature in the ingressed portion of the crust), as:

$$\varepsilon = \beta_s \delta T \tag{15}$$

β_s is here to be considered as a "surface" thermal expansion coefficient, which is twice the "linear" coefficient given in general in the literature. Nevertheless, it may be noticed that, if solidification proceeds from the top, the change in density during the solidification stage,

from liquid to solid, may also be partly considered, depending on the anchorage of the crust on the wall. None of the previous models discussed this aspect and took into account the change of density during the solidification state. In our opinion, some discussion is needed. An additional component related to the density change during the solidification itself, ε_{ls}, may then be included.

$$\varepsilon = \beta_s \delta T + \varepsilon_{ls} \tag{16}$$

Rather than fractures, the effect of density change during solidification itself may lead to porosities in the form of holes, as can be seen in numerous experiments involving fast solidification of corium, e.g., in Fuel Coolant Interaction, see for example [38, 39]. A plausible explanation is that the crust, due to the specific geometry and to the fast heat transfer, makes acts like a solid shell. This is not observed in SSWICS post-test cross-section examinations. It is possible then to conclude that the crust did not form a homogenous shell around the liquid part of the corium. Generally speaking, the permeability may then be written under the form:

$$\kappa = \frac{\varepsilon^3 y^2}{12C^2} = \frac{y^2(\beta_s \delta T)^3}{12C^2} \tag{17}$$

The second point of the modeling is then to determine the crack spacing. Before that, the previous formulation can be used to check the consistency between the measured permeabilities and the apparent crack spacing, which is visually in the order of few centimeters in SSWICS tests (see fig. 9 & 14 in [6]). This is roughly achieved with $\beta_s = 2.10^{-5} K^{-1}$, $\delta T = 2000K$ and $\varepsilon_{ls} = 0$. For simplicity, in the following formulations the component ε_{ls} is dropped, although this point needs further investigations.

Griffith [13] provided a first classical approach for the crack evaluation in a brittle material. He stated that the cracks would appear when the elastic energy accumulated in a constrained material is sufficient to create new surfaces, a process that needs a specific energy per unit surface (similar to surface tension for fluids). The elastic energy is due to the thermal stress induced by the change in density while the material temperature decreases. This energy is the product of the strain by the stress. Evidently, the boundary conditions, i.e., the constraint applied to the crust, are essential to precisely determine the stress and the strain.

At first, the case of constrained slab slowly cooled, with homogeneous decreasing temperature, is here recalled. Furthermore, in consideration of the large uncertainties regarding crust anchoring, a null Poisson coefficient will be considered. This is mainly a numerical simplification. Certainly, an additional parameter could be added, hence the expression

divided by $(1-\nu_p)$. Nevertheless, in view that the discussion revolves around orders of magnitude for the uncertainties of the modeling, such multiplicative parameter quite close to one is clearly not meaningful at this stage.

In this case the elastic stress due to thermal shrinking is simply $E\beta_s\delta T_c$, with E $\left[\frac{kg}{m\cdot s^2}\right]$ being the Young modulus and δT_c [K] the variation of temperature from which a solid-elastic behavior appears to the one where cracks will appear. The strain itself will be $\beta_s\delta T_c$, and thus the elastic energy may be written:

$$E_e = E(\beta_s\delta T_c)^2 \tag{18}$$

This embedded elastic energy must at least balance the surface energy of the new cracks, G_cS, where S is the surface of the created cracks per unit volume, and G_c $\left[\frac{J}{m^2}\right]$ the necessary energy per unit surface (also called the toughness of the material or the fracture energy density). S depends on the crack pattern but is roughly about twice the inverse of the crack spacing y, which is then determined as:

$$y = 2\frac{G_c}{E(\beta_s\delta T_c)^2} \tag{19}$$

A second condition in the Griffith theory allows to determine δT_c: the stress due to thermal shrinking must be larger than the tensile strength σ_c:

$$E\beta_s\delta T_c \geq \sigma_c \tag{20}$$

Thus, the approximate solution for the crack spacing is:

$$y = 2\frac{G_cE}{{\sigma_c}^2} \tag{21}$$

hence the permeability:

$$\kappa = \left(\frac{G_cE}{{\sigma_c}^2}\right)^2 \frac{(\beta_s\delta T_c)^3}{3C^2} \tag{22}$$

A first remark is the extreme sensitivity of the permeability with the parameters (highly non-linear): Young modulus and surface energy are raised to the 2nd power, thermal expan-

sion to the 3rd power, and the critical tensile strength to the 4th power. Unfortunately, the knowledge of these parameters is somewhat limited, particularly in complex compositions and high temperatures as those involved here for corium-concrete mixtures. In order to provide a first evaluation of the permeability the available data for the mechanical properties involved, including those proposed by Lomperski and Farmer [5, 6], is here presented:

- The temperature drop $\delta T = T_{sol} - T_{sat}$ for determining the permeability is rather well characterized, provided the consideration that the solidification behavior occurs around the solidus temperature. The solidus temperature falls strongly with the inclusion of concrete material into the corium, from, depending on the exact composition, about 3000 K with no concrete to about 1400 K with 10-15 % of concrete. This effect should impact strongly the permeability and explain, for a part, the decrease of permeability with increasing amount of concrete.

- The (surface) expansion coefficient β_s for solid components is generally around $5 \times 10^{-5} \frac{1}{K}$ at 2500 K for the UO_2/ZrO_2 mixtures, whereas the one for concrete components are smaller, of the order of $10^{-5} \frac{1}{K}$. The inclusion of concrete should then also decrease noticeably the shrinking effect and thus the permeability.

- The Young modulus is decreasing with temperature and drops to zero at the solidus temperature (visco-plastic behavior). At room temperature, the value is about $200GPa$ for UO_2/ZrO_2 [40]. For the different concrete's components, and different concrete mixtures, values around $30 - 60GPa$ can be found in the literature [41, 42, 43, 44]. Thus, probably decreasing the overall value for corium with the incorporation of concrete in the corium.

- The critical stress, in contrast, seems to increase with the incorporation of concrete in the corium, since values are around $100MPa$ for UO_2/ZrO_2 [40] to about $300MPa$ for the concrete mixtures.

- The major uncertainty may come from the surface energy, G_c. Values of about $1 \frac{J}{m^2}$ could be found for solid UO_2 alone [40], close to the value for liquid components. For liquid corium-concrete mixtures recent evaluations can be found in [45] of the order of $0.4 \frac{J}{m^2}$. In this work, a rough approximation of $1 \frac{J}{m^2}$ for solid corium-concrete mixtures is considered.

All in all, for UO_2/ZrO_2 mixtures, this leads to the value of $4 \times 10^{-13} m^2$ for the permeability. The inclusion of $10 - 15\%$ of concrete may not strongly affect the mechanical properties, but only the thermal expansion and this may lead to values around $2 \times 10^{-16} m^2$. This rough evaluation yield values smaller than the (averaged) measured values by several orders of magnitude. The addition of a component related to the shrinkage during the solidification stage itself (ε_{ls}) might help for the global permeability, but it would, in any case,

result in crack spacing much smaller than the visual observations in the SSWICS tests. This simplified model also leads to a very large crack temperature, since δT_c is only of the order of 125 K.

For non uniform cooling processes due to, e.g., a thermal shock, the usual procedure is similar for the determination of the initial crack spacing, except that the surface and elastic energy must be computed as integrals along the cracks. Formally, with l [m] being the crack length, the initial crack spacing may be approximated as:

$$y = \frac{\int_0^l G_c \, dz}{\int_0^l E(\beta \delta T)^2 \, dz} \tag{23}$$

where δT is the temperature drop throughout the thermal boundary layer. However, this refinement does not substantially help to gain the missing orders of magnitude of discrepancy with the experimental measurements.

In fact, the computation of the released elastic energy is not so simple since, around the crack tip, only a fraction of the energy is released. Overall, the previous energy balance proposed by Griffith is valid only if the behavior of the solid is purely elastic, which is rarely the case. In the present situation, this is probably far from being the case due to the high temperatures involved. For UO_2, an estimation of the transition of fragile to ductile behavior, i.e., with a noticeable plasticity, is around 1700 K [46], thus quite below the solidification temperature. The above evaluated high temperature for crack initiation is also an indication that the Griffith model cannot be used directly since the fracturing occurs partly with plastic behavior and consequential energy losses. In such a case, the energy balance must take into account the irreversible energy loss due to plastic deformation.

Modeling this behavior precisely is out of reach in the present context. In general, the visco-plastic deformation energy is accounted through the multiplication of the surface energy by a empirical factor, called hereafter γ_p:

$$E\alpha^2 \delta T_c^2 = \gamma_p G S \tag{24}$$

This is equivalent to multiplying the crack spacing by a fitting factor, as done by Yeo & No [12] (their factor ζ). The order of magnitude for this factor to accurately recover the experimental values is about 100. However, this approach may be rendered not satisfactory vis-à-vis of the substantial uncertainties, particularly the actual physical properties, so that the fitting process will be totally dependent on the choice of physical properties[7].

[7] this is already the case with the Lister-Epstein model used by Lomperski & Farmer, any change of the

Now, it is also interesting to recall some further characteristics of crack propagation. According to [47], for a sudden thermal shock (without water ingression), once a set of cracks has appeared, these cracks are constrained to propagate with the same spacing until an instability takes place leading to a selection of propagating cracks and arrest of the others. This selection leads to a reduction in the number of cracks, which in turn grow in thickness. This might be due to the fact that in a pure conduction problem, the thickness of the temperature gradient tends to increase. Indeed, [48] proposed a simple scaling law between the spacing y, the crack length l, and the cooling penetration depth δ_T :

$$\frac{y}{l} = C\left(\frac{y}{\delta_T}\right)^2 \tag{25}$$

with the constant C being of the order of 0.5. Roughly, by scaling the crack length with the thermal gradient length, δ_T, results in the crack spacing scaling simply with the length. As the permeability is a growing function of the crack spacing, this should lead to a positive gradient of permeability with depth. However, in a configuration with cracks of different lengths, the porosity will likely be prevalent in the longest cracks, so that the permeability may be rather homogeneous along the height. Thus an "effective" crack spacing may be obtained by considering only the longest cracks. This leads to the consideration that the crack spacing y is proportional to $\delta_T \simeq \frac{\lambda \delta T_c}{\phi}$ and thus, inversely proportional to the square of the heat flux ϕ. Using eq. (17), the permeability can be put under the form:

$$\kappa = F\frac{(\lambda \delta T_c)^2(\beta_s \delta T)^3}{\phi^2} \tag{26}$$

where F is a function of the material properties that may be considered as a constant. Both δT and δT_c may have very similar values if the crack temperature is close to the solidus temperature, and may be approximated by $\delta T_{sol} = T_{solidus} - T_{sat}$.

Lister-Epstein model makes a somewhat similar hypothesis, applying it all along the transient in such way that $\phi = \phi_{WI}$ is the WI heat flux, to obtain:

$$\kappa_{LE} = F\left(\frac{(\beta_s \delta T)^3}{\phi_{WI}^2}\right)^{4/5} \tag{27}$$

Both formulations (eq. (26)) and eq. (27)), when applied to the WI heat flux, lead to a sharp decrease of the permeability with the increase of the heat flux. In view of the results in

uncertain properties lead to change also the adjustment of the model

fig. 2 and the related discussion, this seems in contradiction with experimental observations (the permeability and heat flux follow the same tendency). In contrast, eq. (26) may be consistent if one considers the surface heat transfer as the one generating the preliminary crack pattern. If the "effective" crack spacing scales with the thermal layer, the porosity at the surface will grow with time. One may also take into consideration the apparent prevalence of the term $(\beta_s \delta T)^3$ regarding the impact of the concrete amount on the heat flux. Furthermore, in conjunction with the decreasing conductive heat flux, both effects will contribute to delaying the time in water ingress until the conditions are reached. Once this condition is reached, the water ingress will maintain the heat flux, and so will the thermal layer (if the corium depth is sufficient).

5.2. Semi-empirical model, without decay heat

With the previous hypotheses, a semi-empirical model can be formulated. The permeability is firstly written as:

$$\kappa = G_m \frac{\lambda^2 \delta T_c^2 \beta_s^3 (\delta T_{sol})^3}{\phi^2} \tag{28}$$

with:

- $\delta T_{sol} = T_{solidus} - T_{sat}$,
- δT_c the temperature drop of longest cracks; it may be assimilated to δT_{sol},
- and G_m used as an empirical factor, embedding the uncertain mechanical effects (and physical properties), to be adjusted from the available experimental data, namely the SSWICS ones; from eq. (17), it might be of the order of $1/(12C^2) \sim 1/50$

Furthermore, from eq. (12), the flux may be expressed as:

$$\phi_{WI} = \kappa F_p \tag{29}$$

with $F_p = F_p(P)$ being an identified grouping, depending mostly on the pressure:

$$F_p = \frac{\rho_l g h_{lv}}{25\nu_l + 2\nu_v} \tag{30}$$

Substituting eq. (28) into eq. (29), and identifying δT_c with δT_{sol}, results in the correlation:

$$\phi_{WI} = (G_m F_p)^{1/3} \lambda^{2/3} \beta_s (\delta T_{sol})^{5/3} \tag{31}$$

Conversely, the permeability is given by:

$$\kappa = \left(\frac{G_m}{F_p^2}\right)^{1/3} \lambda^{2/3} \beta_s (\delta T_{sol})^{5/3} \tag{32}$$

Now, G_m may be evaluated by comparing the measured permeabilities and heat fluxes. However, the formulation eq. (32) indicates an impact of the ambient pressure of the form: $F_p^{-2/3}$. Figure 5 indicates an increase of F_p of the order of 2 to 3 from 1 to 4 bars although permeability measurements tend to show factor of about 4. For this reason, it may be anticipated that G_m may also vary with the pressure. Figure 15 shows the results of the model with

$$G_m = \frac{1}{50} \frac{P_0}{P} \tag{33}$$

where P_0 is the reference pressure = 1 bar. β_s, the thermal conductivity and the solidus temperatures are evaluated as indicated in the Appendix A. Several points have been added in conditions not tested in SSWICS, in particular the cases without added concrete. It is noticed that despite its important impact on the permeability, the ambient pressure impacts only marginally the heat flux. Overall, a strong decrease of the permeability and the heat flux is obtained up to about 14 % of concrete, essentially due to the decrease of the solidification temperature. At that point, the heat fluxes are about $50 \frac{kW}{m^2}$. With the addition of concrete, there is then a slow decrease of permeability and heat flux due to the small expansion coefficient of concrete.

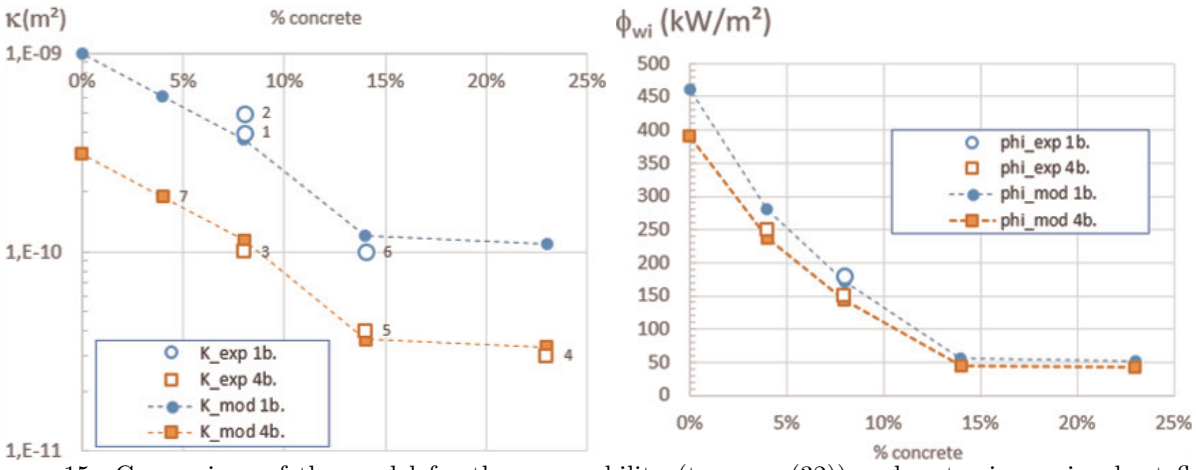

Figure 15: Comparison of the model for the permeability (top, eq. (32)) and water ingression heat flux (bottom, eq. (31)) and the available SSWICS data

5.2.1. Impact of decay heat

As did Epstein in [17], the situation with decay heat may be extrapolated for completeness, but no data is available to support any model (the data provided in [10] are not sufficient and, as already discussed in the introduction, there is a need for clarification of the behavior). Experiments involving internal power are also with concrete ablation and thus with an important bubbling and evolution with time of the concrete amount and corium mixture properties. Then, the precise evaluation of a complete situation is out of the scope of the present work, hence the aim is to provide a general analysis of the particular effect of internal decay heat.

Here the focus is to examine the situation with an homogeneous internal power density P_r $\left[\frac{W}{m^3}\right]$ independent on the solidification of the melt, in a quasi-steady situation. The situation of the experiments with internal heat only affecting the liquid part of the melt may be easily extrapolated from the following and will not be discussed here. The heat flux to be extracted is $P_r L$, where L is the total height of the melt (subject to internal power). More precisely, $P_r L$ represents the part of the internal energy that is extracted upward, through the crust. Again, the evaluation of the downward heat flux is out of the scope here. A schematic of the considered melt configuration is shown in fig. 16.

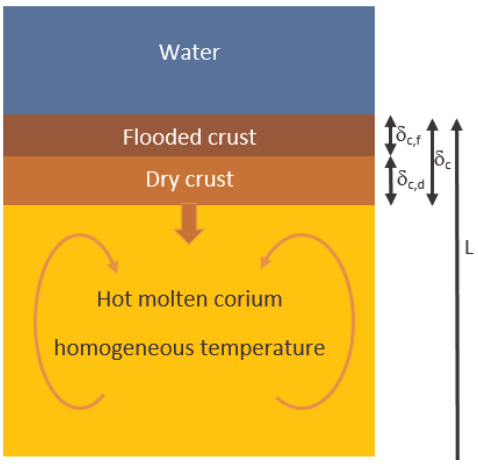

Figure 16: Schematic of the model configuration for the melt.

When the decay heat is important, the corium is liquid for a large part with a superficial crust where most of the thermal gradient is embedded. The bubbling due to concrete ablation, which is likely at the moment of reflooding, should homogenize the temperature in the liquid part. The crust may be decomposed into a flooded part, of thickness $\delta_{c,f}$, and a dry part, of thickness $\delta_{c,d}$, such that $\delta_c = \delta_{c,f} + \delta_{c,d}$. The critical heat flux occurs at the top of the crust, and may be expressed as the sum of the heat flux at the liquid front, say Φ_f, and the generated power in the flooded crust (on top of the front):

$$\Phi_c = \Phi_{WI} = \Phi_f + P_r \delta_{c,f} \tag{34}$$

The front heat flux comes from the internal power and conduction through the dry crust, so that it may be approximated as:

$$\Phi_f = \lambda \frac{\delta T_c}{\delta_{c,d}} + P_r \frac{\delta_{c,d}}{2} + P_r (L - \delta_c) \tag{35}$$

where the second term is the contribution of internal heat to the temperature profile, the third term is the part of the power generated below the crust, and extracted through the crust. Combining the last expressions finally leads to:

$$\Phi_{WI} = \lambda \frac{\delta T_c}{\delta_{c,d}} + P_r \left(L - \frac{\delta_{c,d}}{2} \right) \tag{36}$$

$$\delta_{c,d} = \lambda \frac{\delta T_c}{\Phi_{WI} - P_r \left(L - \frac{\delta_{c,d}}{2} \right)} \tag{37}$$

Equation (37) may be formally solved and eq. (28) replaced by:

$$\kappa = G_m \frac{\lambda^2 \delta T_c^2 \beta_s^3 (\delta T_{sol})^3}{\delta_{c,d}^2} \tag{38}$$

The extracted heat flux remains, at maximum, the critical heat flux of the fractured medium, eq. (29): $\Phi_{WI} = \kappa F_P$. However, the solution cannot be expressed analytically. For this reason it is possible to simplify and make the hypothesis that the crack length (at the initiation of the water ingression) and spacing are of the same order than the dry crust thickness $\delta_{c,d}$. Thus, back to eq. (17), it is possible to roughly express the permeability at the initiation of penetration as:

$$\kappa \simeq G'_m \delta_{c,d}^2 (\beta_s \delta T)^3 \tag{39}$$

with, keeping the role of pressure as before,

$$G'_m \simeq \frac{1}{12C^2} \frac{P_0}{P} \tag{40}$$

Once the water penetrates, the front is progressing downward with a velocity depending on the margin between the actual extracted flux and the input decay heat.

The set of equations eqs. (29), (37) and (39) are easily solved numerically. The parameter G'_m is adjusted in order to approach to the previous solution in the absence of internal heat. In this case, at one bar, it can be adjusted to 1/30, quite comparable to the 1/50 in the previous more complete model.

The solutions can be derived for any amount of concrete. In the frame of a strategy for mitigating severe accidents, the reflooding should occur early, with a melt containing only a few amount of concrete. For this reason, only the case of a corium mixture containing 8% of concrete at the reflooding time will be commented here. Figure 17 shows the results of the evaluation as a function of the upward input power per unit surface. It is reminded that, roughly, the decay heat lies between 2 and 1 $\frac{MW}{m^3}$ from one hour to one day after the SCRAM. If the melt is well spread in the reactor pit, the height L should be about 30 cm. The model predicts an important increase of the water ingression heat flux with increasing power $P_r L$, due to an increase of permeability with the crust thickness. Furthermore, the extracted heat flux may be sufficient to ensure in any case a margin between the input and extracted power, thus with a propagation of the form roughly estimated in fig. 17. Regardless, in the case of relatively large "input power", for example, $P_r L = 600 \frac{kW}{m^2}$, the front velocity of 4 $\frac{cm}{h}$ may necessitate about 8 hours to fully solidified 30 cm of melt, a time during which ablation should persist and lead to a strong increase of the concrete amount in the corium mixture, thus reducing strongly the permeability.

For completeness of the analysis, a short a discussion highlighting the difficulties and necessary new hypotheses ensues. As the melt concrete content will rapidly increase with time, the crust will show a profile of increasing fraction of concrete with the depth. Note at first that the decay heat will no longer be homogeneous as the crust will gradually have a larger amount of the initial corium as compared to the progressively concrete-rich corium, hence a larger volumetric fraction of the source of decay heat. Thus more heat should be generated in the crust compared to the liquid part and there should be a gradient of heat power, with highest value on top of the bed. The increase of concrete amount will reduce the local and global melt dilatation and then effective final porosity. When large amounts of concrete are present, the thermal dilatation will strongly decrease and the porosity will fall drastically. As the crack spacing is a function of the dry crust thickness, it seems difficult that, in case of reduction, new cracks appears, hence the crack spacing should either be stable, or increase, which counter-balances the negative previous effects.

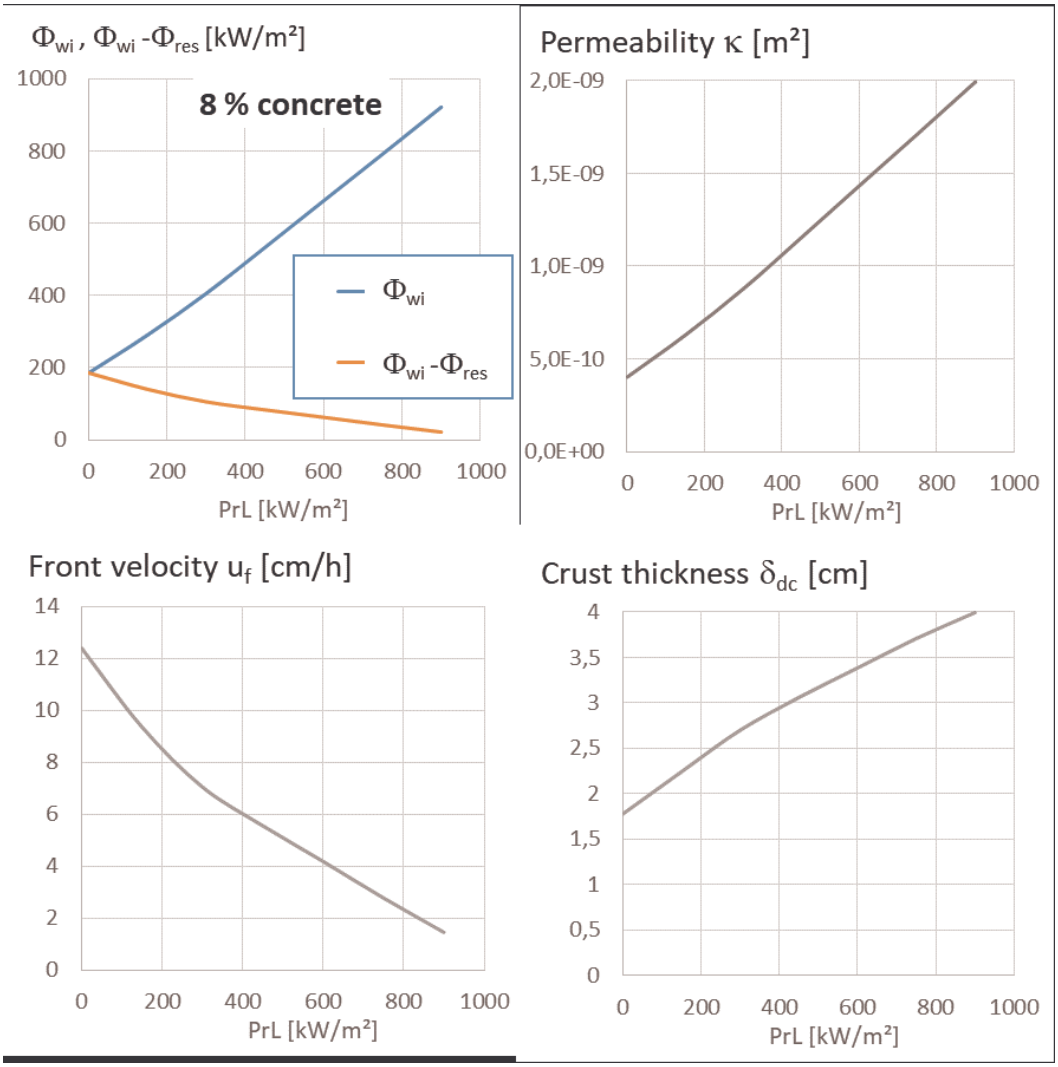

Figure 17: Results regarding the impact of decay heat for a quasi-steady situation (constant amount of concrete) on the heat flux (top left), the permeability, front velocity and dry crust thickness.

6. Conclusions

In this work, the difficulties of evaluating and extrapolating the mechanisms that govern the phenomenon of water-ingression into a solidified corium crust with internal decay heat, have been highlighted. Underlining the lack of experimental data to corroborate the models here presented, it is important to exploit the available data with prototypical corium, limited to cases without heat input. Section 2 presents the preliminary analysis on the the SSWICS tests concluding from the data:

- the existence of a strong reduction of permeability with increasing amount of concrete, and
- a clear effect of the pressure on the permeability resulting however in a low overall impact on the heat flux.

In sections 3 and 4 a thermal-hydraulic model was derived, accompanied by one- and two-dimensional CFD calculations. The calculations performed were found in agreement with the constructed heat transfer correlation and most importantly show that:

- for corium with a concrete content larger than 14 %, a low heat transfer of the order of 50 $\frac{kW}{m^2}$ is consistent with the permeability data; in these cases, the water ingression occurs very lately and, in fact, most of the heat flux history can be explained by conduction through the crust;
- important border effects were present in the SSWICS tests; at first the significant heat transfer to the lateral MgO wall; secondly, although less clear (suspected through visual observations of post test configuration), larger fractures close to the test section wall, due to the both presence of the wall and the heat transfer towards it, that may impact the water penetration through the crust.

In order to properly evaluate the generation of permeability and therefore the heat extraction to be expected from a fracturing crust subjected to water ingression, section 5 presents the construction and utilisation of a model to evaluate the WI under the specific conditions of the SSWICS tests and extrapolate to conditions closer to what's expected in a severe accident. Summarizing, section 5 tackled:

- the development of a semi-empirical model, limiting the use of very uncertain physical properties, hypothesizing that, on the range of conditions studied in SSWICS, the mechanical properties embedded in the fitting coefficient are not changing drastically,

- the satisfactory application of the developed model in comparison with the SSWICS data,
- the development of specific methodology aimed to extrapolate the WI fracture model to a case with the inclusion of decay heat,
- the evaluation of WI phenomenon with decay heat, resulting in effective heat extraction in all cases, even with high power, but low cooling front speed.

The modeling of the complete situation, including ablation, is far out of the present scope. The most difficult point may be related to the gas generation which may be integrated without difficulty in the thermal-hydraulic models, but may also have an impact on the permeability. However, it must be emphasized that Water Ingression is an issue for the accident evaluations and mitigation only for the cases where the concrete is very siliceous, i.e. with low gas production during the ablation. For the other cases, the existing experiments show that the concrete ablation leads to a very turbulent flow and an important mixing of melt and water, which is much more effective than WI for cooling the corium.

The modeling presented in the current work leads to consider that, in the presence of strong decay heat, water ingression may start rapidly, providing that reflooding occurs relatively early enough to assure low concrete content in the corium melt. However, the cooling front velocity of some few centimeters per hour allows envisaging a full solidification though this effect only in cases of spreading of the melt on a quite large surface, i.e. small melt height. A complete model necessitates several additional hypotheses, better knowledge of physical properties, and should take into account different characteristic configurations (e.g. the effect of corium-steel mixtures), which, in any case, highlights the clear need for additional dedicated experiments.

Acknowledgements

Throughout the many stages leading to the development of the models and the obtaining of the results here presented, we have received a helping hand from various colleagues. In particular we would like to acknowledge Stéphane Picchi and Guillaume Astier, IRSN, for their key support and availability.

Appendix A. Material properties

The present model was built in a way to limit the impact of highly uncertain thermophysical properties. As an input of the model, eqs. (31) and (32) need the solidus temperature (as the solidification temperature), the superficial thermal expansion coefficient and the thermal conductivity coefficient. It is important to point out that all mixtures properties cannot be estimated with simple geometric or arithmetic averages, so, in lack of experimental values, the properties are provided as first approximations.

Material properties of either UO_2, ZrO_2 or $(UZr)O_2$ can be found in [40]. $(UZr)O_2$ properties are nevertheless subject to large uncertainties. UO_2 properties can also be found in [14]. SiO_2 and $CaCO_3$ properties may be found in a large amount of different sources.

Clearly, any change in the used properties should need an adjustment of the G_m parameter in eq. (32). The material properties adopted here are the following.

Appendix A.1. Mechanical material properties

- Surface thermal expansion: thermal expansion coefficient reported in the literature are linear ones, so the surface coefficient is twice the linear one. The thermal strain of $(UZr)O_2$ mixtures seems to show large discontinuities with temperatures due to the behavior of ZrO_2, while UO_2 displays a more regular increasing thermal strain. The overall coefficient of ZrO_2 will be considered as null, the UO_2 one will be taken from [14]. As for silica, the literature reports small values of about $2.5 \times 10^{-6} \left[\frac{1}{K}\right]$ at ambient temperature, a value that will be used here. In this study, the thermal expansion coefficient of the corium was evaluated as a mass weighted average of the given composition: UO_2, ZrO_2, SiO_2 and $CaCO_3$, the two later being representative of the concrete.

$$\beta_{s,ZrO_2} = 0 \left[\frac{1}{K}\right] \tag{A.1}$$

$$\beta_{s,UO_2} = 2 \times \left(1.18 \times 10^{-5} - 5 \times 10^{-9} T + 3.7 \times 10^{-12} T^2 - 6.1 \times 10^{-17} T^3\right) \left[\frac{1}{K}\right] \tag{A.2}$$

$$\beta_{s,SiO_2} = 2 \times 2.5 \times 10^{-6} \left[\frac{1}{K}\right] \tag{A.3}$$

- The thermal conductivity coefficient of corium is also subject to uncertainties. For UO_2 [14] reports values ranging from 8 $\frac{W}{m \cdot K}$ at ambient temperature down to about 2 $\frac{W}{m \cdot K}$ at 2000 K, and then re-increase to about 3 $\frac{W}{m \cdot K}$ at 3000 K. Recently, [15] reported similar values for $(UZr)O_2$ mixtures for 2 temperatures (550 and 1400 K). As a mean,

it seems that a value of 2.5 can be used. For the silica, [49] reports values from 1.4 $\frac{W}{m \cdot K}$ at ambient temperature to about 3 $\frac{W}{m \cdot K}$ at 1500 K. Overall a representative value of 2.5 $\frac{W}{m \cdot K}$ was selected for all SSWICS tests mixtures.

Appendix A.2. Thermodynamic material properties

Finally, the solidus temperature for the corium-concrete mixtures can be obtained from databases as these are rather well identified. However, these properties are particularly complex, as several phases are involved.

In the calculations presented here, we use simplified thermodynamic properties. In particular, the solidus and the so-called solidification temperatures are supposed to be identical and are approximated. Figure A.1 shows the values used in the calculations as a function of the amount of concrete.

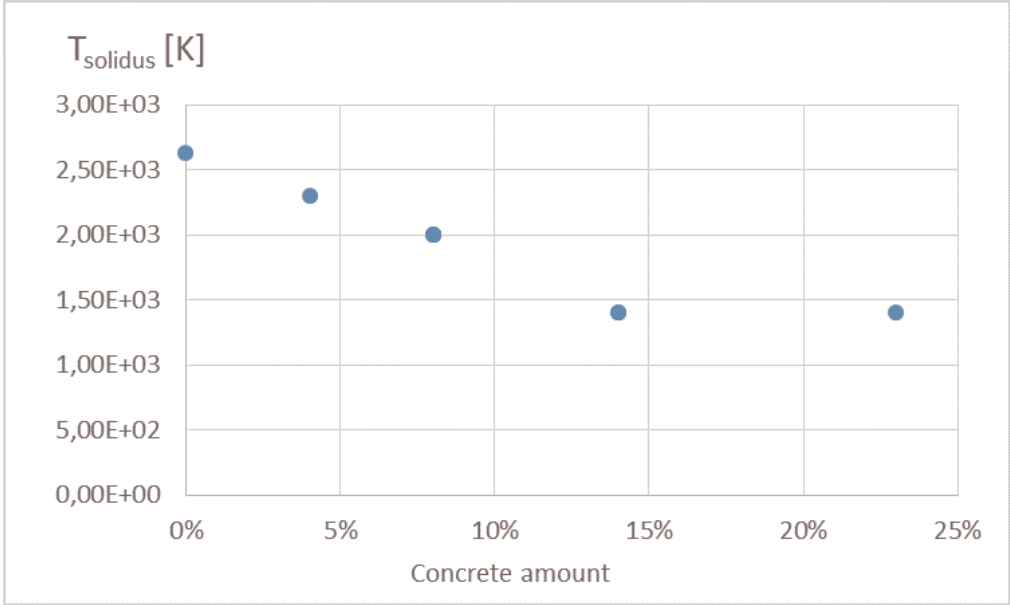

Figure A.1: Solidus temperature of corium mixtures used in the calculations

References

[1] NDF, Technical Strategic Plan 2019 For Decommissioning of the Fukushima Daiichi Nuclear Power Station of Tokyo Electric Power Company Holdings, Inc. : Overview, Report, Nuclear Damage Compensation and Decommissioning Facilitation Corporation (NDF), 2019. URL: http://www.dd.ndf.go.jp/en/strategic-plan/book/20191101_SP2019e0V.pdf.

[2] OECD, State of the Art Report on Molten Corium Concrete Interaction and Ex-Vessel Molten Core Coolability, State of the Art 7392, OECD, 2017. URL: https://www.oecd-nea.org/nsd/pubs/2017/7392-soar-molten-corium.pdf.

[3] S. Levy, Summary of coolability studies undertaken by ACE, MACE, ACEX, Technical Report, S. Levy Incorporated (SLI), California, 2002.

[4] M. T. Farmer, B. Tourniaire, K. Atkhen, Molten Core Concrete Interaction with Early Top Flooding: Results of the CCI-8 Experiment, in: Proceedings of 17th International Topical Meeting on Nuclear Reactor Thermal Hydraulics (NURETH-17), Xi'an, China, 2017, p. 12.

[5] S. Lomperski, M. Farmer, S. Basu, Experimental investigation of corium quenching at elevated pressure, Nuclear Engineering and Design 236 (2006) 2271–2280. URL: https://linkinghub.elsevier.com/retrieve/pii/S0029549306003062. doi:10.1016/j.nucengdes.2006.03.041.

[6] S. Lomperski, M. Farmer, Experimental evaluation of the water ingression mechanism for corium cooling, Nuclear Engineering and Design 237 (2007) 905–917. URL: http://linkinghub.elsevier.com/retrieve/pii/S0029549307000222. doi:10.1016/j.nucengdes.2006.12.009.

[7] Y. Maruyama, Y. Kojima, M. Tahara, H. Nagasaka, M. Kato, A. A. Kolodeshnikov, V. S. Zhdanov, Y. S. Vassiliev, A study on concrete degradation during molten core/concrete interactions, Nuclear Engineering and Design 236 (2006) 2237–2244. URL: https://linkinghub.elsevier.com/retrieve/pii/S0029549306003037. doi:10.1016/j.nucengdes.2006.03.055.

[8] C. R. B. Lister, On the Penetration of Water into Hot Rock, Geophysical Journal International 39 (1974) 465–509. URL: https://academic.oup.com/gji/article-lookup/doi/10.1111/j.1365-246X.1974.tb05468.x. doi:10.1111/j.1365-246X.1974.tb05468.x.

[9] M. Epstein, Dryout Heat Flux During Penetration of Water Into Solidifying Rock, Journal of Heat Transfer 128 (2006) 847. URL: http://HeatTransfer.asmedigitalcollection.asme.org/article.aspx?articleid=1448447. doi:10.1115/1.2227042.

[10] A. K. Nayak, R. K. Singh, P. P. Kulkarni, B. R. Sehgal, A numerical and experimental study of water ingression phenomena in melt pool coolability, Nuclear Engineering and Design 239 (2009) 1285–1293. URL: http://linkinghub.elsevier.com/retrieve/pii/S0029549309000934. doi:10.1016/j.nucengdes.2009.02.016.

[11] P. Kulkarni, A. Nayak, Study on coolability of melt pool with different strategies, Nuclear Engineering and Design 270 (2014) 379–388. URL: https://linkinghub.elsevier.com/retrieve/pii/S0029549314000867. doi:10.1016/j.nucengdes.2014.01.017.

[12] D. Y. Yeo, H. C. No, Modeling crust fracture and water ingression through crust during top-flooding strategy for corium cooling, Nuclear Engineering and Design 342 (2019) 219–230. URL: http://www.sciencedirect.com/science/article/pii/S0029549318308094. doi:10.1016/j.nucengdes.2018.12.004.

[13] A. A. Griffith, G. I. Taylor, VI. The phenomena of rupture and flow in solids, Philosophical Transactions of the Royal Society of London. Series A, Containing Papers of a Mathematical or Physical Character 221 (1921) 163–198. URL: https://royalsocietypublishing.org/doi/abs/10.1098/rsta.1921.0006. doi:10.1098/rsta.1921.0006.

[14] J. K. Fink, Thermophysical properties of uranium dioxide, Journal of Nuclear Materials 279 (2000) 1–18. URL: http://www.sciencedirect.com/science/article/pii/S0022311599002731. doi:10.1016/S0022-3115(99)00273-1.

[15] A. Seibert, D. Staicu, D. Bottomley, M. Cologna, J. Boshoven, H. Hein, E. Kassim, S. Nourry, M. Ernstberger, D. Robba, R. Konings, Thermophysical properties of U, Zr-oxides as prototypic corium materials, Journal of Nuclear Materials 520 (2019) 165–177. URL: https://linkinghub.elsevier.

com/retrieve/pii/S0022311518315861. doi:10.1016/j.jnucmat.2019.04.019.
[16] P. J. Berenson, Film-Boiling Heat Transfer From a Horizontal Surface, Journal of Heat Transfer 83 (1961) 351–356. URL: https://asmedigitalcollection.asme.org/heattransfer/article/83/3/351/430783/FilmBoiling-Heat-Transfer-From-a-Horizontal. doi:10.1115/1.3682280.
[17] M. Epstein, Review of Water Ingression Models, ACEX-TR-CD31 ACEX-TR-CD31, Fauske & Associates, 2000.
[18] A. Villarreal Larrauri, Analysis and modeling of ex-vessel underwater cooling processes of debris bed and molten corium pool in interaction with concrete, PhD Thesis, Université de Lorraine, 2020. URL: https://www.researchgate.net/publication/344025482_Analysis_and_modeling_of_ex-vessel_underwater_cooling_processes_of_debris_bed_and_molten_corium_pool_in_interaction_with_concrete.
[19] T. Ginsberg, J. Klein, J. Klages, C. E. Schwarz, J. C. Chen, Transient core-debris bed heat-removal experiments and analysis, Technical Report BNL-NUREG–31796, Brookhaven National Lab., 1982. URL: http://inis.iaea.org/Search/search.aspx?orig_q=RN:14746048.
[20] T. Ginsberg, J. Klein, J. Klages, Y. Sanborn, C. E. Schwarz, J. C. Chen, L. Wei, An Experimental and analytical investigation of quenching of superheated debris beds under top-reflood conditions. Final report, Technical Report NUREG/CR-4493; BNL-NUREG-51951, Brookhaven National Lab., Upton, NY (USA), 1986. URL: https://www.osti.gov/biblio/5912914-experimental-analytical-investigation-quenching-superheated-debris-beds-under-top-reflood-conditions-final-report.
[21] D. H. Cho, D. R. Armstrong, L. Bova, S. H. Chan, G. R. Thomas, Debris bed quenching studies, in: Proceedings of the international meeting on thermal nuclear reactor safety, volume 2, American Nuclear Society, Chicago, IL, USA, 1983, pp. 987–995. URL: http://inis.iaea.org/Search/search.aspx?orig_q=RN:14792410.
[22] P. G. Saffman, S. G. I. Taylor, The penetration of a fluid into a porous medium or Hele-Shaw cell containing a more viscous liquid, Proceedings of the Royal Society of London. Series A. Mathematical and Physical Sciences 245 (1958) 312–329. URL: https://royalsocietypublishing.org/doi/10.1098/rspa.1958.0085. doi:10.1098/rspa.1958.0085.
[23] H. Kull, Theory of the Rayleigh-Taylor instability, Physics Reports 206 (1991) 197–325. URL: https://linkinghub.elsevier.com/retrieve/pii/037015739190153D. doi:10.1016/0370-1573(91)90153-D.
[24] B. Raverdy, R. Meignen, L. Piar, S. Picchi, T. Janin, Capabilities of MC3D to investigate the coolability of corium debris beds, Nuclear Engineering and Design 319 (2017) 48–60. URL: http://linkinghub.elsevier.com/retrieve/pii/S0029549317301681. doi:10.1016/j.nucengdes.2017.04.005.
[25] A. W. Reed, K. R. Boldt, E. D. Gorham-Bergeron, R. J. Lipinski, T. R. Schmidt, DCC-1/DCC-2 degraded core coolability analysis, Technical Report NUREG/CR–4390-R3, Sandia National Labs., 1985. URL: http://inis.iaea.org/Search/search.aspx?orig_q=RN:17065530.
[26] M. Fourar, R. Lenormand, A new model for two-phase flows at high velocities through porous media and fractures, Journal of Petroleum Science and Engineering 30 (2001) 121–127. URL: http://linkinghub.elsevier.com/retrieve/pii/S0920410501001097. doi:10.1016/S0920-4105(01)00109-7.
[27] M. C. Leverett, Capillary Behavior in Porous Solids, Transactions of the AIME 142 (1941) 152–169. URL: https://www.onepetro.org/journal-paper/SPE-941152-G. doi:10.2118/941152-G.
[28] K. S. Udell, Heat transfer in porous media considering phase change and capillarity—the heat pipe effect, International Journal of Heat and Mass Transfer 28 (1985) 485–495. URL: https://linkinghub.elsevier.com/retrieve/pii/0017931085900821. doi:10.1016/0017-9310(85)90082-1.
[29] M. T. van Genuchten, A Closed-form Equation for Predicting the Hydraulic Conductivity of Unsaturated Soils1, Soil Science Society of America Journal 44 (1980) 892. URL: https://www.soils.org/publications/sssaj/abstracts/44/5/SS0440050892. doi:10.2136/sssaj1980.03615995004400050002x.
[30] R. J. Lipinski, Model for boiling and dryout in particle beds, Technical Report NUREG/CR–2646, Sandia National Labs., 1982. URL: http://inis.iaea.org/Search/search.aspx?orig_q=RN:14732098.

[31] D. A. DiCarlo, Stability of gravity-driven multiphase flow in porous media: 40 Years of advancements: Stability of Multiphase Gravity-Driven Flow, Water Resources Research 49 (2013) 4531–4544. URL: http://doi.wiley.com/10.1002/wrcr.20359. doi:10.1002/wrcr.20359.

[32] S. W. Jones, M. Epstein, S. G. Bankoff, D. R. Pedersen, Dryout heat fluxes in particulate beds heated through the base, Journal of heat transfer 106 (1984) 176–183.

[33] H. C. Hardee, R. H. Nilson, Natural Convection in Porous Media with Heat Generation, Nuclear Science and Engineering 63 (1977) 119–132. URL: https://www.tandfonline.com/doi/full/10.13182/NSE77-A27015. doi:10.13182/NSE77-A27015.

[34] R. Meignen, S. Picchi, J. Lamome, B. Raverdy, S. Castrillon-Escobar, G. Nicaise, The challenge of modeling fuel coolant interaction: Part I – Premixing, Nuclear Engineering and Design 280 (2014) 511–527. URL: http://www.sciencedirect.com/science/article/pii/S0029549314005056. doi:10.1016/j.nucengdes.2014.08.029.

[35] J. Kokalj, M. Uršič, M. Leskovar, L. Piar, R. Meignen, Modelling of debris bed reflooding in PEARL experimental facility with MC3D code, Nuclear Engineering and Design 330 (2018) 450–462. URL: http://www.sciencedirect.com/science/article/pii/S0029549318301286. doi:10.1016/j.nucengdes.2018.02.016.

[36] S. Ergun, Fluid flow through packed columns, Chem. Eng. Prog. 48 (1952) 89–94. URL: http://dns2.asia.edu.tw/~ysho/YSHO-English/1000%20CE/PDF/Che%20Eng%20Pro48,%2089.pdf.

[37] B. Cheynet, NUCLEA, 2007. URL: https://hal.archives-ouvertes.fr/hal-00165418.

[38] J.-H. Kim, I.-K. Park, S.-W. Hong, B.-T. Min, S.-H. Hong, J.-H. Song, H.-D. Kim, Steam Explosion Experiments Using Nuclear Reactor Materials in the TROI Facilities, Heat Transfer Engineering 29 (2008) 748–756. URL: https://doi.org/10.1080/01457630801981796. doi:10.1080/01457630801981796.

[39] V. Tyrpekl, Material effect in the fuel-coolant interaction: structural characterization of the steam explosion debris and solidification mechanism, Ph.D. thesis, Université de Strasbourg, 2012.

[40] L. J. Siefken, E. W. Coryell, E. A. Harvego, J. K. Hohorst, SCDAP/RELAP5/MOD 3.3 Code Manual: MATPRO - A Library of Materials Properties for Light-Water-Reactor Accident Analysis, Code Manual, Idaho National Engineering and Environmental Laboratory, 2001. URL: https://www.nrc.gov/docs/ML0103/ML010330363.pdf.

[41] O. Bahr, P. Schaumann, B. Bollen, J. Bracke, Young's modulus and Poisson's ratio of concrete at high temperatures: Experimental investigations, Materials & Design 45 (2013) 421–429. URL: http://www.sciencedirect.com/science/article/pii/S0261306912005225. doi:10.1016/j.matdes.2012.07.070.

[42] E. Nonnet, N. Lequeux, P. Boch, Elastic properties of high alumina cement castables from room temperature to 1600 C, Journal of the European Ceramic Society 19 (1999) 1575–1583. URL: http://www.sciencedirect.com/science/article/pii/S0955221998002556. doi:10.1016/S0955-2219(98)00255-6.

[43] E. Gregorová, M. Černý, W. Pabst, L. Esposito, C. Zanelli, J. Hamáček, J. Kutzendörfer, Temperature dependence of Young's modulus of silica refractories, Ceramics International 41 (2015) 1129–1138. URL: http://www.sciencedirect.com/science/article/pii/S0272884214014242. doi:10.1016/j.ceramint.2014.09.039.

[44] A. Alnuaim, W. Hamid, A. Alshenawy, Unconfined Compressive Strength and Young's Modulus of Riyadh Limestone, Electronic Journal of Geotechnical Engineering 24 (2019) 12.

[45] J. Delacroix, C. Journeau, N. Chikhi, P. Fouquart, D. Zhan, Measurements of in-vessel and ex-vessel liquid corium surface tension and density in the VITI-MBP test bench within ALISA Euro-Chinese project, Mechanical Engineering Journal 7 (2020) 19–00611–19–00611. doi:10.1299/mej.19-00611.

[46] R. F. Canon, J. T. A. Roberts, R. J. Beals, Deformation of UO2 at High Temperatures, Journal of the American Ceramic Society 54 (1971) 105–112. URL: https://ceramics.onlinelibrary.wiley.com/doi/abs/10.1111/j.1151-2916.1971.tb12230.x. doi:10.1111/j.1151-2916.1971.tb12230.x, _eprint: https://ceramics.onlinelibrary.wiley.com/doi/pdf/10.1111/j.1151-2916.1971.tb12230.x.

[47] L. F. Faria Ricardo, D. Leguillon, G. Parry, A. Doitrand, Modeling the thermal shock induced cracking in ceramics, Journal of the European Ceramic Society (2019)

S0955221919308167. URL: https://linkinghub.elsevier.com/retrieve/pii/S0955221919308167. doi:10.1016/j.jeurceramsoc.2019.11.071.

[48] H.-A. Bahr, H.-J. Weiss, U. Bahr, M. Hofmann, G. Fischer, S. Lampenscherf, H. Balke, Scaling behavior of thermal shock crack patterns and tunneling cracks driven by cooling or drying, Journal of the Mechanics and Physics of Solids 58 (2010) 1411–1421. URL: https://linkinghub.elsevier.com/retrieve/pii/S0022509610000955. doi:10.1016/j.jmps.2010.05.005.

[49] P. Combis, P. Cormont, L. Gallais, D. Hebert, L. Robin, J.-L. Rullier, Evaluation of the fused silica thermal conductivity by comparing infrared thermometry measurements with two-dimensional simulations, Applied Physics Letters 101 (2012) 211908. URL: http://aip.scitation.org/doi/10.1063/1.4764904. doi:10.1063/1.4764904.

figure

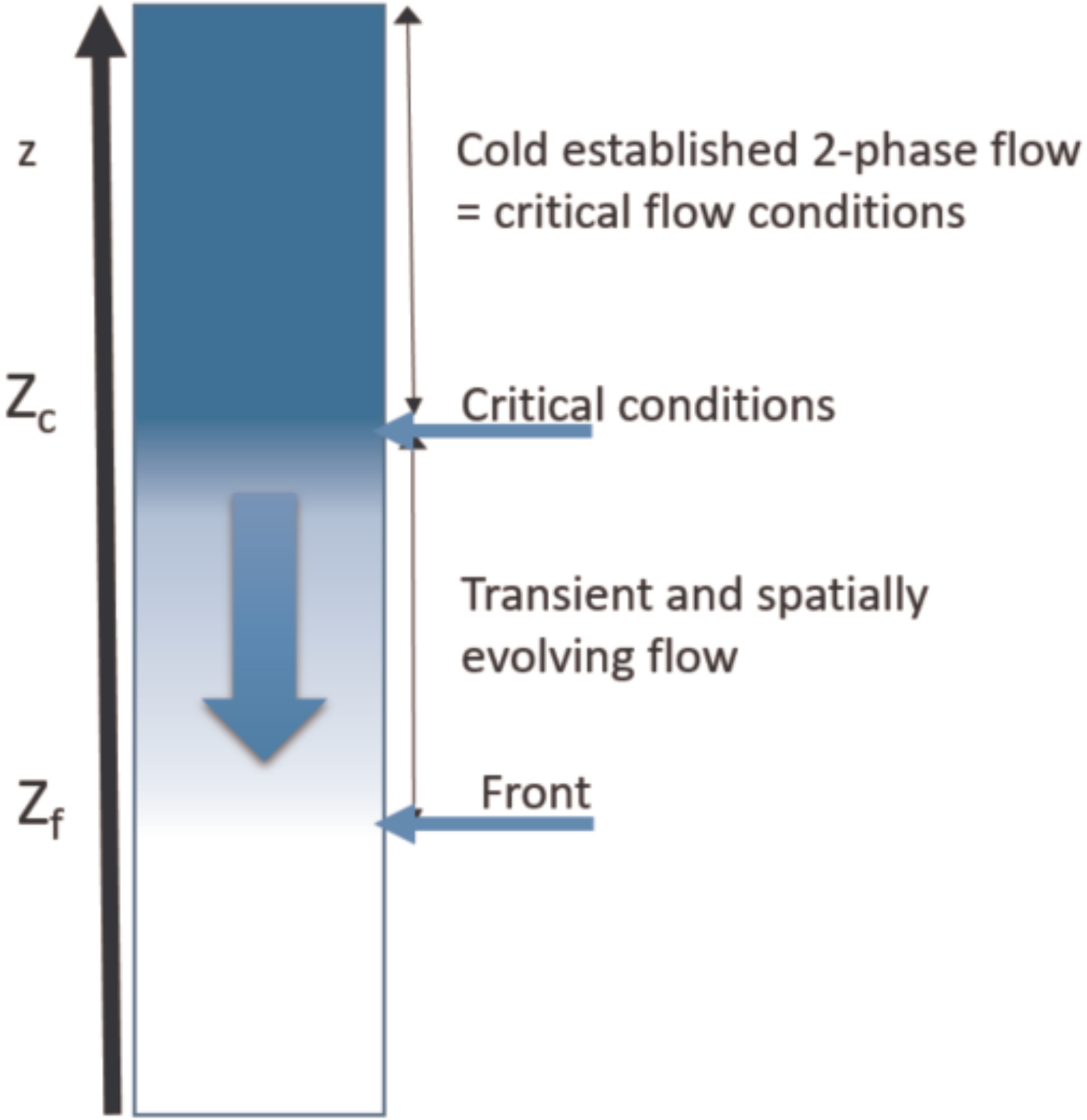
z
Z_c
Z_f
Cold established 2-phase flow
= critical flow conditions
Critical conditions
Transient and spatially
evolving flow
Front

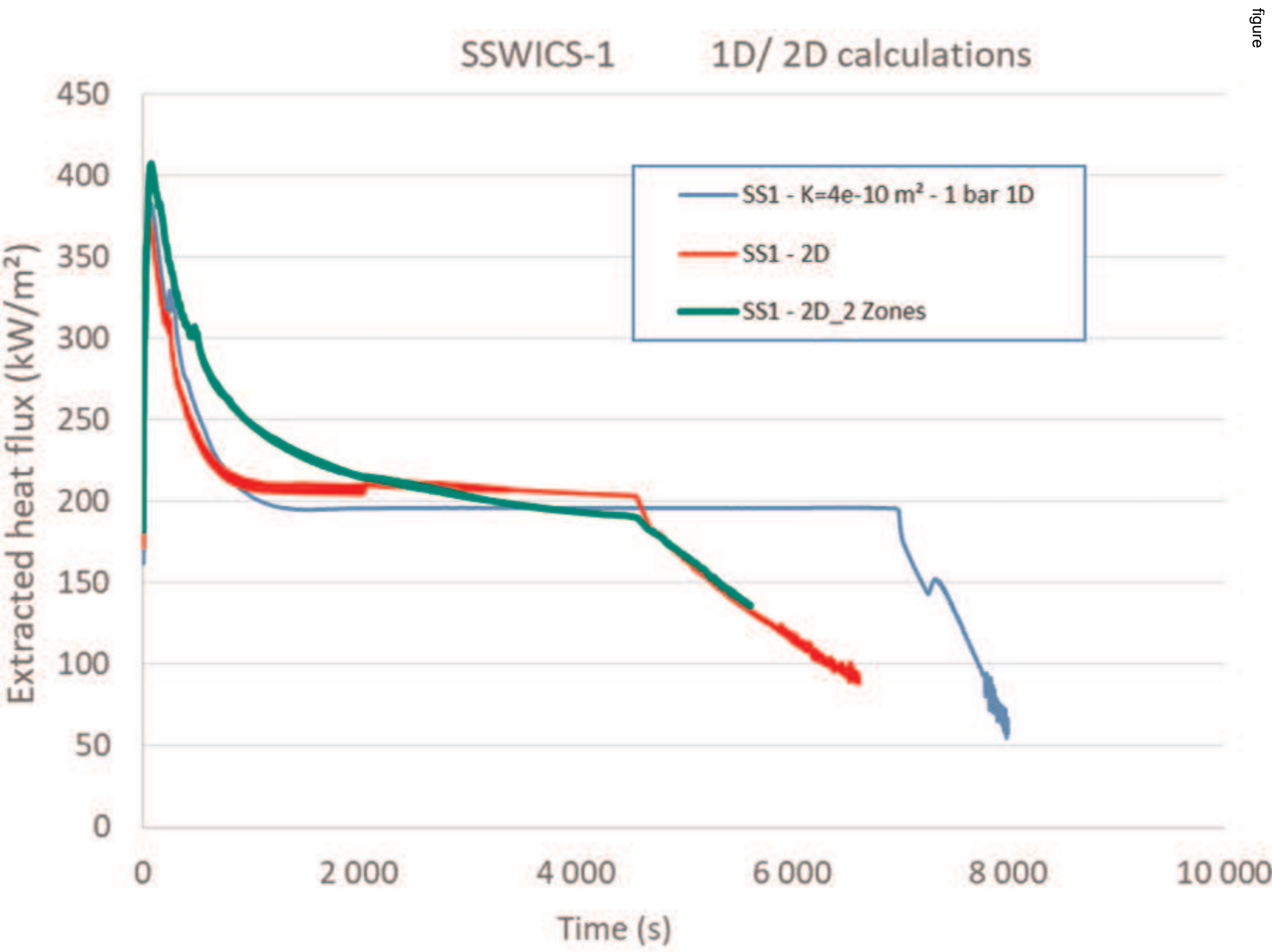
SSWICS-1 1D/ 2D calculations
Extracted heat flux (kW/m²)
Time (s)
SS1 - K=4e-10 m² - 1 bar 1D
SS1 - 2D
SS1 - 2D_2 Zones
450
400
350
300
250
200
150
100
50
0
0
2 000
4 000
6 000
8 000
10 000

figure

figure

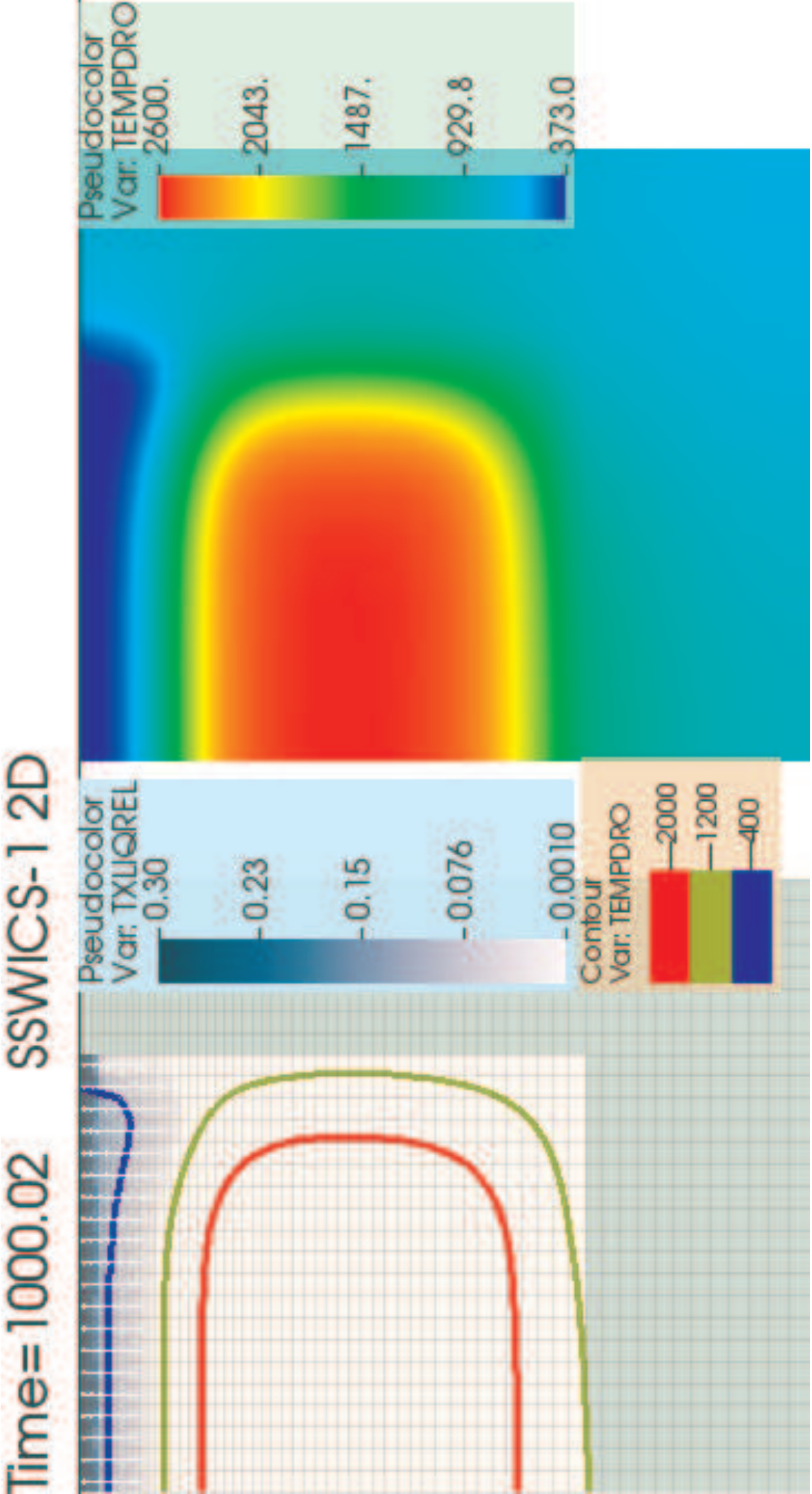
Time=1000.02
SSWICS-1 2D
Pseudocolor
Var: TXLIQREL
0.30
0.23
0.15
0.076
0.0010
Pseudocolor
Var: TEMPDRO
2600.
2043.
1487.
929.8
373.0
Contour
Var: TEMPDRO
2000
1200
400

figure

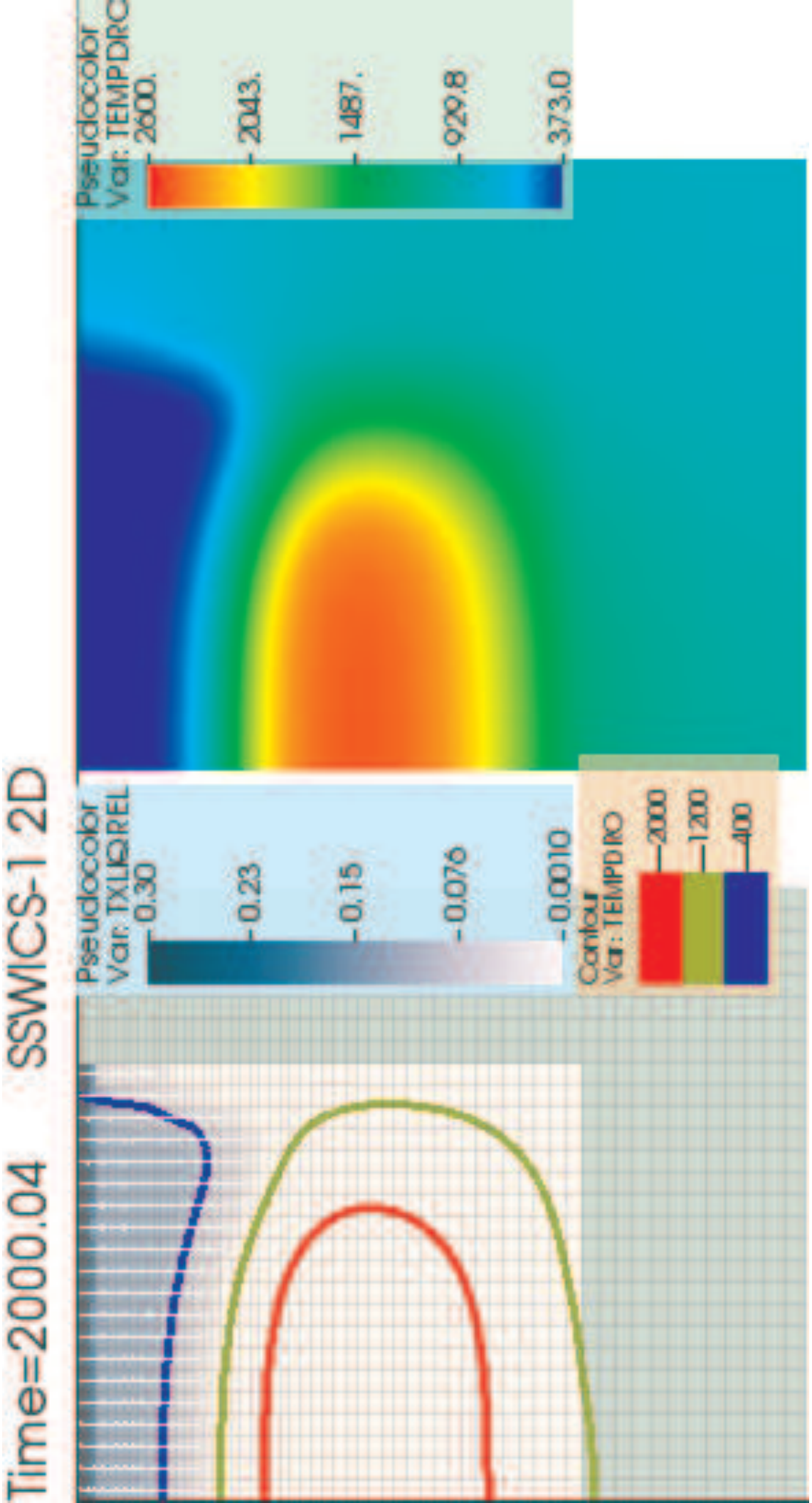
Time=2000.04
SSWICS-1 2D
Pseudocolor
Var: TEMPDRO
2600.
2043.
1487.
929.8
373.0
Pseudocolor
Var: TXLIQREL
0.30
0.23
0.15
0.076
0.0010
Contour
Var: TEMPDRO
2000
1200
400

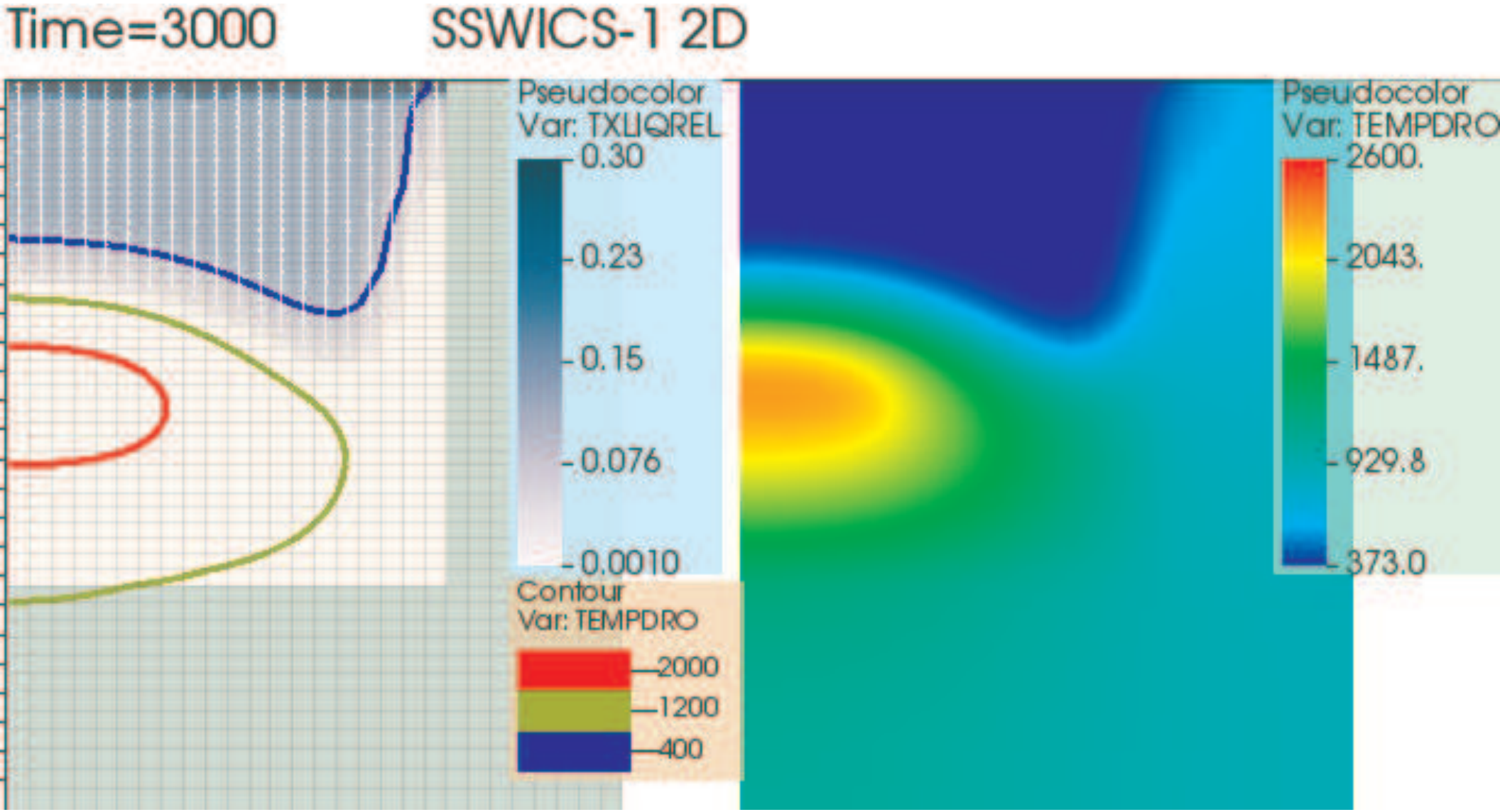
Time=3000
SSWICS-1 2D
Pseudocolor
Var: TXLIQREL
0.30
0.23
0.15
0.076
0.0010
Contour
Var: TEMPDRO
2000
1200
400
Pseudocolor
Var: TEMPDRO
2600.
2043.
1487.
929.8
373.0

figure

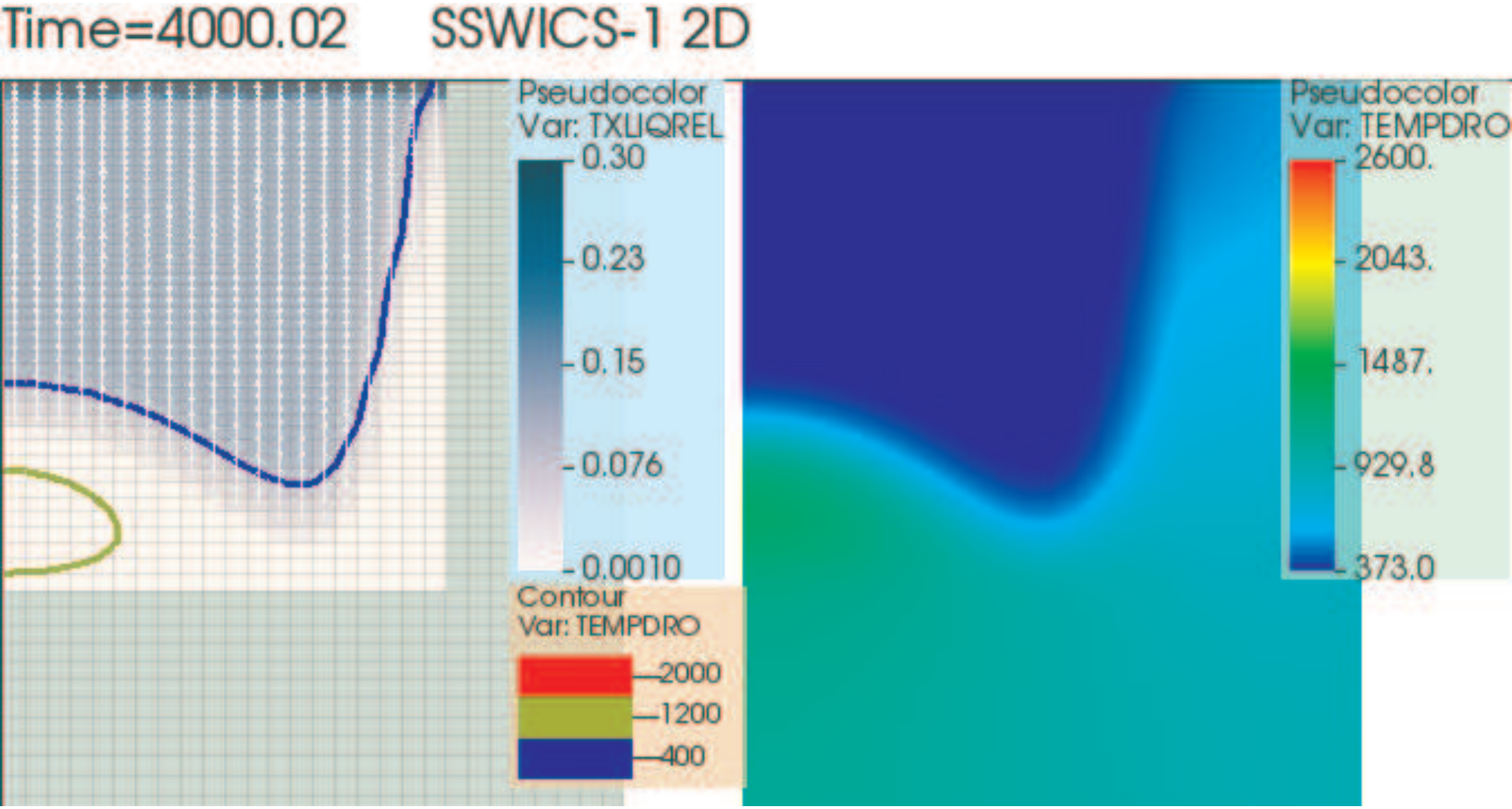
Time=4000.02
SSWICS-1 2D
Pseudocolor
Var: TXLIQREL
0.30
0.23
0.15
0.076
0.0010
Contour
Var: TEMPDRO
2000
1200
400
Pseudocolor
Var: TEMPDRO
2600.
2043.
1487.
929.8
373.0

figure

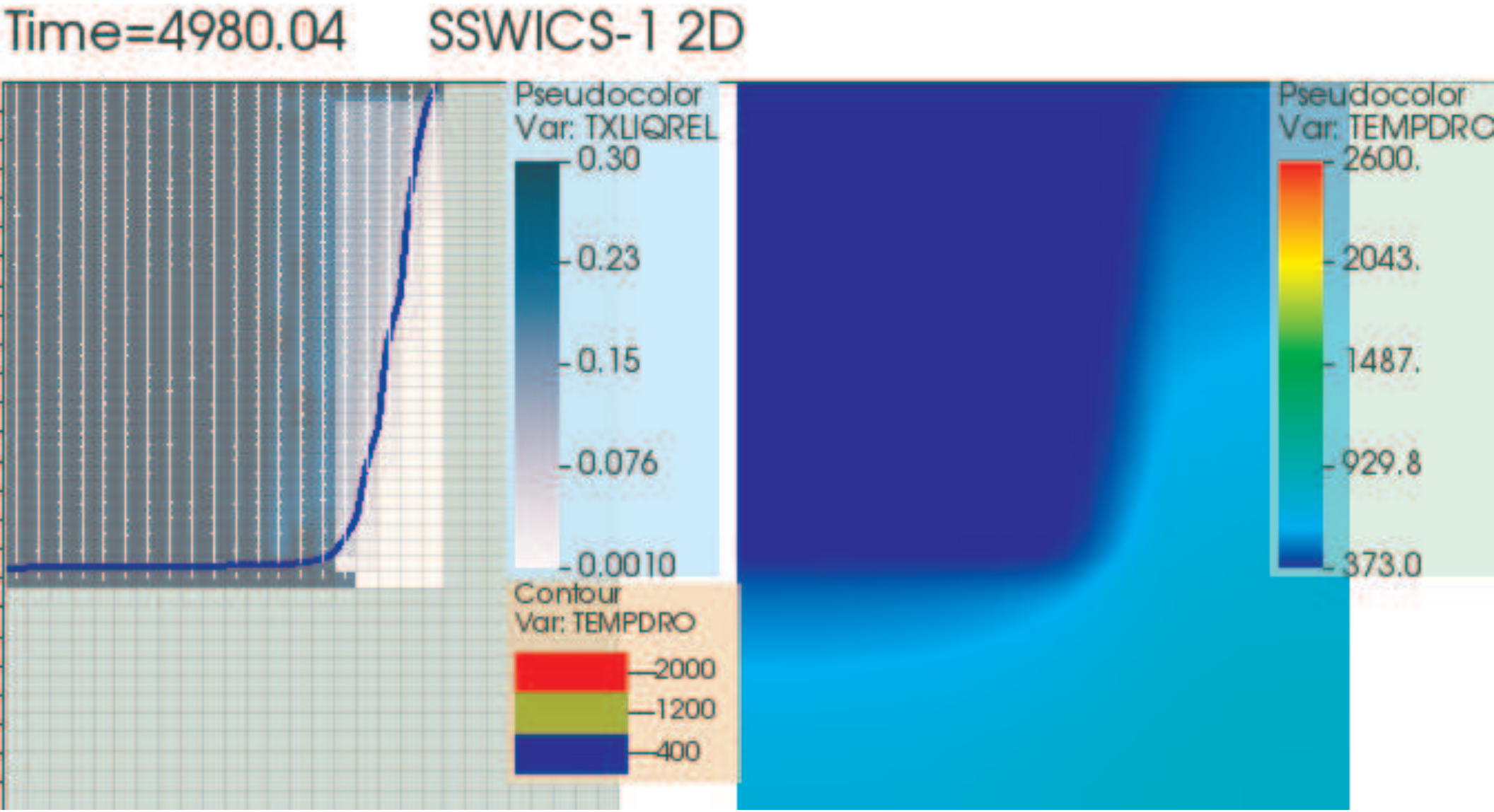
Time=4980.04
SSWICS-1 2D
Pseudocolor
Var: TXLIQREL
0.30
0.23
0.15
0.076
0.0010
Contour
Var: TEMPDRO
2000
1200
400
Pseudocolor
Var: TEMPDRO
2600.
2043.
1487.
929.8
373.0

figure

figure

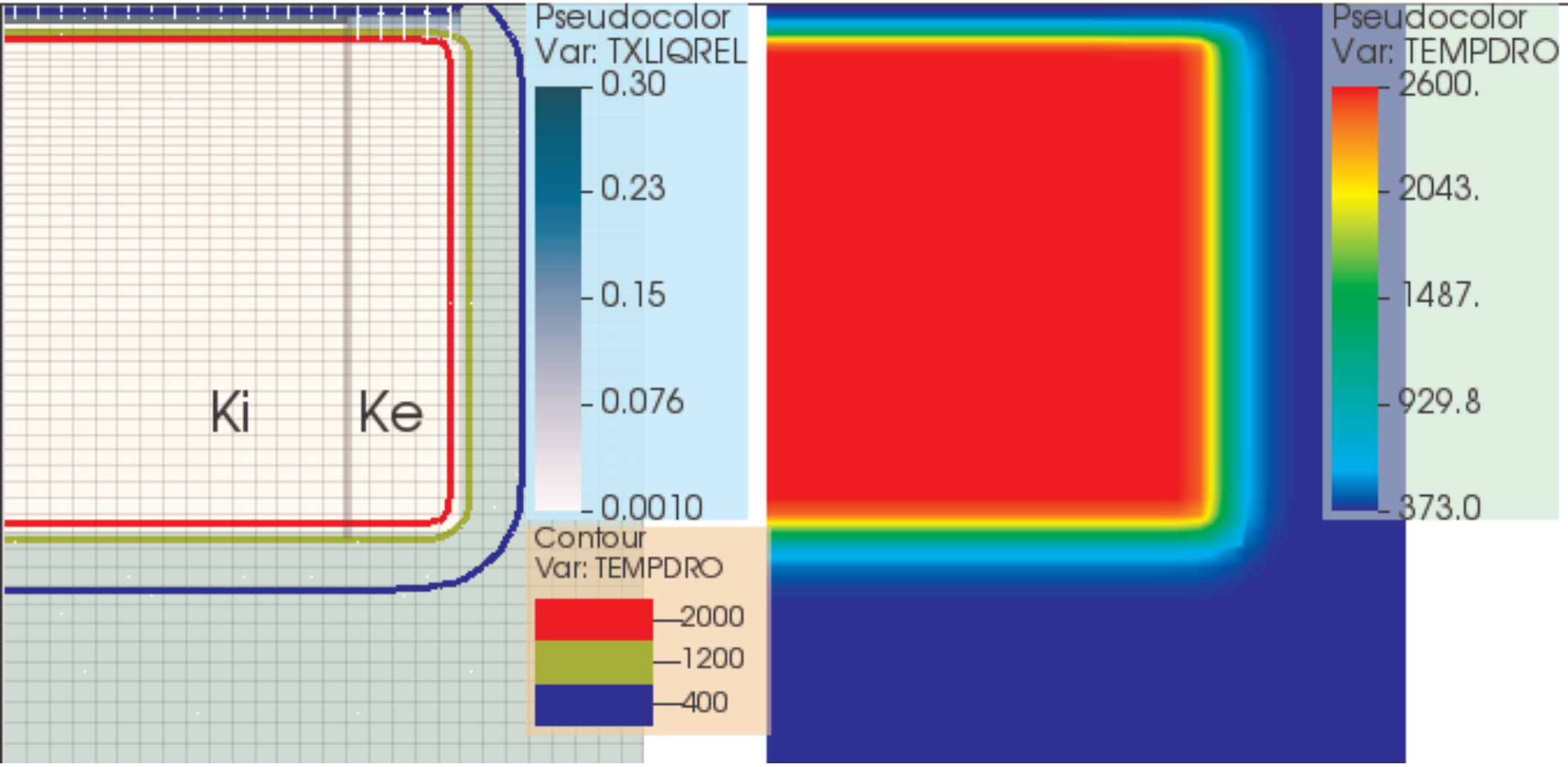
Time=5.00024
SSWICS-1 2D 2 zones for K
Pseudocolor
Var: TXLIQREL
0.30
0.23
0.15
0.076
0.0010
Ki
Ke
Contour
Var: TEMPDRO
2000
1200
400
Pseudocolor
Var: TEMPDRO
2600.
2043.
1487.
929.8
373.0

figure

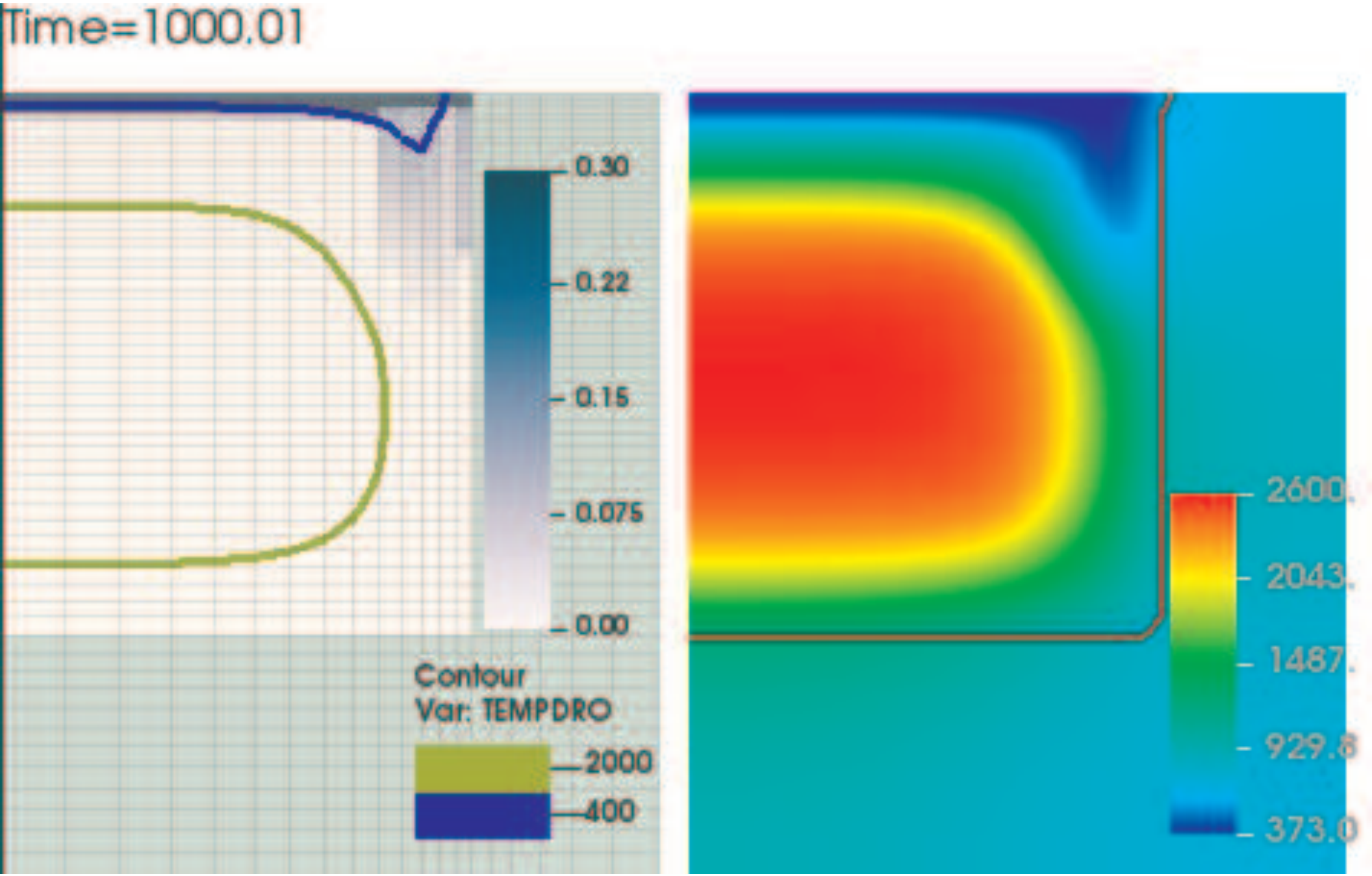
Time=1000.01
0.30
0.22
0.15
0.075
0.00
Contour
Var: TEMPDRO
2000
400
2600.
2043.
1487.
929.8
373.0

figure

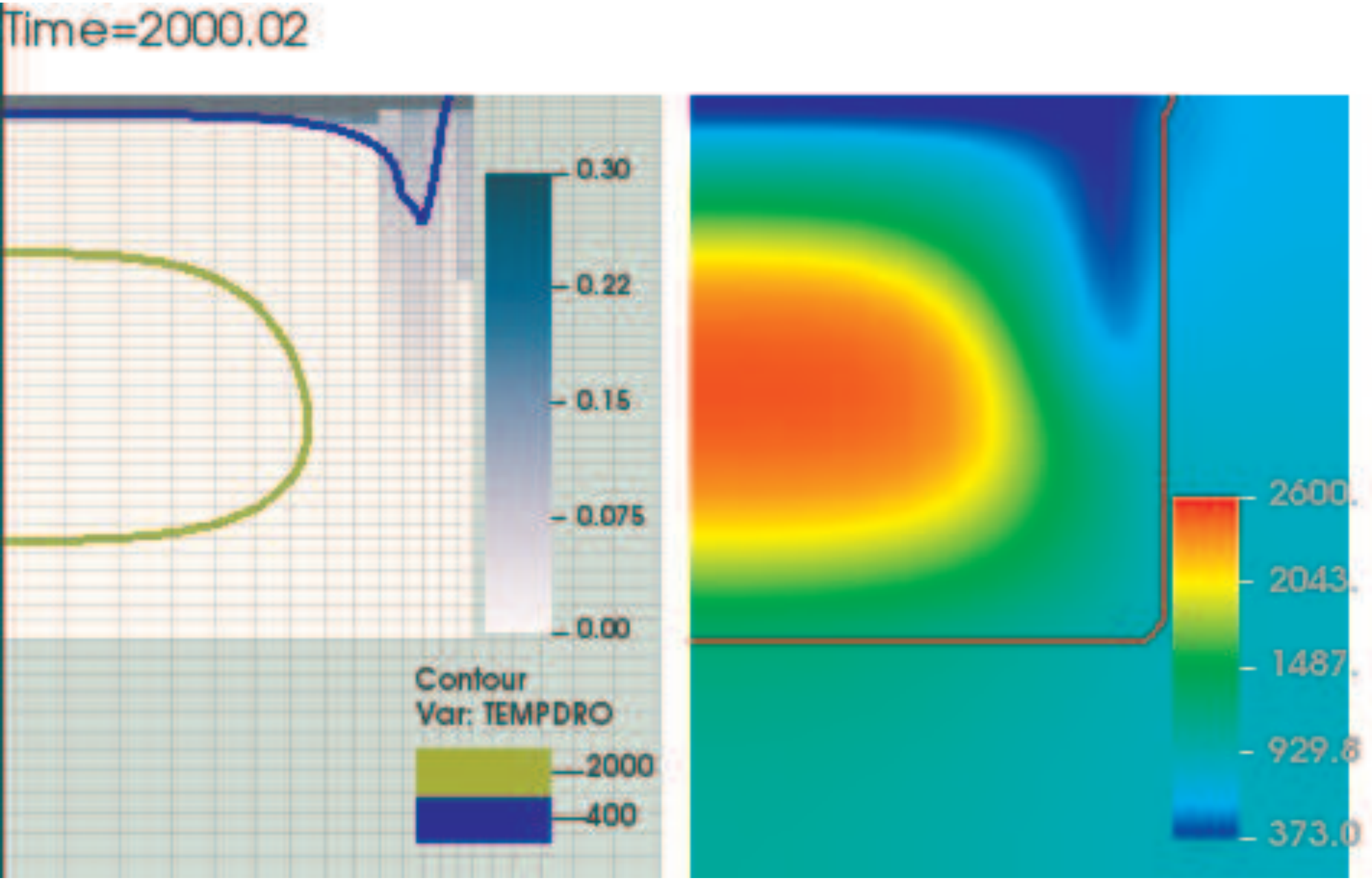
Time=2000.02
0.30
0.22
0.15
0.075
0.00
Contour
Var: TEMPDRO
2000
400
2600.
2043.
1487.
929.6
373.0

figure

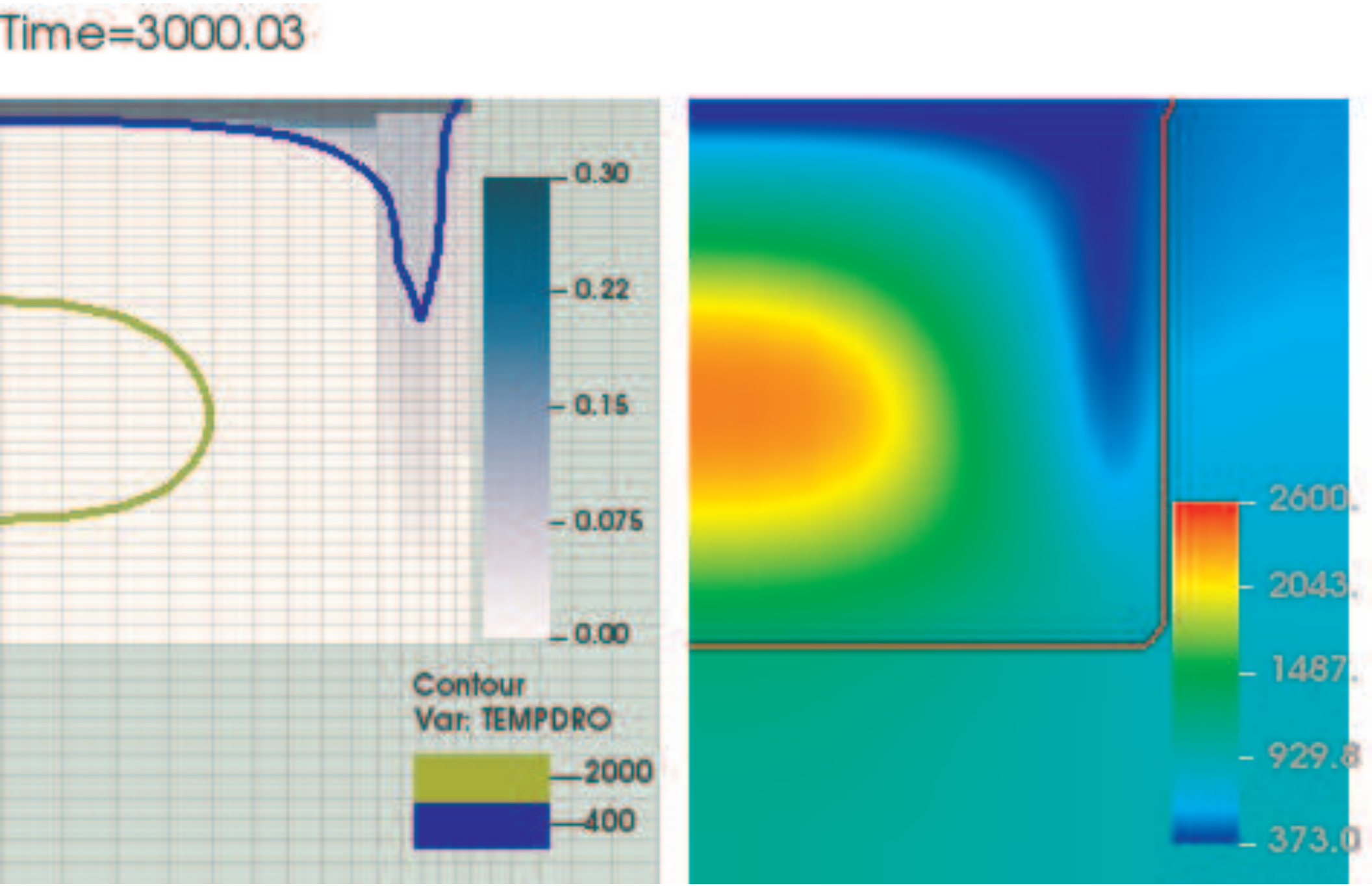
Time=3000.03
0.30
0.22
0.15
0.075
0.00
Contour
Var: TEMPDRO
2000
400
2600.
2043.
1487.
929.8
373.0

figure

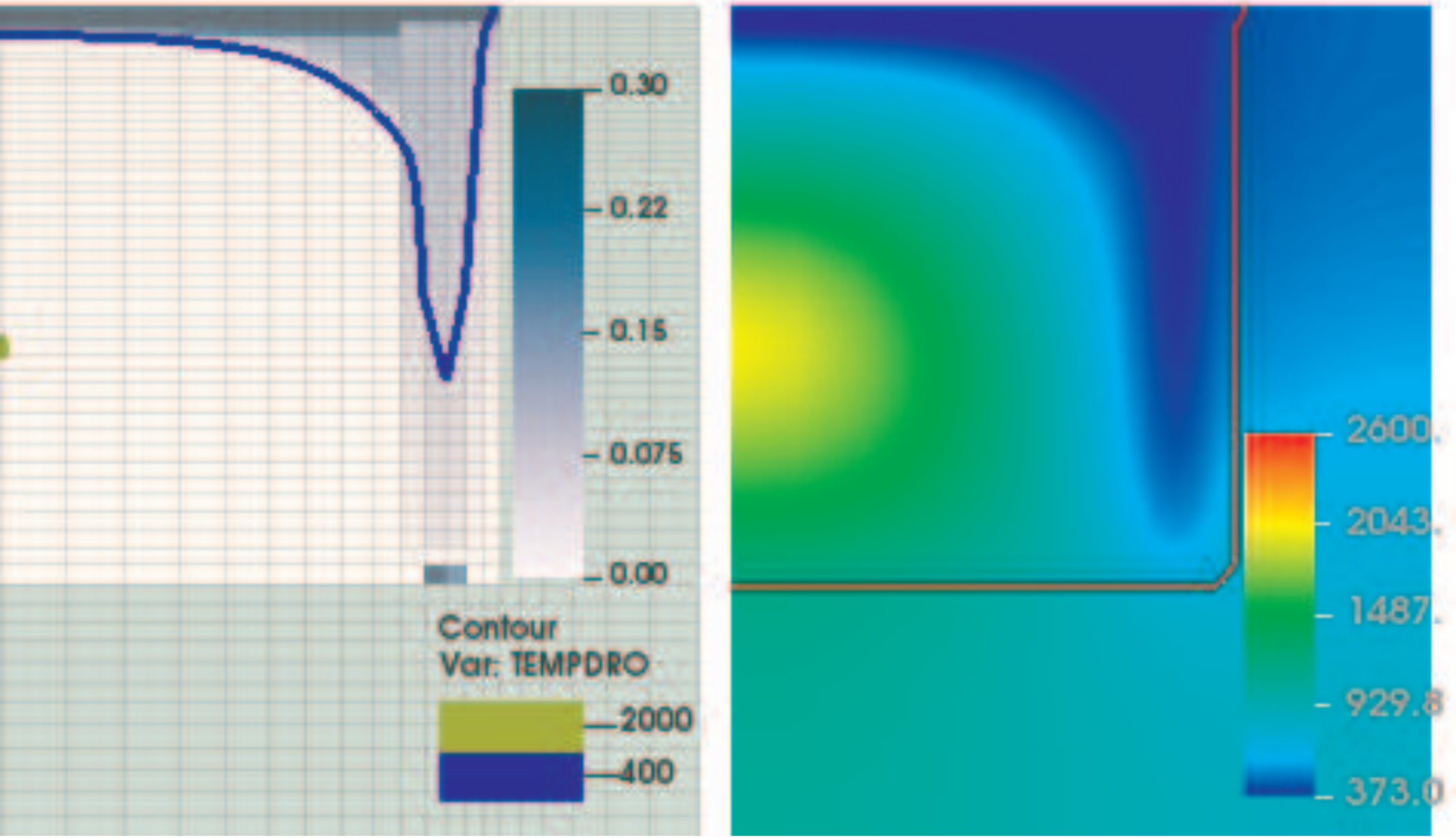
Time=4000.04
0.30
0.22
0.15
0.075
0.00
Contour
Var: TEMPDRO
2000
400
2600.
2043.
1487.
929.8
373.0

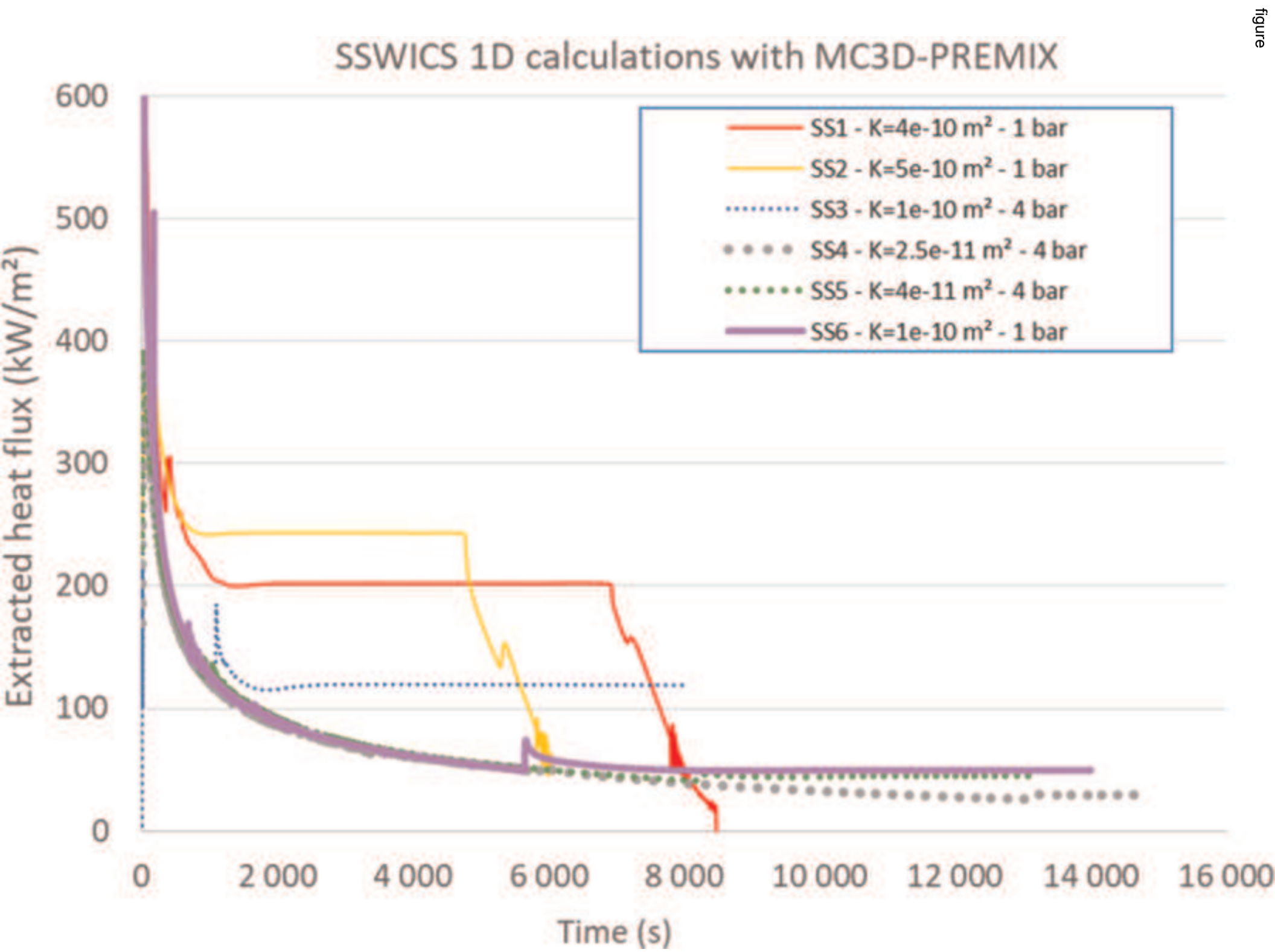
SSWICS 1D calculations with MC3D-PREMIX
SS1 - K=4e-10 m² - 1 bar
SS2 - K=5e-10 m² - 1 bar
SS3 - K=1e-10 m² - 4 bar
SS4 - K=2.5e-11 m² - 4 bar
SS5 - K=4e-11 m² - 4 bar
SS6 - K=1e-10 m² - 1 bar
Extracted heat flux (kW/m²)
600
500
400
300
200
100
0
0
2 000
4 000
6 000
8 000
10 000
12 000
14 000
16 000
Time (s)

figure

figure

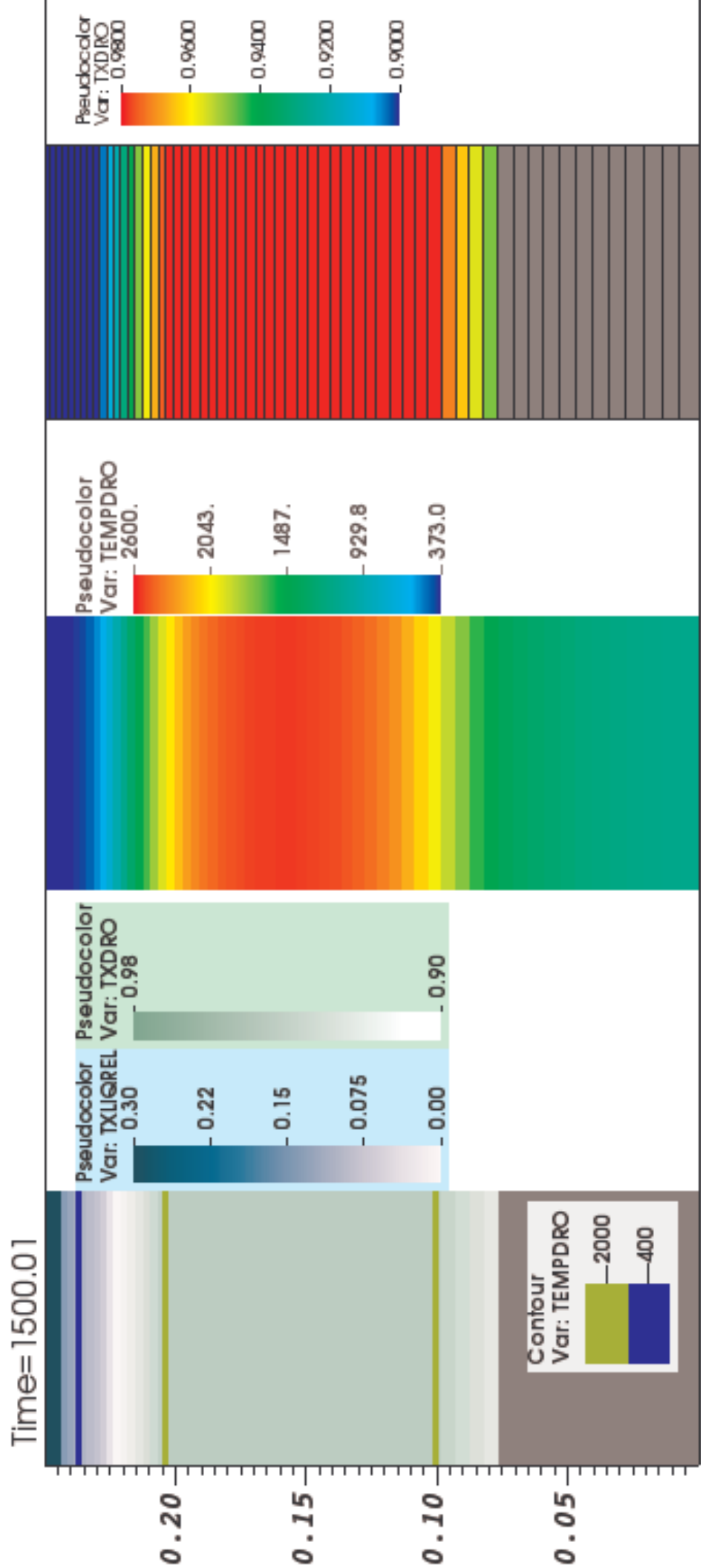
Time=1500.01
Pseudocolor
Var: TXLI@REL
0.30
0.22
0.15
0.075
0.00
Pseudocolor
Var: TXDRO
0.98
0.90
Contour
Var: TEMPDRO
2000
400
Pseudocolor
Var: TEMPDRO
2600.
2043.
1487.
929.8
373.0
Pseudocolor
Var: TXDRO
0.9800
0.9600
0.9400
0.9200
0.9000
0.20
0.15
0.10
0.05

figure

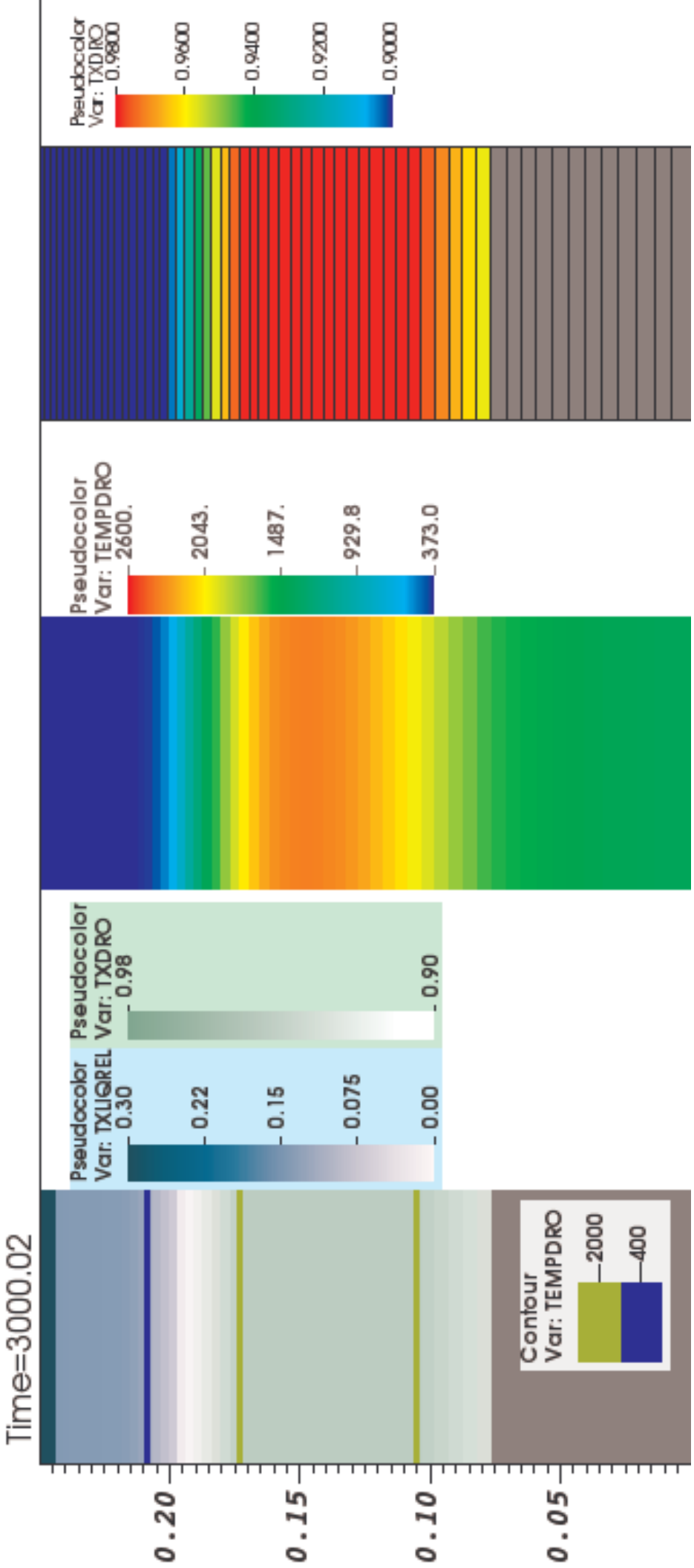
Time=3000.02
0.20
0.15
0.10
0.05
Contour
Var: TEMPDRO
2000
400
Pseudocolor
Var: TXLIQREL
0.30
0.22
0.15
0.075
0.00
Pseudocolor
Var: TXDRO
0.98
0.90
Pseudocolor
Var: TEMPDRO
2600.
2043.
1487.
929.8
373.0
Pseudocolor
Var: TXDRO
0.9800
0.9600
0.9400
0.9200
0.9000

figure

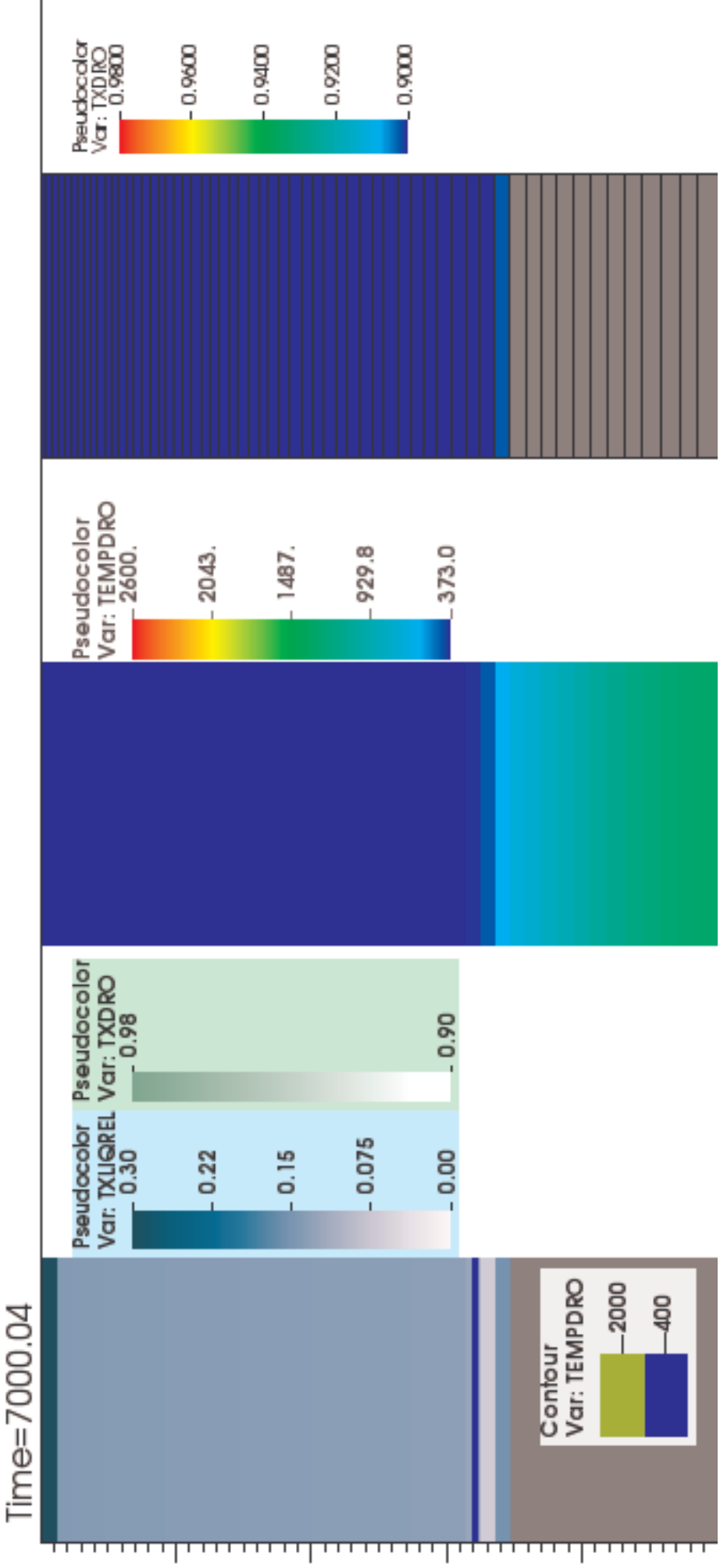
Time=7000.04
Pseudocolor
Var: TXDRO
0.9800
0.9600
0.9400
0.9200
0.9000
Pseudocolor
Var: TEMPDRO
2600.
2043.
1487.
929.8
373.0
Pseudocolor
Var: TXDRO
0.98
0.90
Pseudocolor
Var: TXLIQREL
0.30
0.22
0.15
0.075
0.00
Contour
Var: TEMPDRO
2000
400
0.20
0.15
0.10
0.05

figure

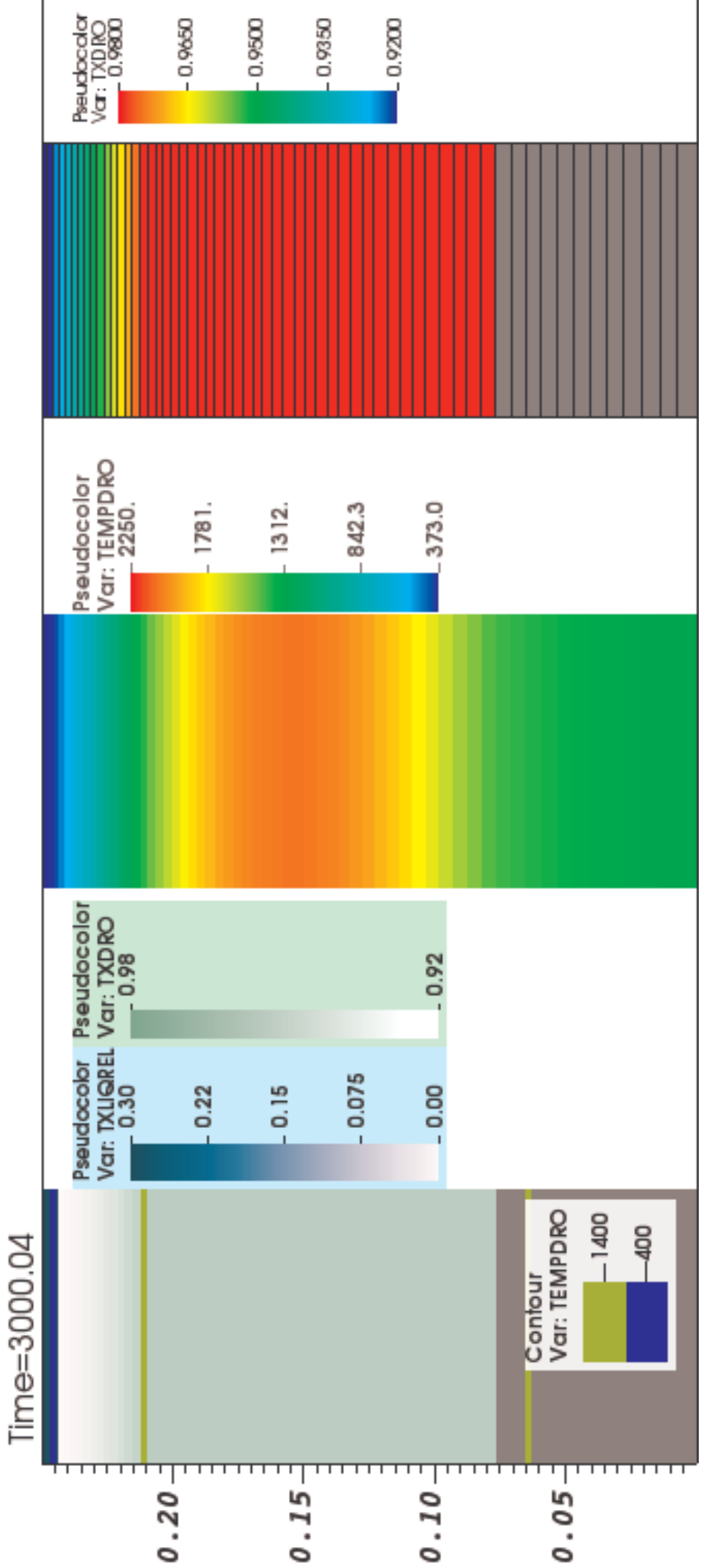
Time=3000.04
Pseudocolor
Var: TXDRO
0.9800
0.9650
0.9500
0.9350
0.9200
Pseudocolor
Var: TEMPDRO
2250.
1781.
1312.
842.3
373.0
Pseudocolor
Var: TXDRO
0.98
0.92
Pseudocolor
Var: TXLIQREL
0.30
0.22
0.15
0.075
0.00
Contour
Var: TEMPDRO
1400
400
0.20
0.15
0.10
0.05

figure

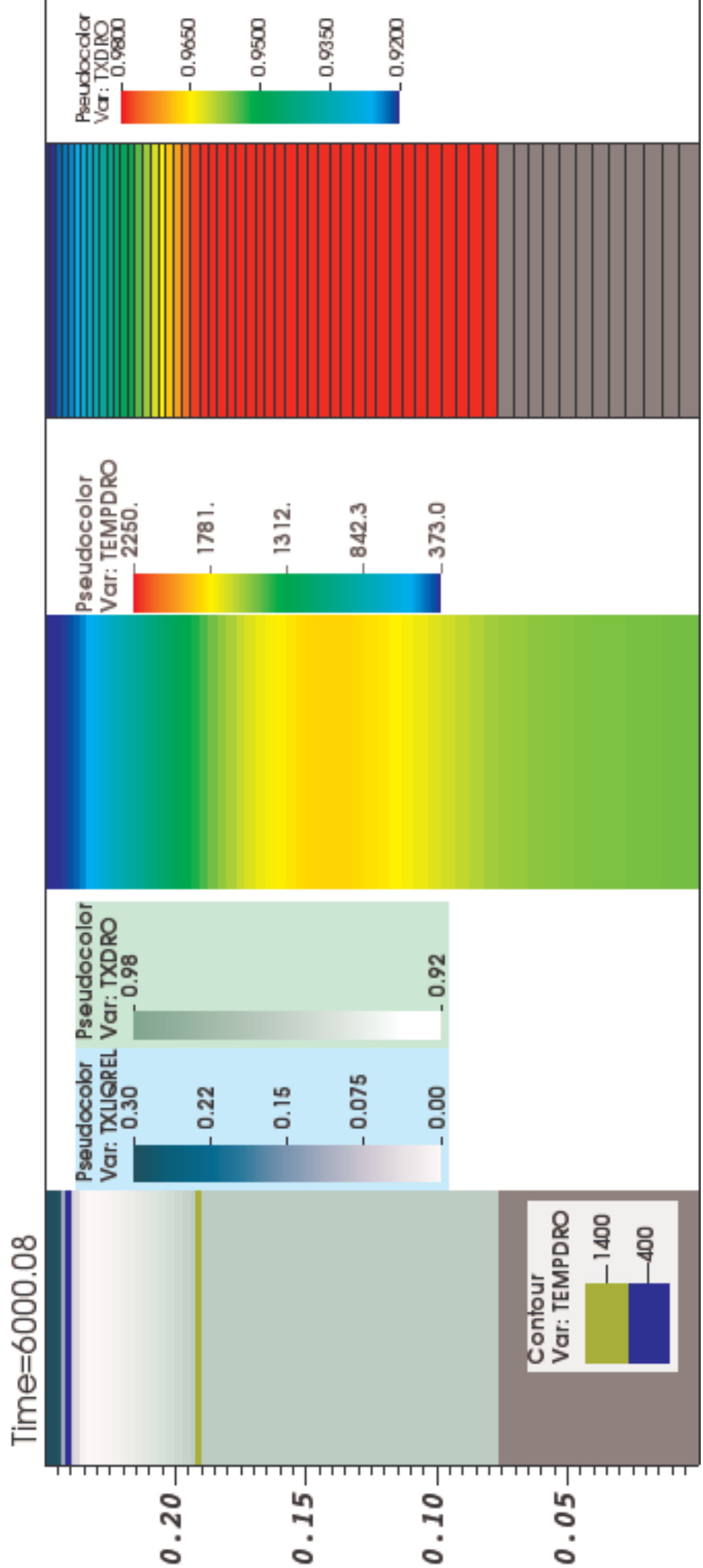
Time=6000.08
0.20
0.15
0.10
0.05
Pseudocolor
Var: TXLI@REL
0.30
0.22
0.15
0.075
0.00
Pseudocolor
Var: TXDRO
0.98
0.92
Contour
Var: TEMPDRO
1400
400
Pseudocolor
Var: TEMPDRO
2250.
1781.
1312.
842.3
373.0
Pseudocolor
Var: TXDRO
0.9800
0.9650
0.9500
0.9350
0.9200

figure

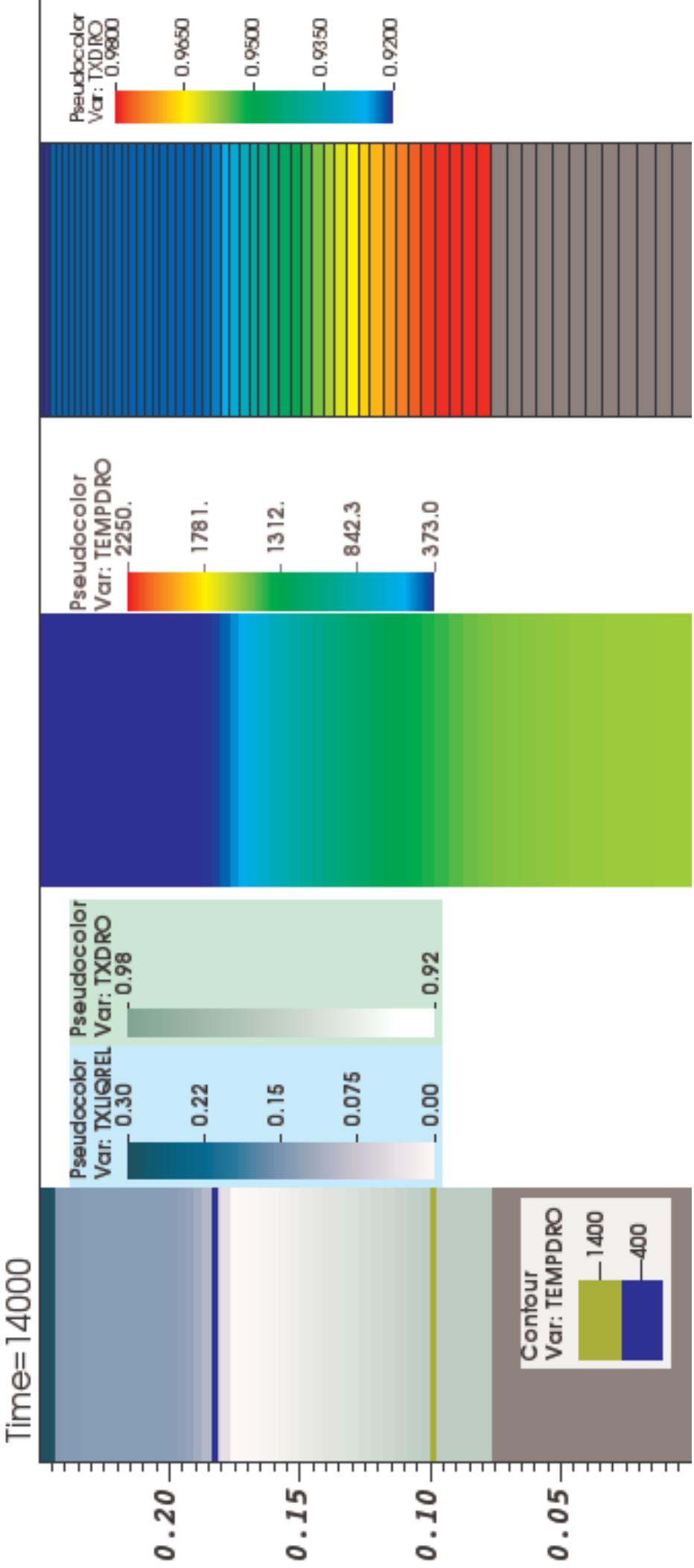
Time=14000
0.20
0.15
0.10
0.05
Contour
Var: TEMPDRO
1400
400
Pseudocolor
Var: TXLIQREL
0.30
0.22
0.15
0.075
0.00
Pseudocolor
Var: TXDRO
0.98
0.92
Pseudocolor
Var: TEMPDRO
2250.
1781.
1312.
842.3
373.0
Pseudocolor
Var: TXDRO
0.9800
0.9650
0.9500
0.9350
0.9200

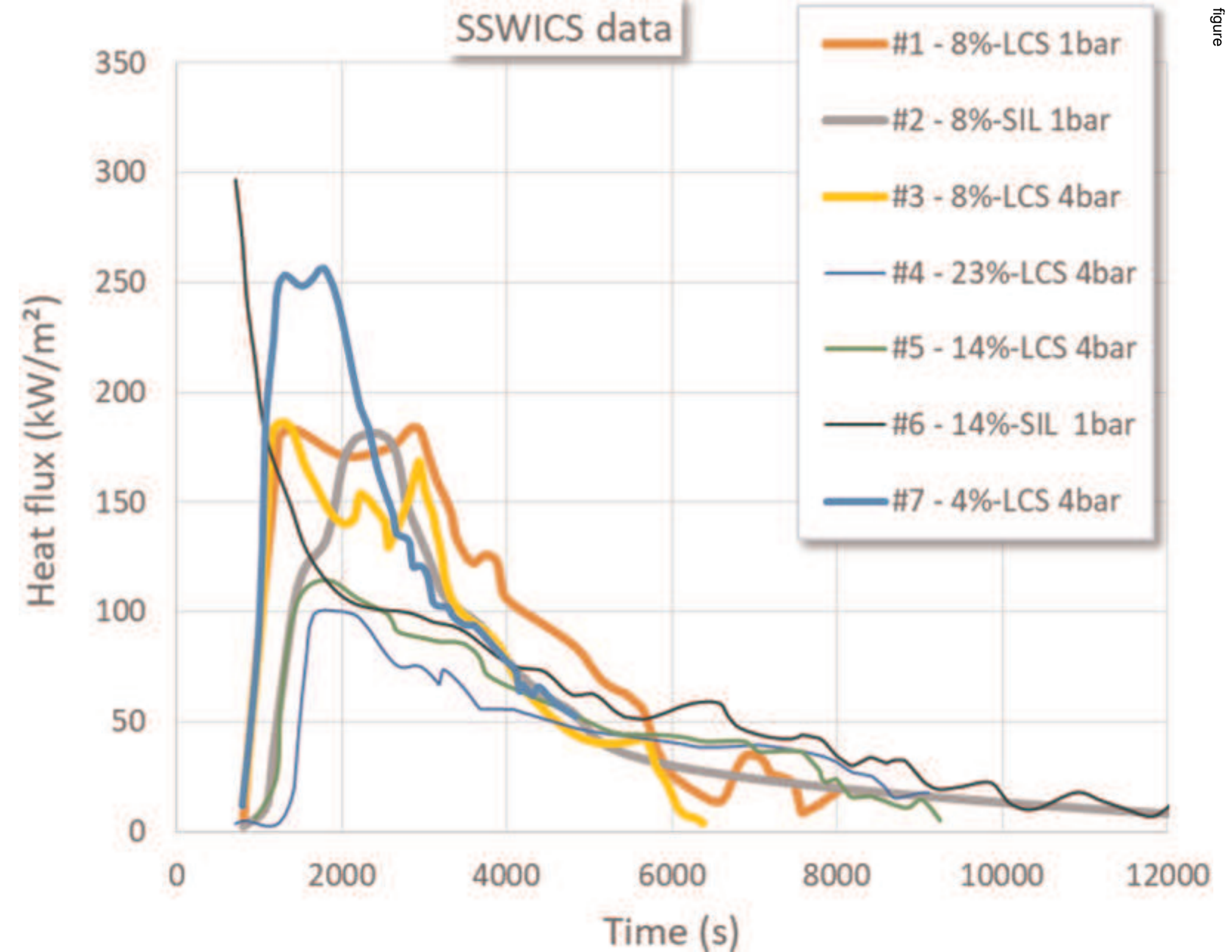
SSWICS data
#1 - 8%-LCS 1bar
#2 - 8%-SIL 1bar
#3 - 8%-LCS 4bar
#4 - 23%-LCS 4bar
#5 - 14%-LCS 4bar
#6 - 14%-SIL 1bar
#7 - 4%-LCS 4bar
Heat flux (kW/m²)
350
300
250
200
150
100
50
0
0
2000
4000
6000
8000
10000
12000
Time (s)
figure

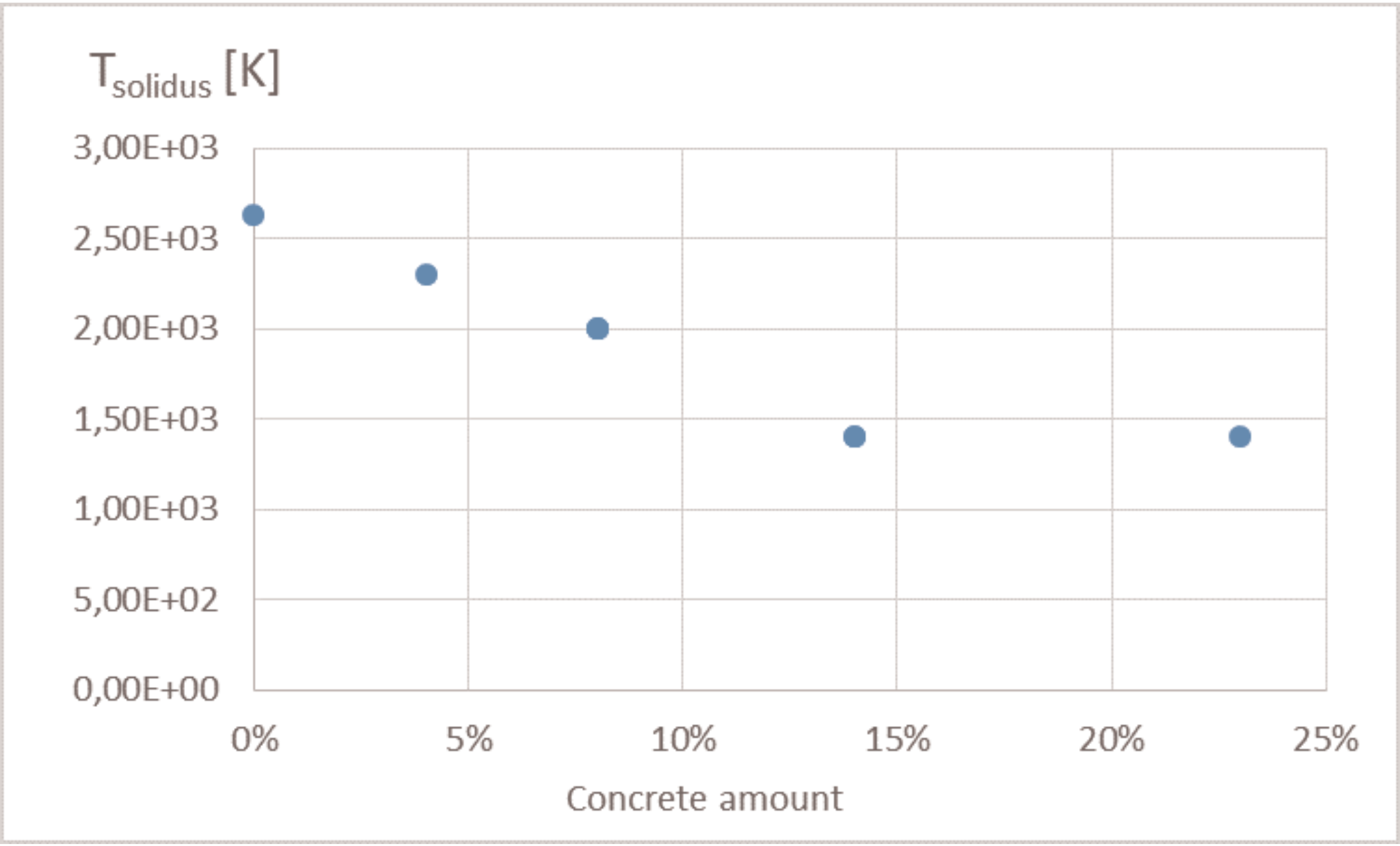
$T_{solidus}$ [K]
3,00E+03
2,50E+03
2,00E+03
1,50E+03
1,00E+03
5,00E+02
0,00E+00
0%
5%
10%
15%
20%
25%
Concrete amount

figure

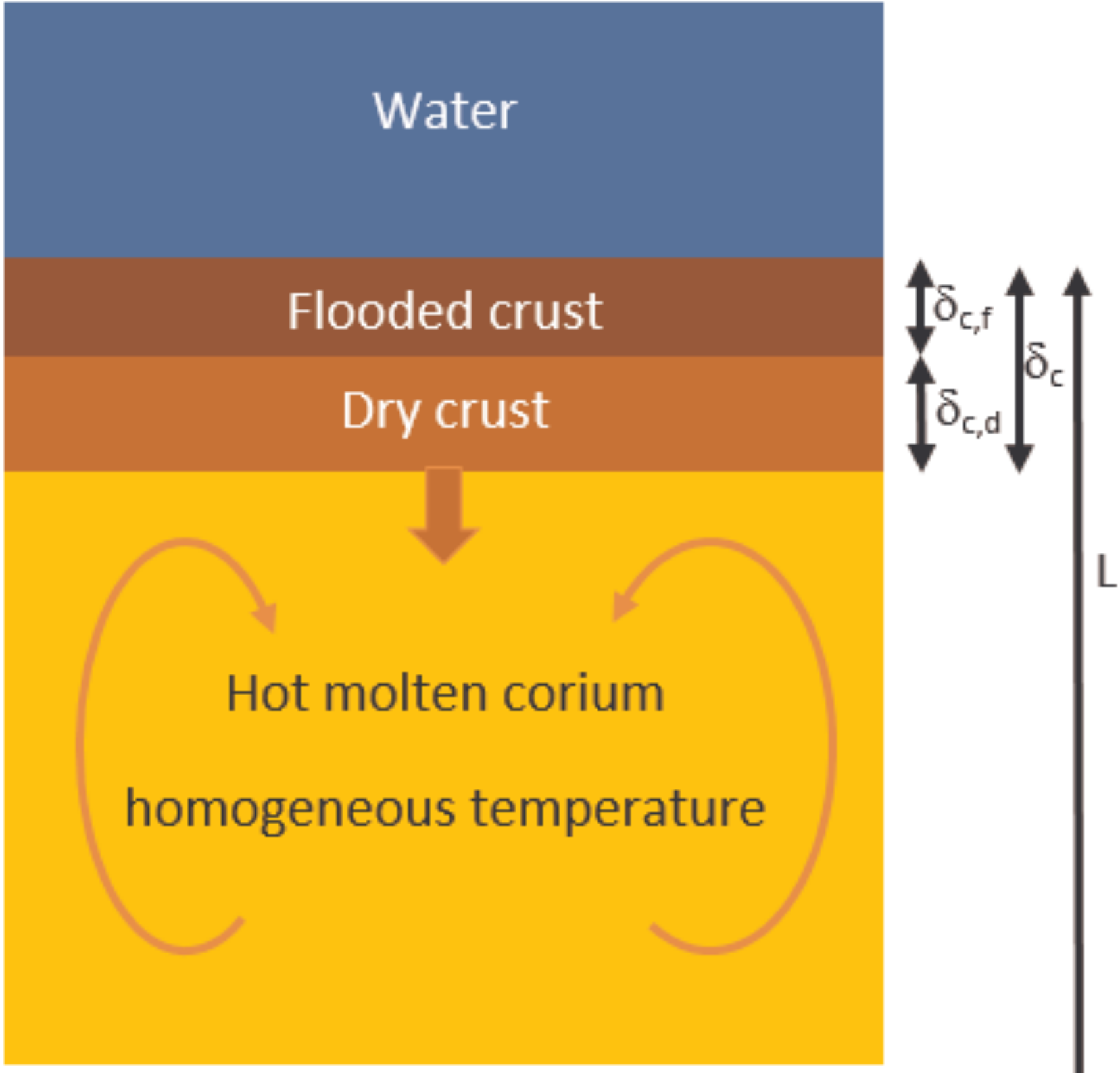
Water
Flooded crust
Dry crust
Hot molten corium
homogeneous temperature
$\delta_{c,f}$
$\delta_{c,d}$
δ_c
L
figure

figure

figure

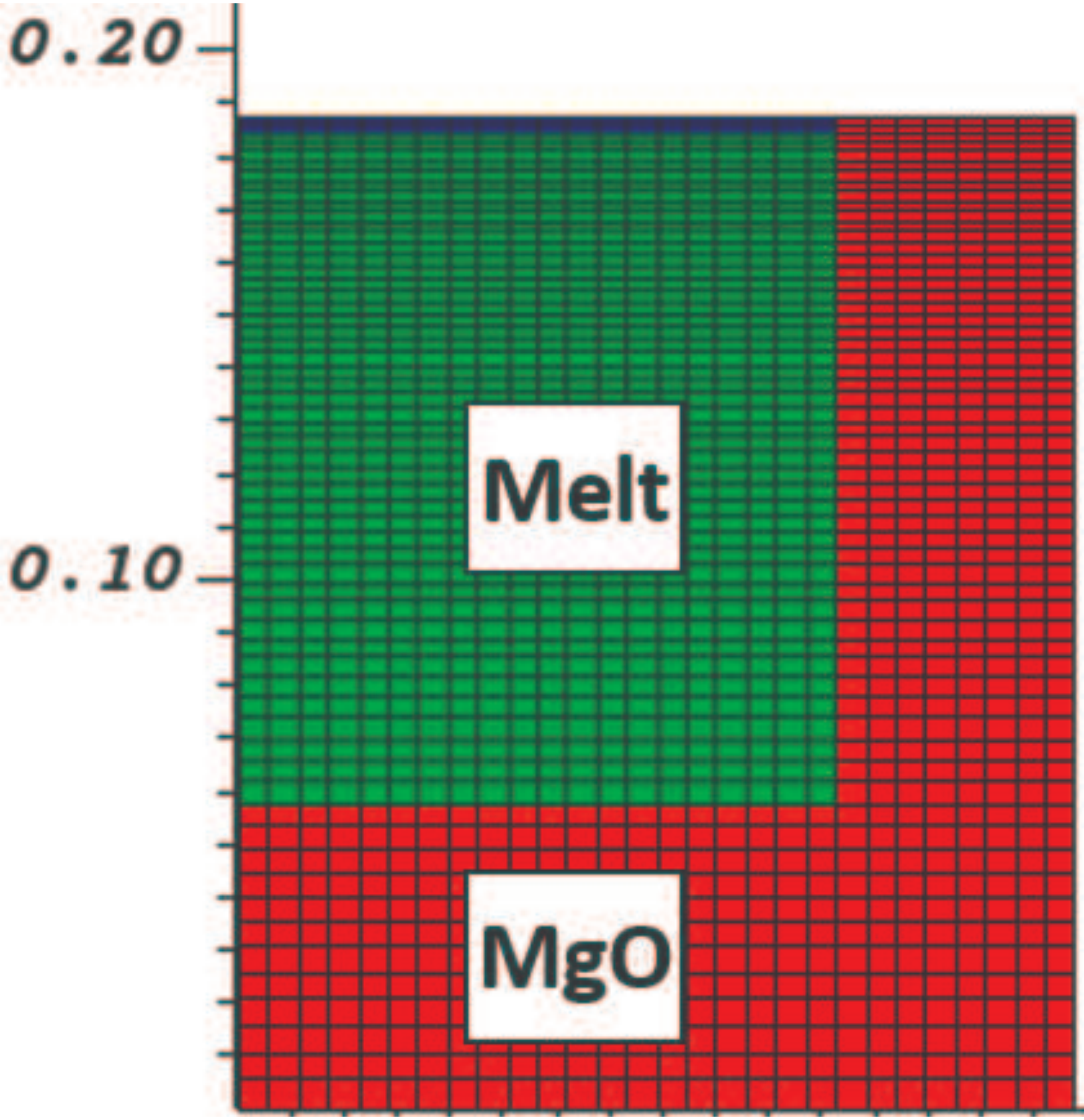

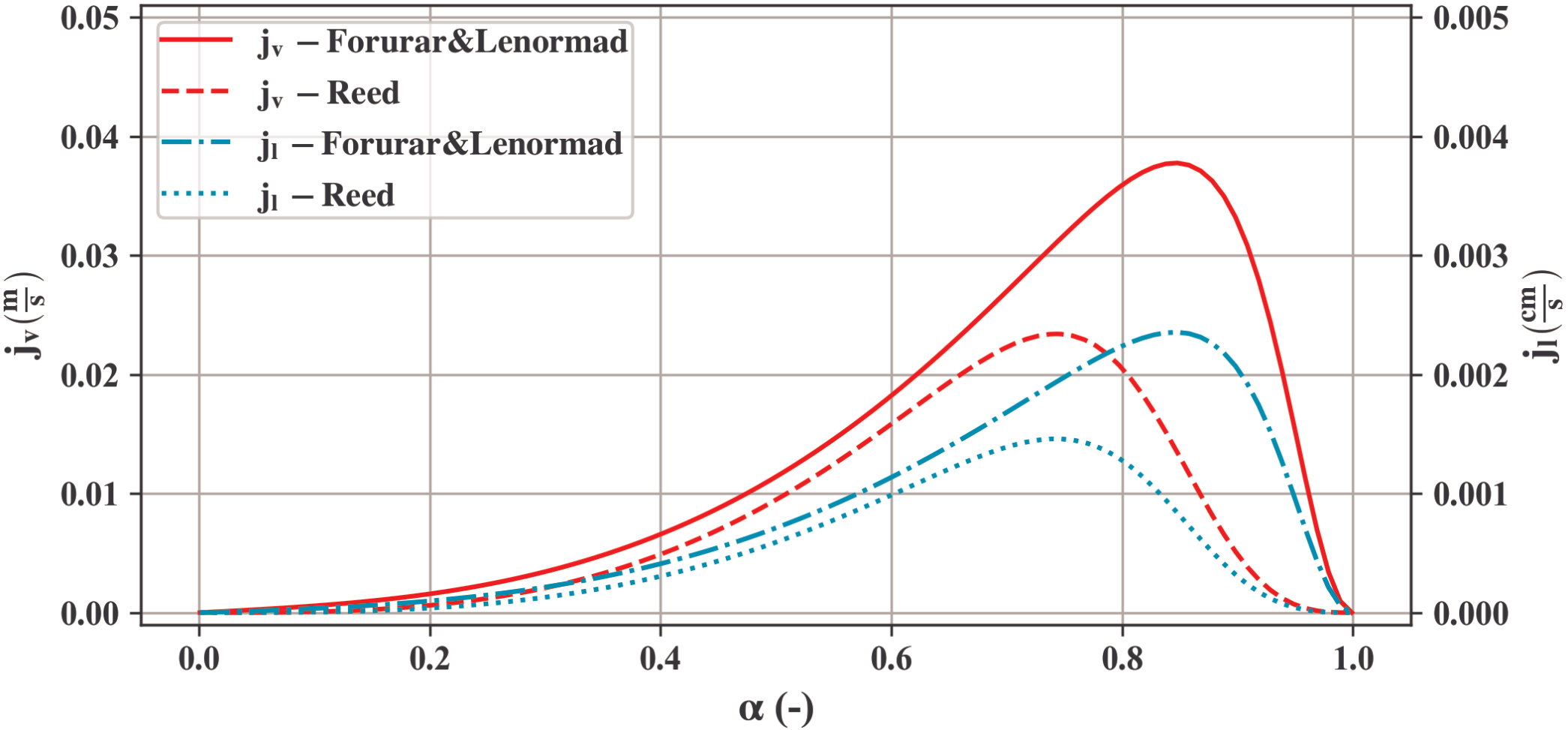
j_v – Forurar&Lenormad
j_v – Reed
j_l – Forurar&Lenormad
j_l – Reed
0.05
0.04
0.03
0.02
0.01
0.00
0.005
0.004
0.003
0.002
0.001
0.000
0.0
0.2
0.4
0.6
0.8
1.0
$j_v\left(\frac{m}{s}\right)$
$j_l\left(\frac{cm}{s}\right)$
α (-)

figure

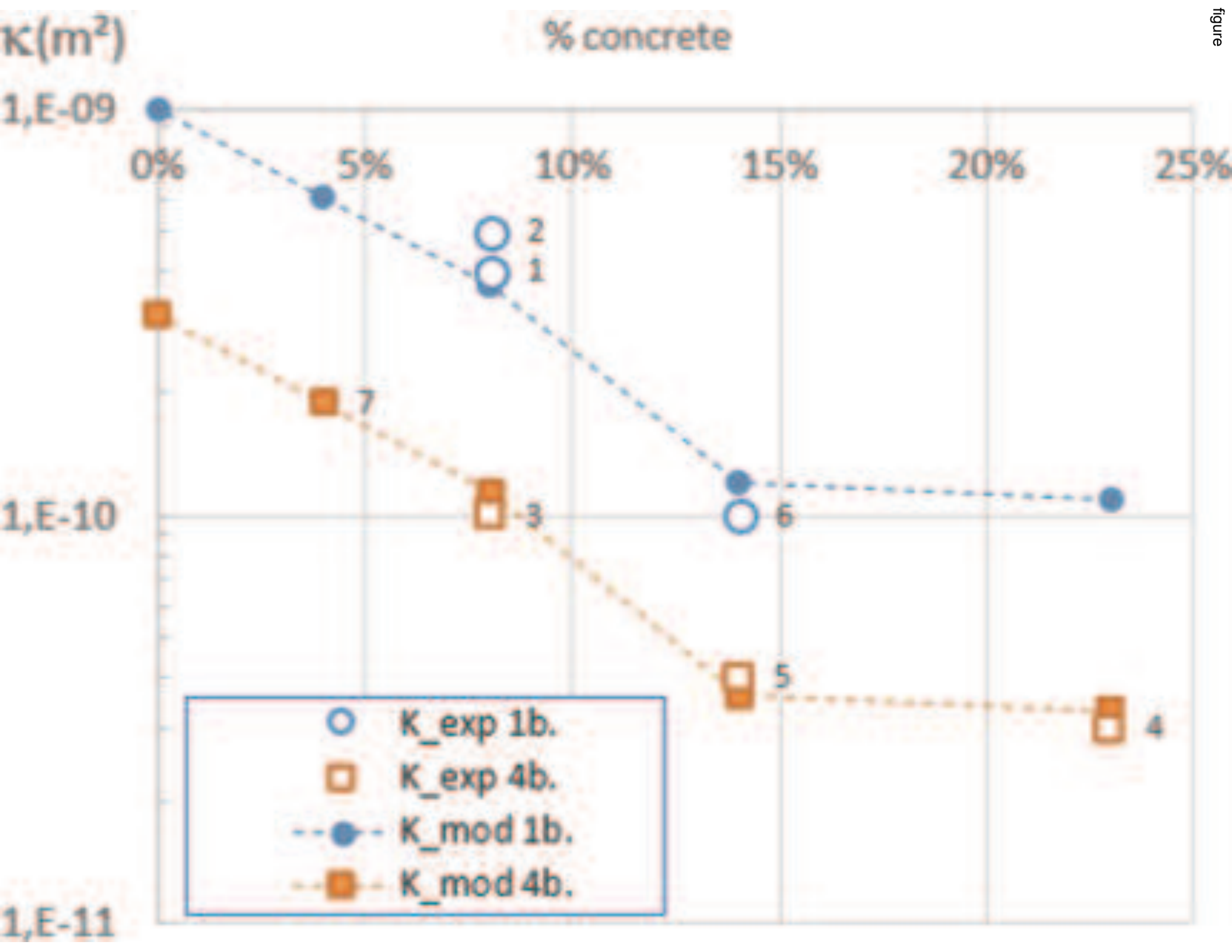
K(m²)
% concrete
1,E-09
1,E-10
1,E-11
0%
5%
10%
15%
20%
25%
1
2
3
4
5
6
7
K_exp 1b.
K_exp 4b.
K_mod 1b.
K_mod 4b.

figure

figure

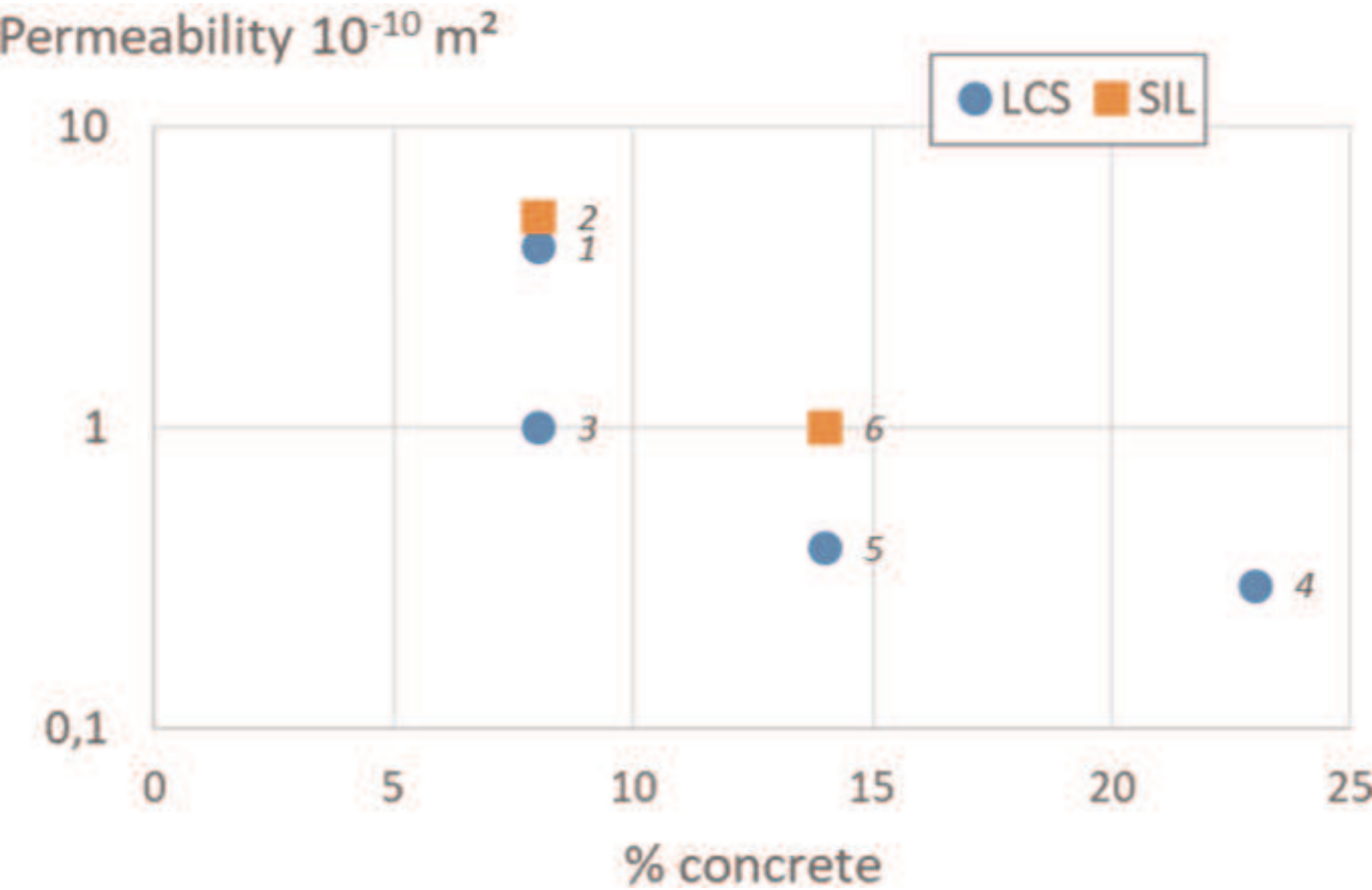
Permeability 10-10 m²
LCS
SIL
10
1
0,1
0
5
10
15
20
25
% concrete
1
2
3
4
5
6

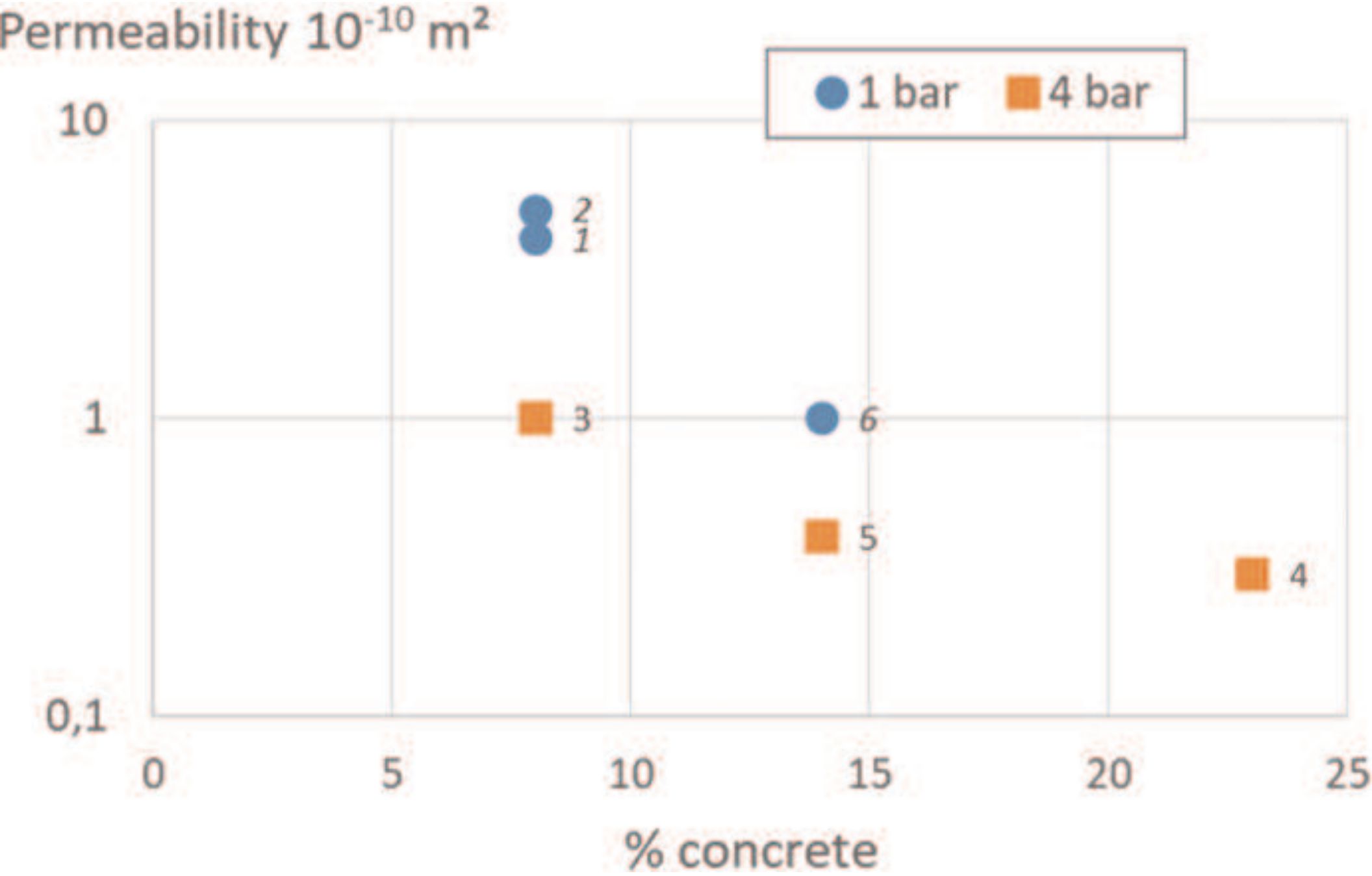
Permeability 10-10 m²
1 bar
4 bar
10
1
0,1
0
5
10
15
20
25
% concrete
2
1
3
6
5
4

figure

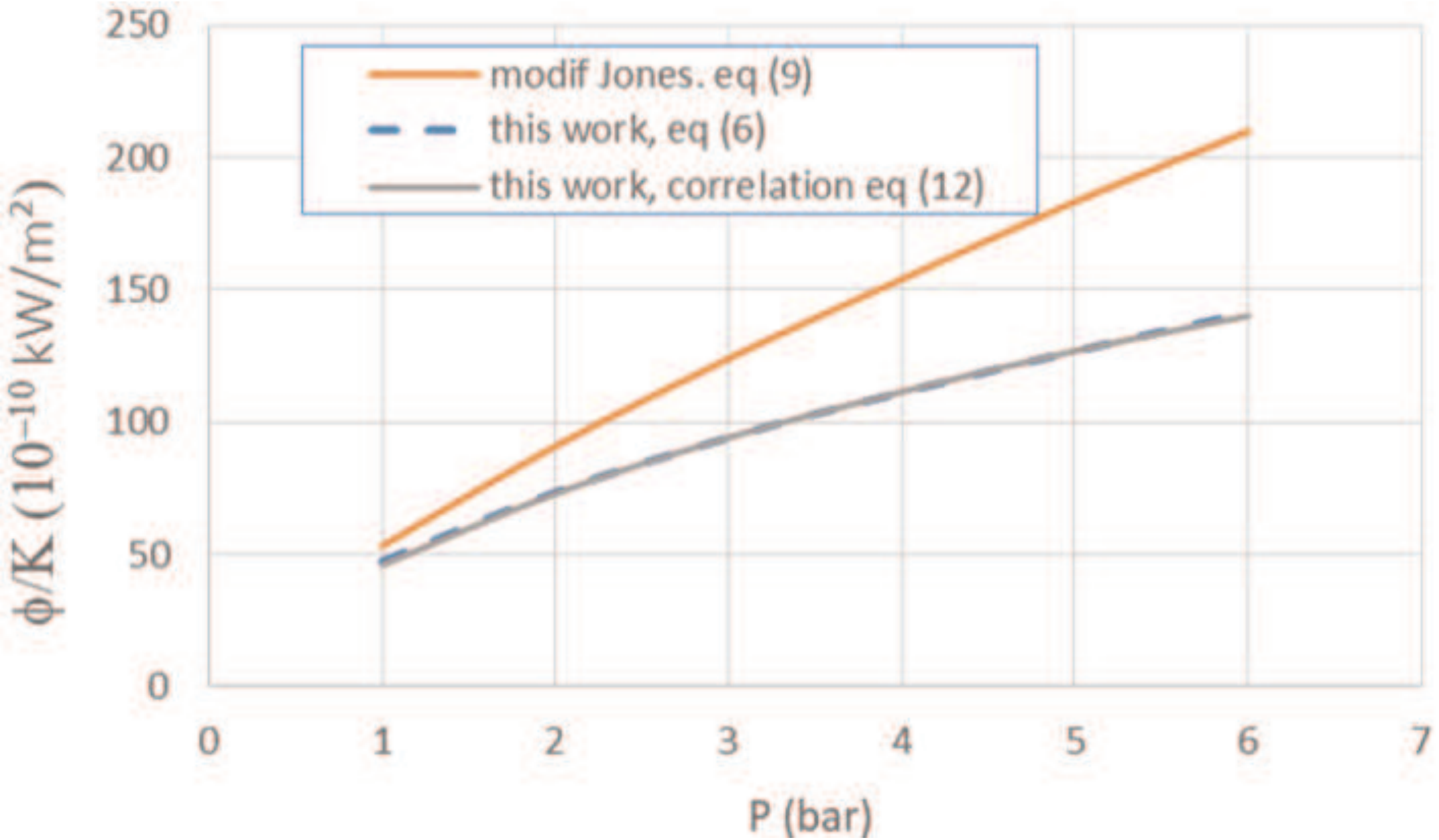
modif Jones. eq (9)
this work, eq (6)
this work, correlation eq (12)
250
200
150
100
50
0
ϕ/K (10⁻¹⁰ kW/m²)
0
1
2
3
4
5
6
7
P (bar)

figure

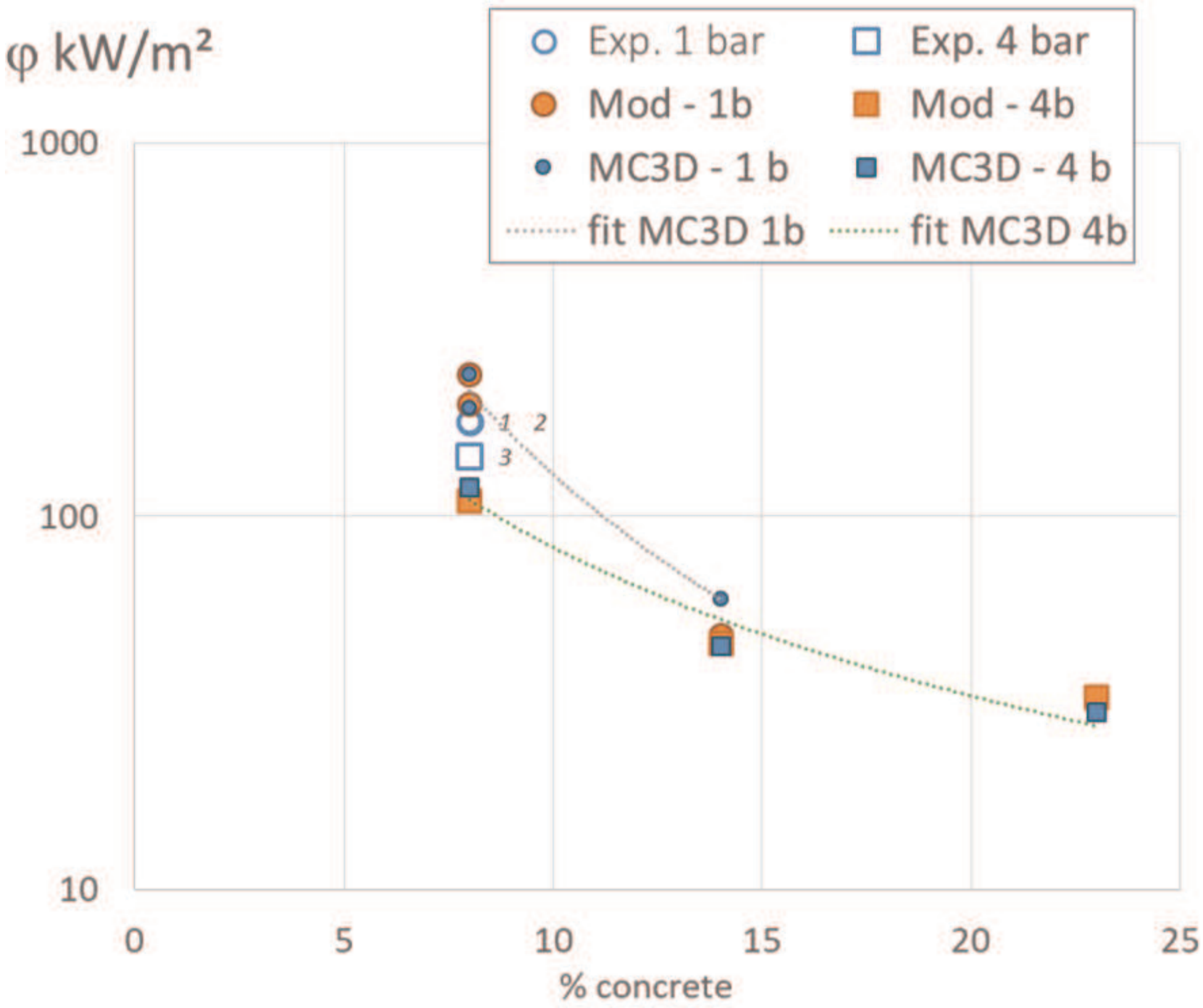
φ kW/m²
Exp. 1 bar
Exp. 4 bar
Mod - 1b
Mod - 4b
MC3D - 1 b
MC3D - 4 b
fit MC3D 1b
fit MC3D 4b
1000
100
10
1
2
3
0
5
10
15
20
25
% concrete
figure

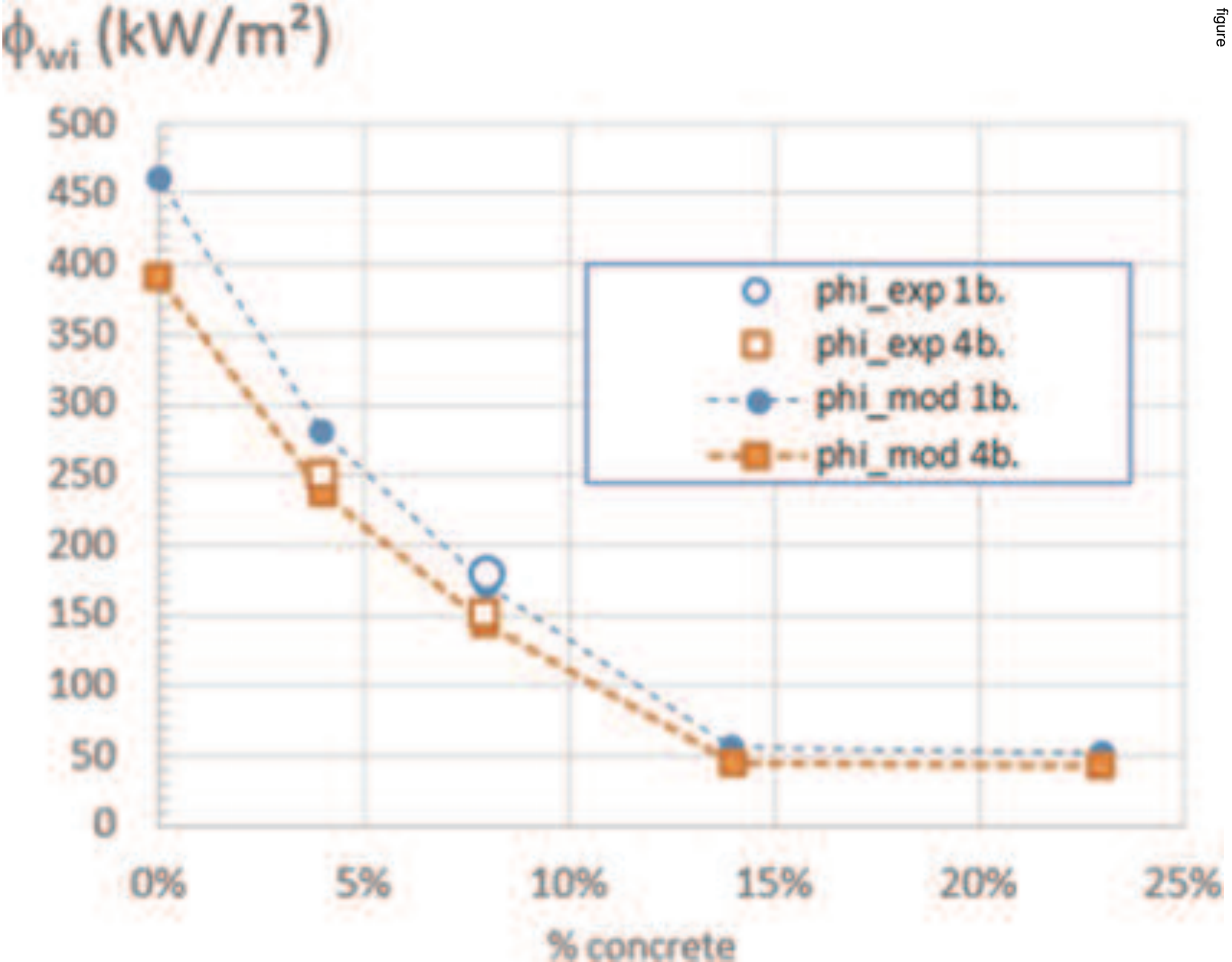
ϕ_{wi} (kW/m²)
500
450
400
350
300
250
200
150
100
50
0
0%
5%
10%
15%
20%
25%
% concrete
phi_exp 1b.
phi_exp 4b.
phi_mod 1b.
phi_mod 4b.

figure

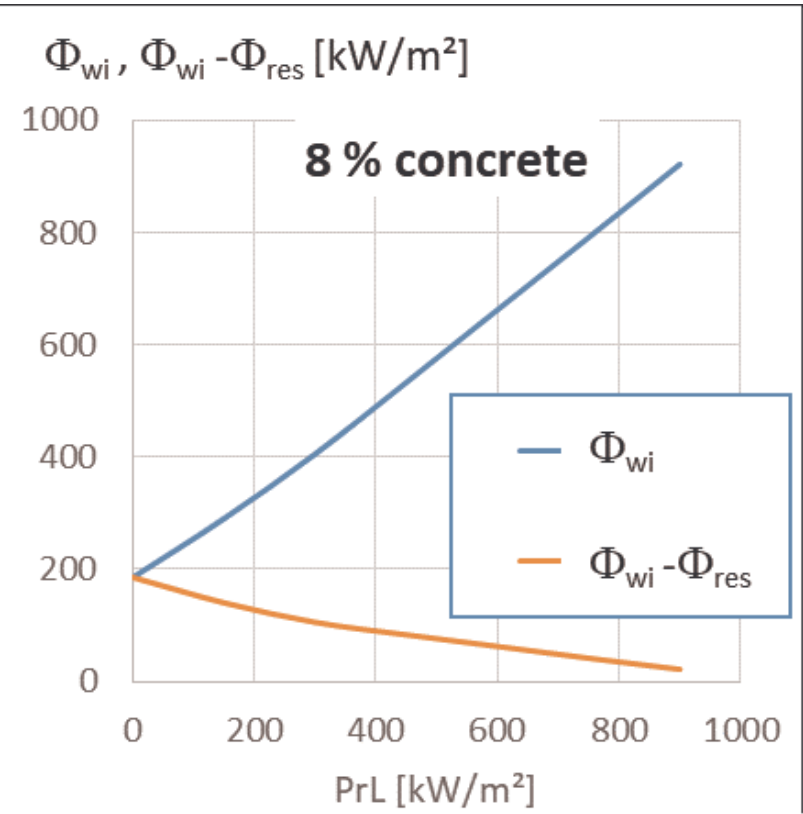
Φwi , Φwi -Φres [kW/m²]
8 % concrete
1000
800
600
400
200
0
0
200
400
600
800
1000
PrL [kW/m²]
Φwi
Φwi -Φres

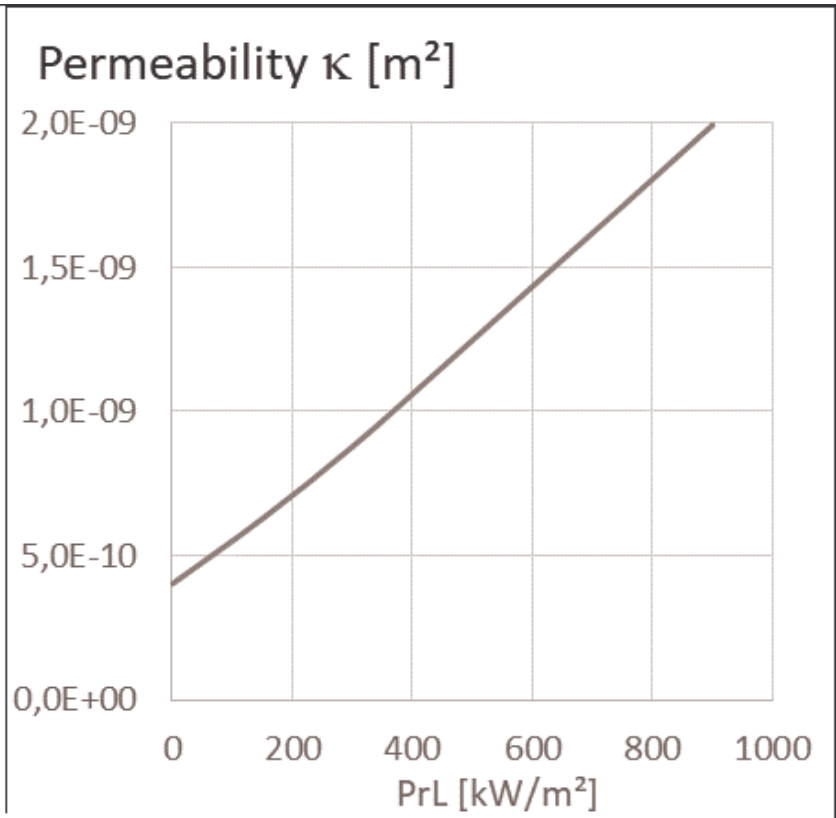
Permeability κ [m²]
2,0E-09
1,5E-09
1,0E-09
5,0E-10
0,0E+00
0
200
400
600
800
1000
PrL [kW/m²]

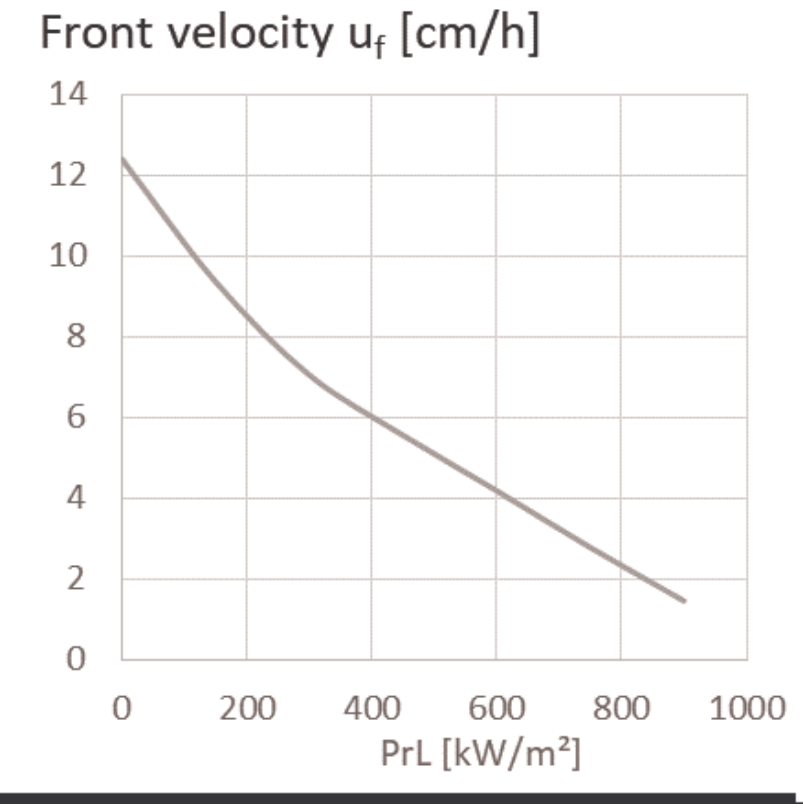
Front velocity uf [cm/h]
14
12
10
8
6
4
2
0
0
200
400
600
800
1000
PrL [kW/m²]

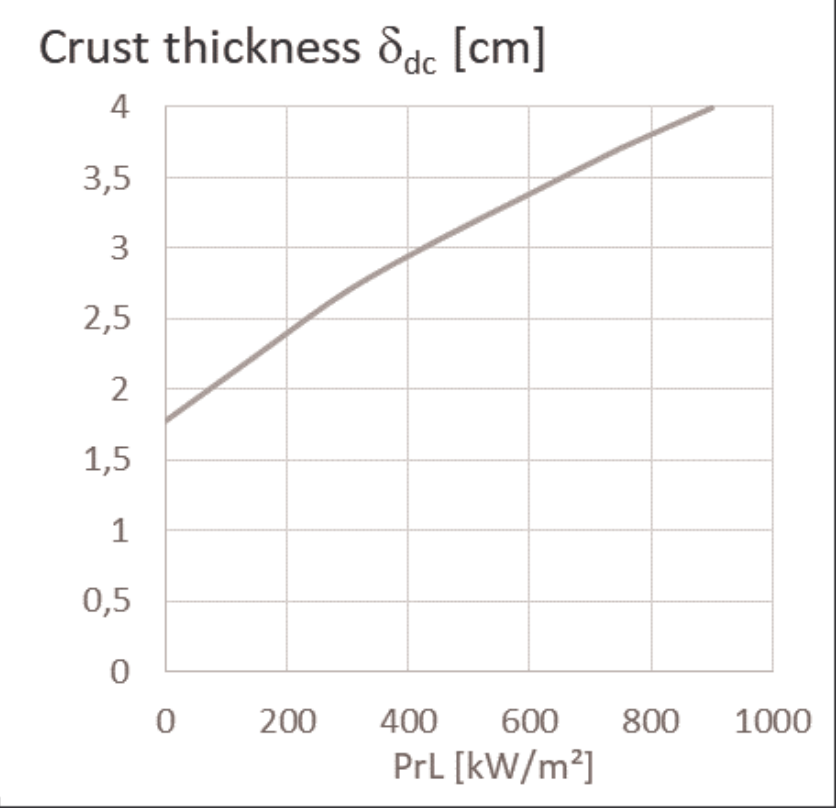
Crust thickness δdc [cm]
4
3,5
3
2,5
2
1,5
1
0,5
0
0
200
400
600
800
1000
PrL [kW/m²]